UniMi/UniTs/ESA/CNR-
IFP/JBO/IASF-
INAF/UCSB/OAT/SAN
LFI Project System Team

Planck LFI

TITLE: Data Analysis and scientific performances of the LFI FM Instrument

DOC. TYPE: Analysis Document

PROJECT REF.: PL-LFI-PST-AN-006 PAGE: 1 of 108

ISSUE/REV.: 2.0 draft 1 DATE: June 3, 2008

Prepared by	**Aniello Mennella** **Marco Bersanelli** **Benedetta Cappellini** **Angel Colin** **Francesco Cuttaia** **Ocleto D'Arcangelo** **Samuele Galeotta** **Anna Gregorio** **Rodrigo Leonardi** **Stuart Lowe** **Michele Maris** **Luis Mendes** **Peter Meinhold** **Maura Sandri** **Luca Stringhetti** **Luca Terenzi** **Maurizio Tomasi** **Luca Valenziano** **Fabrizio Villa** **Andrea Zonca**	**Date:** June 3, 2008 **Signature:** 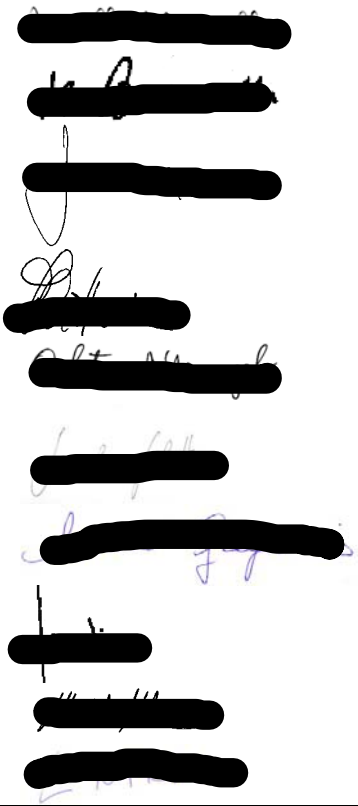

		
Agreed by	**M. BERSANELLI** **LFI Instrument Scientist** **C. BUTLER** **LFI Program Manager**	**Date:** June 3, 2008 **Signature:** 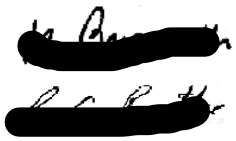
Approved by	**N. MANDOLESI** **LFI Principal Investigator**	**Date:** June 3, 2008 **Signature:** 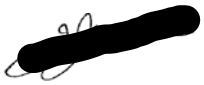

CHANGE RECORD

Issue	Date	Sheet	Description of change	Release
0.1	15th Jun, 2006	All	First structure of document	0.1
0.1	11th Oct, 2006	All	First draft of document	0.1
1.0	30th Oct, 2006	All	First issue of document	1.0
1.1	15th Nov, 2006	All	First update after release 1.0, in correspondence to Planck SVR (16-17 Nov 2006). Major changes to be noticed are: (i) The σ/q column in the REBA section; (ii) the calibrated white noise level has been temporarily removed (will be reintroduced in further versions after thorough understanding of photometric calibration; (iii) the spike section has been reduced (details relegated to annexes); (iv) the THB section has been reduced (details relegated to annexed)	1.1
2.	1st Jun, 2008	All	Release 2.0 with answers to SVR recommendations (still in draft)	draft 1

DISTRIBUTION LIST

Recipient	Company/Institute	E-mail address	Sent
E. Alippi	Alenia Spazio S.p.A.	ezio.alippi@thalesaleniaspace.com	Yes
M. Balasini	Alenia Spazio S.p.A.	maurizio.balasini@thalesaleniaspace.com	Yes
P. Battaglia	Alenia Spazio S.p.A.	paola.battaglia@thalesaleniaspace.com	Yes
E. Artal	Univ. of Cantabria - Santander	artal@dicom.unican.es	Yes
C. Baccigalupi	SISSA - Trieste	bacci@sissa.it	Yes
A. Balbi	Univ. di Roma Tor Vergata	amedeo.balbi@roma2.infn.it	Yes
M. Bersanelli	Univ. degli studi di Milano	marco.bersanelli@fisica.unimi.it	Yes
C. Burigana	INAF-IASF sez di Bologna	burigana@iasfbo.inaf.it	Yes
C. Butler	IASF-CNR Sez di Bologna	butler@iasfbo.inaf.it	Yes
G. Cafagna	Alenia Spazio S.p.A.	gaetano.cafagna@thalesaleniaspace.com	Yes
B. Cappellini	Univ. degli studi di Milanl	benedetta.cappellini@mi.infn.it	Yes
B. Collaudin	ASPI - Cannes	bernard.collaudin@thalesaleniaspace.com	Yes
F. Cuttaia	INAF-IASF sez di Bologna	cuttaia@iasfbo.inaf.it	Yes
O. D'Arcangelo	IFP - CNR	ocleto@ifp.cr.it	Yes
R. Davis	JBO - UK	rjd@jb.man.ac.uk	Yes
G. de Gasperis	Univ. di Roma Tor Vergata	Giancarlo.Degasperis@roma2.infn.it	Yes
L. Figini	IFP - CNR	figini@ifp.cr.it	Yes
M. Frailis	INAF-OAT - Trieste	frailis@oats.inaf.it	Yes
C. Franceschet	Alenia Spazio S.p.A.	cristian.franceschet@thalesaleniaspace.com	Yes
E. Franceschi	INAF-IASF sez di Bologna	franceschi@iasfbo.inaf.it	Yes
T. Gaier	JPL - Pasadena	gaier@merlin.jpl.nasa.gov	Yes
S. Galeotta	INAF-IASF sez di Milano	galeotta@oats.inaf.it	Yes
A. Gregorio	Univ. di Trieste	anna.gregorio@ts.infn.it	Yes
G. Guyot	IAS - Orsay	guyot@ias.u-psud.fr	Yes
R. Hoyland	IAC - Tenerife	rjh@ll.iac.es	Yes
N. Hughes	Ylinen	nicholas.hughes@elektrobit.com	Yes
D. Kettle	JBO - UK	dkettle@jb.man.ac.uk	Yes
J.M. Lamarre	IAS - Orsay	lamarre@ias.u-psud.fr	Yes
C. Lawrence	JPL - Pasadena	crl@jplsp.ipl.nasa.gov	Yes
R. Leonardi	UCSB – USA	rodrigo@deepspace.ucsb.edu	Yes
P. Leutenegger	Alenia Spazio S.p.A.	paolo.leutenegger@thalesaleniaspace.com	Yes
S. Lowe	JBO - UK	slowe@jb.man.ac.uk	Yes
D. Maino	Univ. degli studi di Milano	davide.maino@fisica.unimi.it	Yes
M. Malaspina	INAF-IASF sez di Bologna	malaspina@iasfbo.inaf.it	Yes
N. Mandolesi	INAF-IASF Sez. di Bologna	reno@iasfbo.inaf.it	Yes
M. Maris	INAF-OAT - Trieste	maris@oats.inaf.it	Yes
E. Martinez-Gonzalez	Univ. of Cantabria - Santander	martinez@ifca.unican.es	Yes
P. Meinhold	UCSB – USA	peterm@cfi.ucsb.edu	Yes
L. Mendes	ESA	lmendes@rssd.esa.int	Yes
A. Mennella	Univ. degli studi di Milano	aniello.mennella@fisica.unimi.it	Yes
M. Miccolis	Alenia Spazio S.p.A.	maurizio.miccolis@thalesaleniaspace.com	Yes
G. Morgante	INAF-IASF Sez. di Bologna	morgante@iasfbo.inaf.it	Yes
P. Natoli	Univ. di Roma Tor Vergata	paolo.natoli@roma2.infn.it	Yes
L. Pagan	Alenia Spazio S.p.A.	luca.pagan@thalesaleniaspace.com	Yes

F. Pasian	INAF-OAT - Trieste	pasian@oats.inaf.it	Yes
T. Passvogel	ESA - PT	tpassvog@estec.esa.nl	Yes
L. Perez	ESA	Leticia.Perez.Cuevas@esa.int	Yes
F. Perrotta	INAF-OAT - Trieste	perrotta@oats.inaf.it	Yes
J.L. Puget	IAS - Orsay	puget@ias.u-psud.fr	Yes
N. Roddis	JBO - UK	nr@jb.man.ac.uk	Yes
M. Sandri	INAF-IASF sez di Bologna	sandri@iasfbo.inaf.it	Yes
M. Seiffert	JPL - Pasadena	michael.d.seiffert@jpl.nasa.gov	Yes
R. Silvestri	Alenia Spazio S.p.A.	roberto.silvestri@thalesaleniaspace.com	Yes
A. Simonetto	IFP - CNR	simonetto@ifp.cr.it	Yes
C. Sozzi	IFP - CNR	sozzi@ifp.cr.it	Yes
J. Tauber	ESA	jtauber@astro.estec.esa.nl	Yes
L. Terenzi	INAF-IASF sez di Bologna	terenzi@iasfbo.inaf.it	Yes
M. Tomasi	INAF-IASF sez di Milano	tomasi@lambrate.inaf.it	Yes
J. Tuovinen	Millilab	jussi.tuovinen@vtt.fi	Yes
L. Valenziano	INAF-IASF sez di Bologna	valenziano@iasfbo.inaf.it	Yes
J. Varis	Millilab	jussi.varis@vtt.fi	Yes
F. Villa	INAF-IASF sez di Bologna	villa@iasfbo.inaf.it	Yes
A. Wilkinson	JBO - UK	aw@jb.man.ac.uk	Yes
F. Winder	JBO - UK	fwinder@jb.man.ac.uk	Yes
A. Zacchei	INAF-OAT - Trieste	zacchei@oats.inaf.it	Yes
A. Zonca	Univ. degli Studi di Milano	andrea.zonca@mi.infn.it	Yes
LFI System PCC	INAF-IASF sez di Bologna	lfispcc@iasfbo.inaf.it	Yes

Contents

Abstract

In this report we discuss the results of the scientific analysis of the radiometric data acquired during the calibration and testing of the LFI FM instrument.

Reference Documents

[RD1] T. Bernardino. Description of the equations involved in the Radiometer Susceptibility to Environmental Fluctuations Module of RaNA. Technical Report PL-LFI-SAN-TN-129 1.0, Universitad de Cantabria, March 2005.

[RD2] F. Cuttaia, A. Gregorio, and M. Tomasi. Quick look data analysis of LFI IST1 test. Technical Report PL-LFI-PST-RP-XXX, IASF-INAF, 2008.

[RD3] A Mennella. Estimating white noise sensitivity in flight conditions from raw measured ground data. Technical Report PL-LFI-PST-TN-083 1.0, UniMi, March 2008.

[AD5] A. Mennella, M. Bersanelli, B. Cappellini, A. Colin, F. Cuttaia, O. D'Arcangelo, S. Galeotta, A. Gregorio, R. Leonardi, S. Lowe, M. Maris, L. Mendes, P. Meinhold, M. Salmon, M. Sandri, L. Stringhetti, L. Terenzi, M. Tomasi, L. Valenziano, and F. Villa. Data analysis and scientific performances of the LFI FM instrument. Technical Report PL-LFI-PST-AN-006 1.1, UniMi, IASF-INAF, UCSB, SAN, OAT, UniTs, CNR-IFP, ESA, JBO, November 2006.

[RD5] A. Mennella and R. Leonardi. LFI calibration and testing data analysis methods. Technical Report PL-LFI-PST-TN-068, UniMi, UCSB, December 2005.

[RD6] A. Mennella, M. Sandri, F. Perrotta, T. Poutanen, and Krachmalnicoff N. Analysis and characterisation of spurious frequency spikes in the LFI radiometric data acquired during the LFI FM test campaign. Technical Report PL-LFI-PST-AN-077, UniMi, INAF-OATS, Uni Helsinki, November 2007.

[RD7] T. Poutanen. Noise spectrum fits to the LFI FM data. Univ. Helsinki, November 2007.

[RD8] L. Stringhetti and F. Cuttaia. Current drop noise in RCA 23 FEM. Technical Report PL-LFI-PST-TN-079, IASF-INAF, 2007.

[RD9] L. Stringhetti, F. Cuttaia, O. D'Arcangelo, E. Franceschi, A. Mennella, M. Miccolis, and M. Sandri. Quick look data analysis of LFI WFT. Technical Report PL-LFI-PST-RP-023, IASF-INAF, November 2007.

[RD10] L. Stringhetti, F. Cuttaia, O. D'Arcangelo, and M. Sandri. Quick look data analysis of LFI SFT. Technical Report PL-LFI-PST-RP-024, IASF-INAF, November 2007.

[RD11] L. Stringhetti, F. Cuttaia, O. D'Arcangelo, and M. Tomasi. Quick look data analysis of LFI EMC. Technical Report PL-LFI-PST-RP-030, IASF-INAF, February 2008.

[RD12] L. Stringhetti, F. Cuttaia, and A. Gregorio. Quick look data analysis of LFI performed during SIT. Technical Report PL-LFI-PST-RP-028, IASF-INAF, 2008.

[RD13] L. Stringhetti, F. Cuttaia, A. Mennella, and M. Sandri. Proposal for LFI test dedicated to characterize New Spikes in the FFT spectrum of Scientific Data. Technical Report PL-LFI-PST-TN-080, IASF-INAF, November 2007.

[RD14] L. Terenzi. Measurements of temperature distribution in a FM sky-load representative sample of ECCOSORB. November 2006.

[RD15] L. Terenzi, F. Cuttaia, and S Grassi. A critical data analysis of the RCA27 Flight Spare Tuning. Technical Report PL-LFI-PST-TN-084 0.1, IASF-BO/UniMi, April 2008.

[RD16] L. Terenzi, A. Mennella, G. Morgante, M. Tomasi, and L. Valenziano. Preliminary evaluation of the impact of temperature fluctuations in the HFI 4K-stage on LFI. Technical Report PL-LFI-PST-TN-048 2.0, IASF-BO, UniMi, June 2006.

[RD17] M. Tomasi. *Data analysis of the Planck-LFI QM/FM tests*. PhD thesis, Università degli Studi di Milano, Milano, Italy, 2007.

[RD18] M. Tomasi. Analysis of the DAE offset problem. Technical Report PL-LFI-PST-TN-085, UniMi, May 2008.

[RD19] F. Villa, L. Pagan, and M. Sandri. LFI alignment evaluation and recovery proposal. Technical Report PL-LFI-PST-TN-054 2.1, IASF-BO, TAS-I, February 2005.

Applicable Documents

[AD1] M. Bersanelli, F. Cuttaia, A. Mennella, and F. Villa. Effects of BEM compression. Technical Report PL-LFI-PST-TN-XXX, UniMi, IASF-BO, 2006.

[AD2] F. Cuttaia, E. Franceschi, A. Mennella, M. Sandri, L. Stringhetti, and M. Tomasi. Quick Look Data Analysis Of LFI Spike Tests during EMC tests. Technical Report PL-LFI-PST-RP-031 1.0, IASF-BO/UniMi, April 2008.

[AD3] C. Franceschet. Planck LFI FM test report. Technical Report PL-LFI-LAB-RP-073, Alenia Spazio, October 2006.

[AD4] P. Leutenegger. Planck-LFI test plan. Technical Report PL-LFI-LAB-PL-009, AAS, 2006.

[AD5] A. Mennella, M. Bersanelli, B. Cappellini, A. Colin, F. Cuttaia, O. D'Arcangelo, S. Galeotta, A. Gregorio, R. Leonardi, S. Lowe, M. Maris, L. Mendes, P. Meinhold, M. Salmon, M. Sandri, L. Stringhetti, L. Terenzi, M. Tomasi, L. Valenziano, and F. Villa. Data analysis and scientific performances of the LFI FM instrument. Technical Report PL-LFI-PST-AN-006 1.1, UniMi, IASF-INAF, UCSB, SAN, OAT, UniTs, CNR-IFP, ESA, JBO, November 2006.

[AD6] T. Poutanen, R. Leonardi, and P. Meinhold. Knee frequency versus input temperature. Technical Report PL-LFI-PST-TN-086 1.0, May 2008.

[AD7] L. Stringhetti and A. Gregorio. TV Tests: LFI Test Under Cryogenic Vacuum. Technical Report PL-LFI-PST-PR-021-2.2, IASF-BO/OATs, May 2008.

[AD8] M. Stringhetti, A. Gregorio, A. Mennella, G. Morgante, F. Villa, F. Cuttaia, and M. Bersanelli. Testing Plan of the LFI instrument during the Planck Commissioning and CPV phase. Technical Report PL-LFI-PST-PL-013 1.2, UniMi/IASF-BO/OATs, April 2008.

[AD9] J. Tauber and L. Mendes. LFI science verification review. Test completion review report. Technical Report Planck/PSO/2007-001, ESA/PSO, February 2007.

1 Summary

This documents reports the scientific calibration activities performed on the LFI Flight Model and the obtained results. The current issue contains answers to recommendations of the Science Verification Review held in ESTEC during November 2006 ([AD9]).

Some of the sections have been changed considerably so that a complete rewriting was necessary. These are indicated at the beginning of the section by a warning sentence in italic. Please refer to [AD5] for the old version. In some cases changes were minor so that the corresponding sections have been updated. Finally, some sections remained unchanged.

In the next section we summarise the SVR recommendations with a summary of their status, together with references to documents containing more detail.

2 List of SVR recommendations

Here we summarise the list of recommendations raised at the Science Verification review with a brief list of answers. More details are provided in the annexed documentation.

2.1 Functionality

An effort to understand the causes of the effect caused by the switch on procedure on LFI 28 should be undertaken.

The standard LFI switch on procedure, when applied to RCA 28, produced several unexplained features, like, for example: saturation in RCA 28 scientific output, saturation in other channels where just the BEM was powered (LNAs biased OFF), anomalous increase in drain currents. These features were observed just during cold functional tests and never with LNAs at warm conditions. Despite the problem was not understood, it was practically solved by modifying the switch on procedure just for RCA 28. The new procedure was already used during LFI warm functional tests at satellite level in Cannes, where the anomaly never showed up.

In the present schedule, extra tests are not foreseen in CSL to investigate the RCA 28 behaviour in cryo conditions (where the feature appear). The custom procedure has been included in the CSL procedure everywhere the RCA 28 is required to be switched on.

Extra dedicated tests at satellite level have been not foreseen, especially to avoid triggering the effect with potentially dangerous effects for the whole instrument.

An investigation on the causes of the pop corn noise and the current jumps on LFI 23 should be performed

Description: two different unwanted features affected the RCA 23 scientific output during the RAA test campaign: (i) pop corn noise on RCA 23 R1D1 scientific output and (ii) current drops on RCA 23 (S1 LNA). Although they both affect the scientific output, they have a different nature since the first affects just the BEM output while the second is due to abrupt variations in the front end LNA current.

During the RAA test campaign pop corn noise exhibited both in cryo and warm conditions while current drops just during warm functional tests. Both features have been deeply monitored in Cannes, during WFT, SFT, IST, EMC tests.

Results from pop corn noise analysis are fully documented in: [RD9, RD10, RD11].

Current drops are traced by PRISMA 3877 and detailed in [RD8, RD12, RD2].

Analysis showed that pop corn noise level (peak to peak) and its overall appearance remained the same as during RAA tests and appear always in the RCA 23 R1D1 output. Tests confirm that this feature is characteristic of the BEM output (diode R1D1).

Current drops appeared during tests in Cannes just a few times, as documented in [RD12]. The cause triggering drops is not clear but could be related with the level of bias applied in warm conditions. In any case, since this effect never appeared in cryo conditions, a deeper investigation is required during the cryogenic test campaign in CSL in quiet conditions (no TC sent, no activities performed on the other instruments). A possible slot for this check seems to be during the 24 hours long duration acquisition (see [RD13] for further details).

The effects of the pop corn noise on the map making and its propagation to the scientific output of the LFI should be evaluated

The effect of pop corn noise seems to be independent on the input power entering the BEM, affecting in the same way both SKY and REF signal, since it is caused by a bi-stable oscillation on the BEM diode R1D1. This effect is mostly removed when data are differentiated.

To evaluate the propagation of this effect on sky maps a datastream of at least 24 hours is required in stable conditions (we recall that this effect was not seen during the cold test campaign, but only after warm up, so we do not have a long acquisition in stable and cold conditions containing this effect).

The same test proposed for CSL in [RD13] will provide suitable data for an assessment of this effect on maps and power spectra in case it will show up again.

2.2 Feed-OMTs

Evaluate the effect of the non-compliances in isolation and return loss on science.

Insertion loss has two main effects: attenuate the signal and "generate "thermal noise. Basically one should calculate the eccess of noise and the gain loss with respect to nominal values. Therefore the effect on science is already taken into account during RCA and RAA calibration in the white noise sensitivity results.

The main effect of the return loss is to modify the band of the radiometer. Similarly to the previous case this effect is accounted for in the white noise sensitivity and in the receiver in-band response.

More detailed assessments will come from the results of the "end-to-end phase II" simulations that include realistic noise sensitivities derived from ground test data and receiver in-band response.

Investigate further the reasons for the discrepancies in the cross-polar angular response to gain more confidence in the modelling, if possible using measurements on spare units.

Cross polar discrepancies have two main causes:

1. very difficult measurements for cross polar low levels as in the case of LFI horns
2. real horn geometry different form the design one.

Regarding the first point our baseline is not to perform further measurements on flight spares because of a lack of resources, also considering that feed horn cross polarisation is very low and does not present a problem in any way. Regarding the second point we have run complete feed horn simulations with detailed horn geometries, but a comparison of simulations with measurements has not been done yet.

Determine for each detector the angle of the principal electric plane of polarisation for each detector and its uncertainty

At horn level, the polarization angle is determined by the two OMT arms. For the electromagnetic properties of OMT the field is divided at 90 degrees. The uncertainty may be derived from mechanical uncertainties of OMT. This work is in progress. The major effect however is expected to be the uncertainties of the FPU manufacturing, and the cool down effects. These have been studied in [RD19].

For polarization orientation on the SKY we should include the geometry of the real telecope.

Determine by simulation the main beam shape for each LFI RCA, taking into account the performance of the real telescope.

TBW

2.3 DAE offset

A procedure for in-flight calibration of the DAE offset tables should be prepared before the CSL/PFM2 tests in order to be performed during the tests.

The DAE offset calibration procedure has been prepared, and it is included in [AD7] (par. 5.6.7.2).

An investigation into the origins of the so-called differential effect should be performed and if possible a fix should be produced.

An extensive analysis of the effect has been done, and the results are reported [RD18].

If a fix cannot be produced the consequences of the existence of the offset-level avoidance region should be investigated.

Once the range of dangerous DAE offsets is known, it is straightforward to avoid these values,

since this range is usually quite narrow (a few DEC units) and it can be easily avoided thanks to the number of degrees of freedom (gain, offset) in the DAE calibration.

2.4 Frequency spikes

Investigate the cause of the spike at 8.5 Hz.

FM data analysis as well as subsequent tests conducted at satellite level [AD2] have shown that these frequency spikes are of two very different nature. Purely 1 Hz spikes are directly correlated with the DAE housekeeping sequencer state (disappearing completely when the sequencer is switched off) while spikes at other frequencies (always of the order of few Hz) remain even after the switch off of the HK sequencer. The origin of these spikes is still unkown although it is clear that they originate in the DAE and affect the radiometric data as a common mode effect.

It is unlikely that the exact cause will be understood; the strategy will be to characterise them as thoroughly as possible during TV and CPV tests and remove them from the data in flight if necessary.

Investigate to what level the frequency spikes are still present in differenced data at some level.

A thorough investigation of frequency spikes has been conducted using differential data from the long duration test ST1_0002. This analysis led to the definition of the *spike instrument model*, a collection of tables with the information of frequency spikes in amplitude and phase for each detector. Details of this analysis is reported in [RD6].

Investigate possible tools/filters for removal of the spikes from the output of the radiometers.

Two approaches for spike removal are currently being followed: (i) frequency fourier filtering using the spikes description provided in the instrument model and (ii) time-domain removal using 1-second data binning to highlight the time domain pattern of the 1 Hz disturbance. The first approach has been developed in an IDL code subsequently ported to C++ and integrated into the L2 of the LFI DPC pipeline. The second approach is still at a prototype level and only IDL codes exist at this time. Both approaches have advantages and disadvantages and are in some way complementary; it is likely that both of them will be applied to the data if necessary.

Investigate the effect of any residual spikes on map making and its impact on the scientific outcome of the mission.

A prelimiary investigation limited to the LFI20 and LFI21 70 GHz receivers has been conducted using the *spikes instrument model* and the results are reported in [RD6]. Main results indicate a

very small effect on the temperature anisotropies but a non negligible effect on polarisation. More results will come from the end-to-end phase 2 test of the DPC pipeline.

2.5 Receiver tuning

Prepare tuning procedures to be executed during the CPV phase of the mission for both the phase switch bias currents and the gate voltages in the LNAs. These procedures should take into account that a large parameter space needs to be explored in a limited time interval. The procedures resulting from this recommendation should be available before the CSL test in order for them to be used and eventually fine tuned.

A new receiver tuning procedure has been set up and is part of the TV test plan [AD7] as well as of the CPV test plan [AD8]. This procedure has been defined also on the results of tests performed in TAS-I on the 30 GHz FS receiver aimed at defining a new procedure based on a matrix sampling of the parameter space [RD15].

2.6 Sky load thermal modelling

It is recommended that extensive simulations of the thermal behavior of the sky load be performed to reduce the current uncertainties in the determination of Tsys for the radiometric chains.

As described in Sect. 3.2.2 of this report a wide set of simulations, also correlated with dedicated laboratory test data, were performed in order to have a clear view of the expected behaviour of the sky load in spite of the temperatures measured by sensors during RAA tests.

A representative set of pyramids were considered in the thermal model of the whole RAA experimental setup and a functional relation of the antenna temperature, expected as signal, from the skyload backplate measured temperature was obtained as input to the modules for data analysis. More details are reported in [RD14].

2.7 Non linearity

The impact of temperature measurement errors on the non-linearity issue should be studied, making use also of the sky load thermal behavior simulations discussed in the previous section.

The experimental and modelling study reported in [RD14] allowed to define the best estimate of the sky load temperature to be used in the derivation of the receiver basic properties (noise temperature, gain constant and linarity). Also with this correction the point at highest input temperature showed, in many cases, a higher-than-expected voltage output due to some systematic effect that has not been well understood.

Considering also that three points represent the bare minimum to perform a gain model fit (which depends on three parameters) our approach has been to fit the data constraining the non linearity parameter to stay within $\pm 1\%$ of the RCA value, the rational being that non linearity in the 30-44 GHz receivers arise from the BEM diodes that were at room temperature during both RCA and RAA test campaigns.

Details of the fit and of its results are reported in this document in Sect. 6.

The impact of the non-linearity on the scientific outcome of the LFI should be fully assessed with special attention to the effect that this will have on the calibration of the instrument.

This effect has been studied and it is not expected to impact significantly on the scientific outcome, because the receiver response in practically linear in the dynamic range provided by the sky input. Details of this estimate are provided in [AD1].

2.8 Long term acquisition

The datasets acquired during the RAA test campaign, and particular the long duration test, should be made widely available to the LFI community and an exploitation plan should be drafted.

Datasets have been available on a server at IASF-MI (mephisto.lambrate.inaf.it) together with the LIFE environment. These datasets have been the basis of widespread data analyses exercised

2.9 Receiver bandshape

Detailed analysis and new test results will be soon available in two theses. An MS thesis concerning tests performed on the flight spares and a PhD thesis (available September 2008) summarising all the modelling and analysis work will be available September 2008.

In light of the current situation it is strongly recommended that the acquired knowledge of the bandshapes (resulting from a combination of optical and receiver effects) should be included in a realistic model of the instrument angular and frequency response, in order to allow the production of realistic data streams, that should then be used to study the effect of the non idealities in frequency response and uncertainties in knowledge on photometric calibration, beam characterisation, CMB signal reconstruction, component separation and especially polarization.

Bandpasses are already included into Level S and they will be used by the US team for simulating data for the End to End test phase 2. It is also in preparation, by P Leahy, a module for the pipeline that will improve component separation by an iterative refinement process taking into account bandpasses. In the latter case probably a simplified respresentation of the bandpasses will be used. Beams dependency on frequency is not included yet into the simulations.

It is also strongly recommended that QM receivers and eventually unused spares be used to perform further testing, especially measurements concerning the band margins. Given the uniformity of the performances observed, we expect any results obtained from the spares should still be relevant especially for the purpose of tuning the simulations.

A 30 GHz QM RCA has already been tested at ambient temperature at Alcatel Alenia Space

in Milan during March and April 2008, a Swept Source test was performed with a very large frequency span: 21 to 40 GHz.

These data are still being analysed and will allow a better understanding of 30 GHz response between 21 and 26.5 GHz, the lower limit of the previous tests, and the validation of the model in this frequency range.

A detailed MS thesis summarising all the results will be issued before the end of September 2008.

Evaluate the total out-of-band rejection, possibly using broadband measurements on spare units.

For 70 GHz RCA, it is possible to estimate an out of band rejection based on simulations between 15 and 20 dB with respect to the maximum gain; this is confirmed by measurements just qualitatively, due to the important ripples. A test on a spare component from 50 GHz to 90 GHz instead of 60-80 GHz would better clarify this point.

44 GHz shows an higher rejection of about 30 dB on all channels, based on measurements; simulations show even higher rejection, but they are based on extrapolation, therefore measurements are more conservative in this case.

30 GHz channels measurements show more than 35 dB of rejection and they are confirmed by simulations.

Three sample plots (one for each frequency) of the receiver band response is provided in Fig.

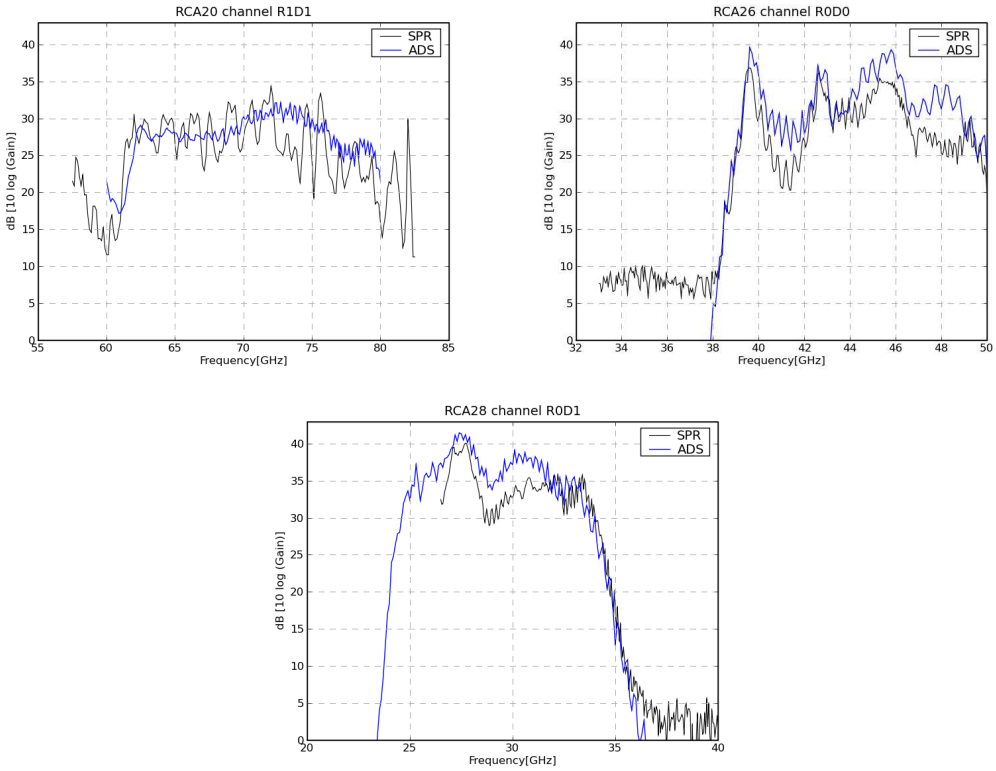

Figure 1: Examples of LFI receiver bandshapes

Establish (in coordination with HFI) means to measure/verify in flight the spectral response of the detectors, using sources having varying spectral functions and angular extents.

It would be possible after data reduction to check the bandpasses of both LFI and HFI by fitting foregrounds of different spectral indexes with the LFI and HFI channels, making a correction for the known bandpass.

If the bandpass is somehow strongly different from the known bandpass, a signature is expected to be seen in the fit as a point distant from the fitting curve, and in particular with an opposite effect on foregrounds with opposite spectral indexes.

This verification should be performed in a collaboration between the component separation Core Team and the IOTs of both HFI and LFI.

2.10 Noise properties

The mismatch in noise temperatures between the RCA and the RAA results should be investigated.

The mismatch has been understood as deriving from the higher FPU temperature in RAA tests compared to RCA tests. We have also provided an estimate of this effect using thermal susceptibility transfer functions measured at RCA level and this mismatch was considerably reduced. Details of this analysis are provided in Sect. 6.

Evaluate the LFI noise data against theoretical models (e.g. the Seyffert model).

The receiver white noise scales very well with the expectation given by the white noise sensitivity formula. Refer to Fig. 38 in Sect. 7 for a demonstration of this. We have also tried to find compare the scaling of the $1/f$ knee frequency with the input offset but with little success, presumably because of the small input offset that was possible to produce in the RAA test setup. Details of this study are provided in [AD6].

2.11 Susceptibility

The reasons why the test XXX_0134 gives rise to completely unexpected results should be investigated.

The test XXX_0134 (instrument warm up after FM test campaign) was not optimized for the thermal susceptibility. In particular during the warmup all the thermal interfaces experienced a rise in temperature and, furthermore, for the most of the useful data range the high sensitivity temperature sensors were off scale.

These two issues jeopardised the possibility to calculate reliable radiometric transfer functions.

A more detailed analysis of the mismatch between the measured and theoretical values for the 30 and 44 GHz receiver susceptibilities should be made. In particular it should be investigated what this mismatch implies for the theoretical model.

The THF_0011 test was a test specifically designed to calculate the radiometric thermal transfer functions. Unfortunately it was run with a bias setup that has been subsequently changed (it was not the optimal one) and the test has not been run again because of schedule reasons.

Results at RCA and RAA levels, therefore, cannont be directly compared apart from the channels that were correctly biased. The comparison for these channels is provided in Sect. 8. The results indicate that there are some channels for which measurements and theory are in good agreement, while for a few others there is still some not understood mismatch.

2.12 Thermal transfer functions

Although the excess damping of the FPU when compared with the mathematical (ESATAN) model is good news, the causes of this effect should be understood and the model updated to reflect it.

The LFI thermal model does not include the effect of contact resistances and this very likely is the cause of the observed excess damping in the experimental data compared to simulations. Taking into account contact resistances in the thermal model would require a massive redesign of the thermal model for a limited improvement in the knowledge of the thermal behavior of the instrument. For this reason we have finally decided to maintain the thermal model as is.

The resolution of the model should be adjusted in order to fully match the observed behaviour of sensors TSL2 and TSL5.

The observed behavior of TSL2 and TSL5 is mainly caused by systematic effects during the experiment. Therefore, changing the model in order to match these effects would produce no real advantage.

Additional simulations and/or measurements should be performed in order to fully explain the observed behaviour of TSR5.

Additional simulations have shown that the problem was in the choice of the node in the thermal model to be compared with the measured behavior of sensor TSR5. After a careful analysis we have found that a proper choice of the thermal node produces results that show a very good match with the other temperature sensors.

Full discussion is provided in [RD17]. The relevant part of this thesis is provided in this data package. Full pdf is available at `http://www.geocities.com/zio_tom78`.

Estimate the effect of realistic fluctuations of the 4K loads induced by the 4K cooler based on the test data presented by HFI.

A preliminary estimate has been provided in [RD16] based on simulated thermal 4K box transfer functions. After one year of coordinated activity between the Thermal Core Teams of both the instruments, an update of the data was recently delivered to be used as input to the end-to-end tests. A higher level of data handling and reducing will be available only during the end-to-end test for a final assessment.

2.13 Further analysis plans

Finalize the calibration report, including all annexes and additional work, before the Satellite-level Instrument Test Completion Review (next stage of the Science Verification Review).

This document issue closes the point.

The WiKi web site, which was set up as a communication tool between all the team involved in the test campaign should be kept alive and used to spread information on the status of the instrument during the forthcoming test campaigns.

The Wiki web site has continued to be a living point of discussion and accumulation of information Since the birth of the Radiometric Core Team area the LFI Wiki has become the natural place to trace the actvities done by the team. Please refer to `http://belzebu.lambrate.inaf.it/twiki/bin/view/LFI/Radio`

3 Cryofacility setup and performances

The cryo-facility is a bell-shaped chamber with 2.5 m base diameter and about 2 m height (see Fig. 2). The LFI RAA is directed downwards to the floor of the chamber (Fig. 2) where a cold Eccosorb load (*sky load*) covers the complete optical field of view.

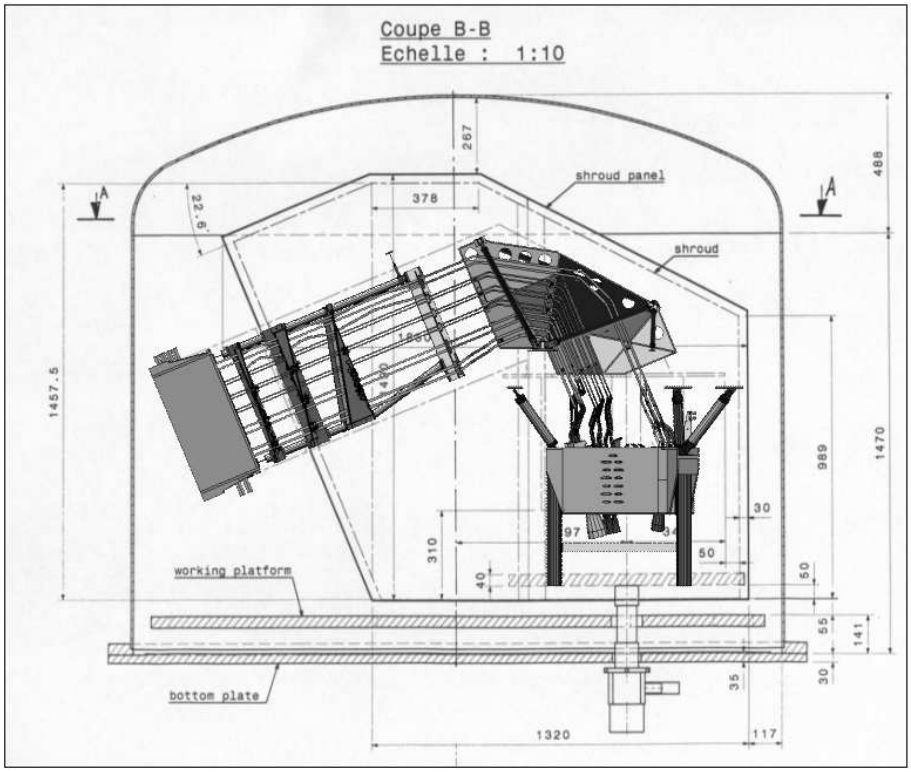

Figure 2: Chamber design and LFI location

The BEU support is connected to a water circuit to keep its temperature close to the nominal one, allowing then to perform a PID control by means of dedicated sensors and heaters. The coldest part is provided with a radiative environment of about 60 K by a shield (*thermal tent*), connected to two 50 K coolers. Also V-grooves 2 and 3 are connected to 50 K coolers.

In Fig. 3 a schematic of the thermal tent is shown together with labels identifying the various panels. Some panels are not shown in the figure (the bottom base, P1, and the panel P2 which is opposite to P9). Furthermore panels P3 and P4 are constituted by two parts, named *a* and *b*. The sides shown in the figure are P3*b* and P4*b*, while P3*a* and P4*a* lie on the opposite side. Interfaces with the coolers are located on P4*a* and P4*b*.

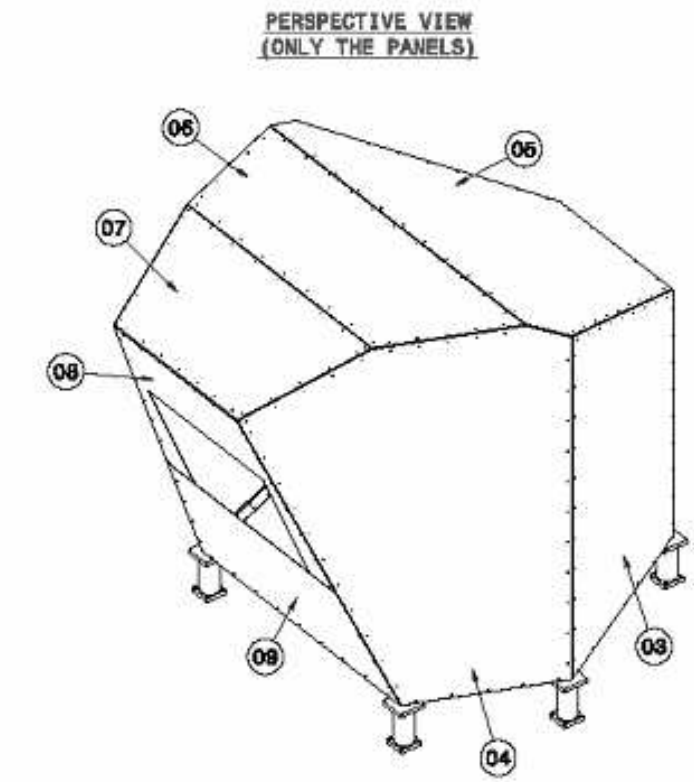

Figure 3: The thermal tent schematic with panels identification numbers.

The V-grooves are couples of copper slabs located at the two opposite sides of the waveguides routing and connected with FM thermal straps to their interfaces with the support structures and waveguides (Fig. 3).

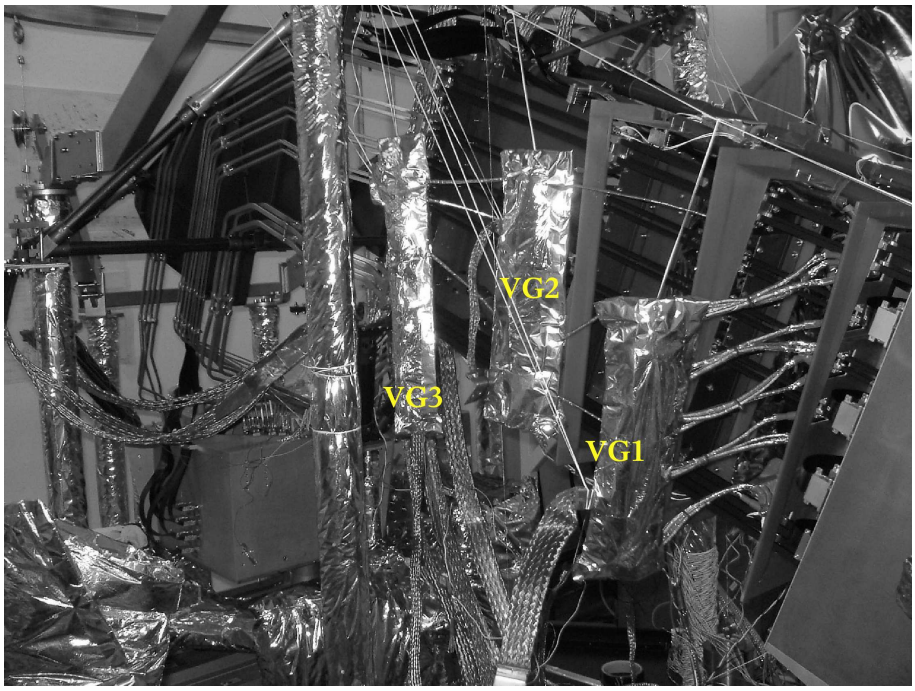

Figure 4: V-groove dummies, constituted by copper slabs covered with MLI and provided with temperature sensors and heaters to allow their temperature control.

The FPU, the HFI dummy, where the 4K reference loads are mounted, and the sky load are all connected to the cold flange of a 20 K cooler. The HFI dummy and the sky load are also provided with a heat switch to enhance the conductivity and speed up thermalization.

In all tests requiring changes in the sky load temperature (e.g. LIS tests) we operated by reducing the heat switch gas pressure down to its complete inactivation.

Here follows a list of the average temperature at various thermal stages acquired during the long duration test (ST1_0001). Many of these values are representative of the temperatures acquired during the whole LFI RAA test campaign.

- Sky load: $\sim$ 18.5 K
- FEU: $\sim$ 25.5 K
- V-groove 1: $\sim$ 184 K
- V-groove 2: $\sim$ 106.2 K
- V-groove 3: $\sim$ 59.5 K
- BEU: $\sim$ 308 K

3.1 Description of acquisition system and chamber sensor

The temperature sensor acquisition system is controlled by a software written in LabView environment that is synchronised with the TQL acquisition system so that the cryo-chamber temperature values are acquired together with the LFI housekeeping.

Two sets of cryo-facility temperature data are acquired:

- one set (labelled *CSL*) is the one already used in the QM test campaign; itemperatures are acquired through two Lakeshore and one Keithley monitors. The software reads 29 sensors with a duty cycle of 10 seconds. After each cycle the software appends to a file all the values read from the sensors. Also the software is designed to control the heaters inside the chamber with a PID philosophy, once the operator has defined the set points to reach, therefore the software is controlling a voltage controlled power supply that gives the right voltage to the heater we need to control.

- the second set (labelled as *Extra*) is acquired by five LakeShore monitors and controllers. This set consists of 27 sensors read with a duty cycle of 30 seconds.

3.2 Analysis of temperature behaviour

An overview of the cryochamber behaviour has been obtained from the first long duration test (ST1_0001) in which the chamber was kept for about 4 days in its steady state at nominal temperatures. A summary of the temperature data (mean temperatures and peak to peak variations) measured during this test is given in Table 1.

3.2.1 Chamber stability

The BEU has been the main source of temperature instability in the LFI chamber which was characterised by a daily modulation in the BEU temperatures that propagated throughout the instrument from the warm to the cryogenic stages (see Figures 5 through 7). Only the parts strictly connected to the 20 K cooler showed a minor correlation with the daily modulation Fig. 9).

This problem was already present during the QM tests (with a p-p variation of ∼5 K) and has been reduced by about one order of magnitude by directly controlling the interface with the BEU (and not the thermostatic bath). Despite this improvement it has not been possible to remove completely this effect.

Figure 5: Temperature fluctuations in different points of the BEU. The BEU control and BEU_1 (right image) sensors are located on the Aluminum support on the two opposite sides of the BEU, while the BEU_2 sensor is located on the top of the DAE Box. Moving far from the control the temperature instability grows.

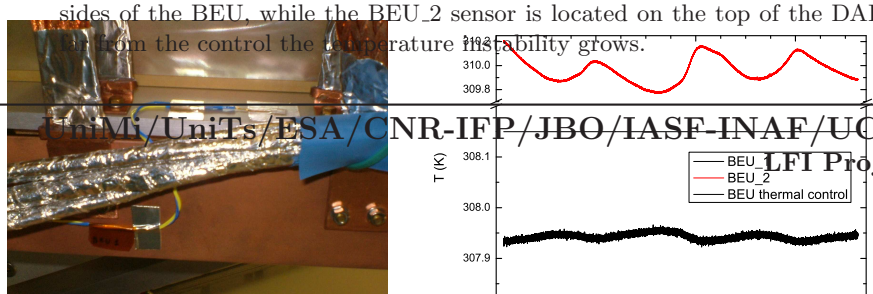

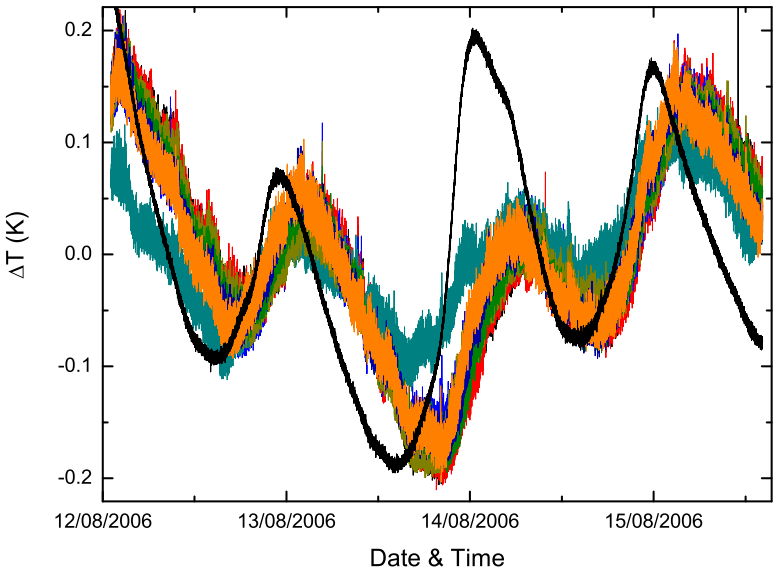

Figure 6: The temperature monitored by the BEU_2 sensor (black curve) is compared to main thermal tent temperatures. Average temperatures have been subtracted from all curves to improve comparison. The BEU fluctuations is in advance of phase with respect ot thermal tents. A deeper investigation will be performed to estabilish if the BEU is driving the instability or the larger thermal inertia of the shroud is delaying it.

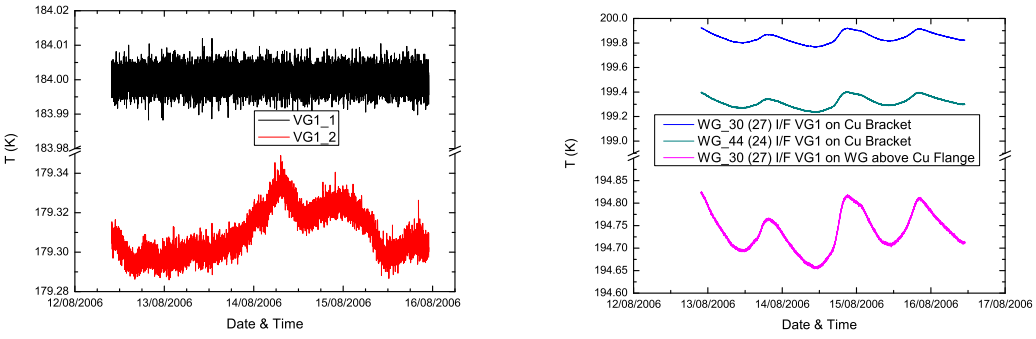

Figure 7: Temperature fluctuation at the opposite sides of the waveguide bundle at the level of first V-groove (temperature sensros VG1_1 and VG1_2 are located on the two opposite side of the WGs routing). The much greater stability measured by VG_1 is an effect of the active temperature control which is driven by VG1_1 sensor.

In the next two figures we show the correlation coefficient between the temperature variations at the various stages with the V-groove temperatures (Fig. 8) and with the FPU temperature (Fig. 9). This correlation analysis shows that many thermal stages are thermally correlated with the VG1 temperature. Little correlation is shown at the level of the reference load sensors, while the sky load temperature (see ECCOSORB side and Centre Pyramid) is moderately correlated with the VG1 temperature. Much less correlation is shown with FPU temperature (see Fig. 9).

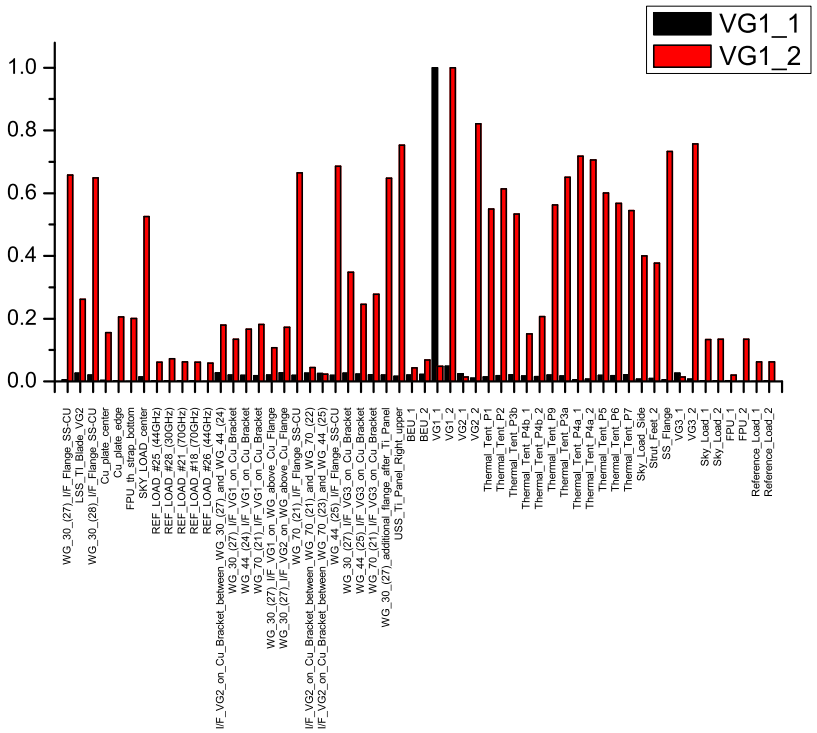

Figure 8: Correlation between VG1_1, VG1_2 sensors with other temperatures in the chamber on a the four days data set. The stage which is directly controlled (VG1_1 sensor) is independent from the overall environment, while VG1_2 is not.

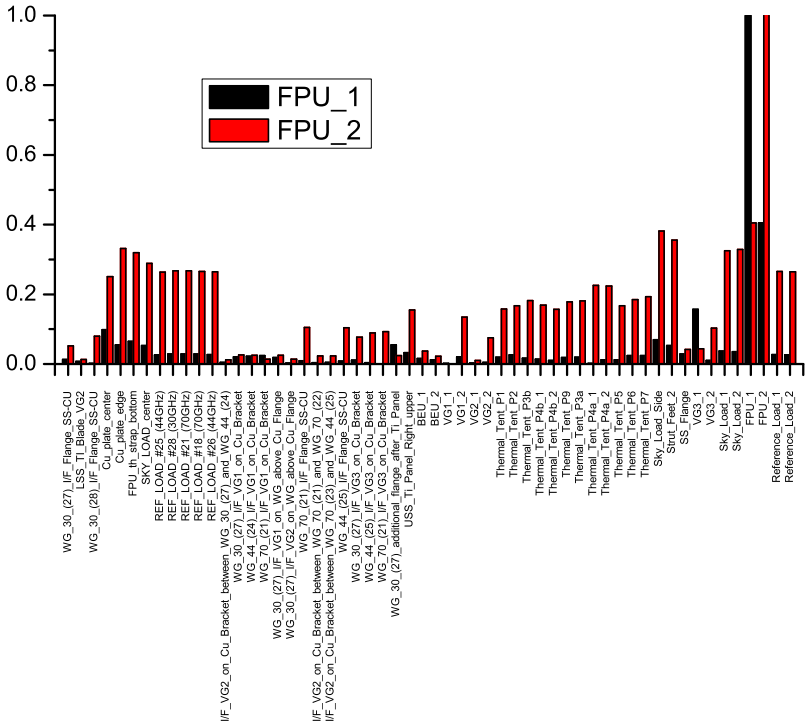

Figure 9: Correlation with the FPU temperaure. The FPU control stage is weakly affected by environmental instability.

Sensor Id	Average T (K)	ΔT_{p-p} (K)
FPU_Right_Bottom_FH28	26.4189	0.04134
FPU_Cone_Right_Part	27.7654	0.06212
FPU_Right_Side_Wall	27.2080	0.04667
FPU_Cold_Plate_Far_Right	25.7702	0.02069
FPU_FH28_Flange	26.1853	0.02395
FPU_Right_Bottom_FH26	26.5363	0.03294
FPU_Left_Side_Wall	25.1834	0.03168
FPU_Cold_Plate_Left_Inner	25.0644	0.03168
FPU_Cold_Plate_Right_Inner	25.6520	0.03976
FPU_Left_Bottom_FH25	25.6777	0.03976
FPU_Cold_Plate_Far_Left	25.1313	0.02451
FPU_Cone_Left_Part	25.5860	0.01982
BEU_Service	47.3434	0.88863
BEU_Science1	47.0814	0.87951
BEU_Science2	49.0413	0.89765
BEU_Science3	47.6113	0.88863
BEU_Science4	49.9698	0.87956

BEU_L_BEM_1	37.2483	0.57432
BEU_L_BEM_2	38.0733	0.50672
BEU_L_FEM_1	42.2284	0.54055
BEU_L_FEM_2	38.1711	0.56305
BEU_L_DAQ_1	37.3191	0.48421
BEU_R_BEM_1	36.3360	0.47295
BEU_R_BEM_2	35.4583	0.49547
BEU_R_FEM_1	40.6417	0.58556
BEU_R_FEM_2	37.0496	0.55170
BEU_R_DAQ_1	37.8117	0.47295
BEU_1	307.943	0.04226
BEU_2	309.951	0.43737
VG1_1	183.999	0.02286
VG1_2	179.310	0.06440
VG2_1	106.199	0.03162
VG2_2	106.529	0.12852
Thermal_Tent_P1	69.5557	0.66024
Thermal_Tent_P2	64.5104	0.42901
Thermal_Tent_P3b	61.4660	0.39138
Thermal_Tent_P4b_1	42.7669	0.23844
Thermal_Tent_P4b_2	45.2058	0.26141
Thermal_Tent_P9	70.4996	0.41156
Thermal_Tent_P3a	61.8007	0.39076
Thermal_Tent_P4a_1	43.1057	0.27981
Thermal_Tent_P4a_2	45.5159	0.30693
Thermal_Tent_P5	61.5262	0.38765
Thermal_Tent_P6	60.1556	0.39642
Thermal_Tent_P7	59.3617	0.38401
Sky_Load_Side	21.2405	0.08512
Strut_Feet_2	24.0928	0.05874
SS_Flange	70.7553	0.33678
VG3_1	59.4999	0.16227
VG3_2	63.4666	0.18741
Sky_Load_1	18.5633	0.11266
Sky_Load_2	18.5474	0.11356
FPU_1	25.4999	0.01566
FPU_2	25.8594	0.01196
Reference_Load_1	22.0591	0.07856
Reference_Load_2	22.0515	0.07921
WG_30_27_IF_Flange_SS_CU	28.2441	0.03098
LSS_TI_Blade_VG2	153.730	0.35693
WG_30_28_IF_Flange_SS_CU	29.0919	0.02802
Cu_plate_center	16.3866	0.19202
Cu_plate_edge	20.9548	0.08095
FPU_th_strap_bottom	21.4173	0.06401
SKY_LOAD_center	29.2524	0.12199
REF_LOAD_25_44GHz	22.0832	0.08207
REF_LOAD_28_30GHz	22.0575	0.07993
REF_LOAD_21_70GHz	22.1082	0.08310
REF_LOAD_18_70GHz	22.1153	0.07906
REF_LOAD_26_44GHz	22.0610	0.08101
IF_VG2_on_Cu_Bracket_between_WG_30_27_and_WG_44_24	147.268	0.27291
WG_30_27_IF_VG1_on_Cu_Bracket	199.837	0.15609

WG_44_24_IF_VG1_on_Cu_Bracket	199.309	0.16706
WG_70_21_IF_VG1_on_Cu_Bracket	195.110	0.12608
WG_30_27_IF_VG1_on_WG_above_Cu_Flange	194.730	0.17093
WG_30_27_IF_VG2_on_WG_above_Cu_Flange	143.220	0.26494
WG_70_21_IF_Flange_SS_CU	30.1667	0.03501
IF_VG2_on_Cu_Bracket_between_WG_70_21_and_WG_70_22	148.518	0.27002
IF_VG2_on_Cu_Bracket_between_WG_70_23_and_WG_44_25	149.659	0.27194
WG_44_25_IF_Flange_SS_CU	29.9502	0.03501
WG_30_27_IF_VG3_on_Cu_Bracket	83.6405	0.12608
WG_44_25_IF_VG3_on_Cu_Bracket	77.1911	0.10595
WG_70_21_IF_VG3_on_Cu_Bracket	73.7764	0.09100
WG_30_27_additional_flange_after_Ti_Panel	27.4395	0.01393
USS_Ti_Panel_Right_upper	37.8942	0.12500

Table 1: Summary of temperature sensor data (including data in the LFI housekeeping) in the ST1_0001 data set.

3.2.2 The sky load thermal behaviour

During the tests some anomalies in the sky load temperature sensors' data were noticed. In particular:

- The temperature difference between the SKY_LOAD_CENTER, located on the central pyramid, and SKY_LOAD_1(2), located on the Aluminum support was higher (about 10 K) than expected (and measured in a dedicated test on a representative setup, see report in annex 1).

- the pyramid sensors was susceptible to daily temperature variations (likely to be linked to BEU temperature variations) as shown in Fig. 3.2.2. The high frequency behaviour of the pyramid shows how the conductive link to the Al base is less efficient than other heat exchanges with the environment, as also remarked in the correlation plot in Fig. 3.2.2.

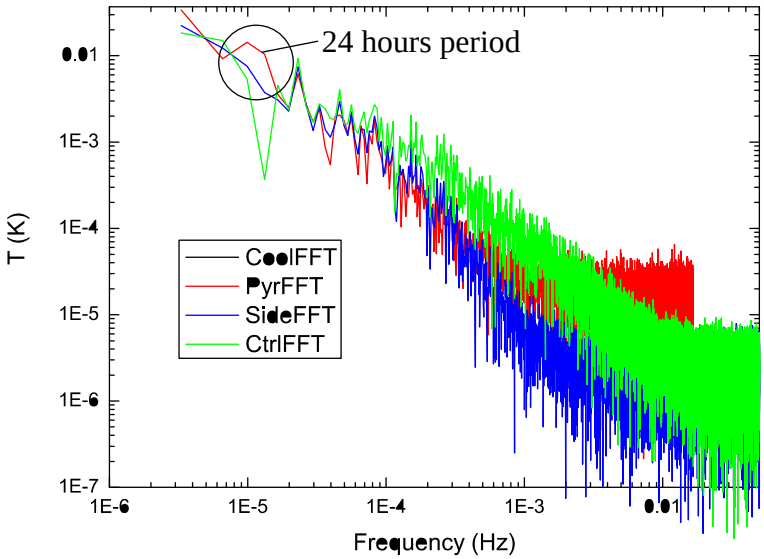

Figure 10: Spectral analysis of temperature measured by the sky load sensors.

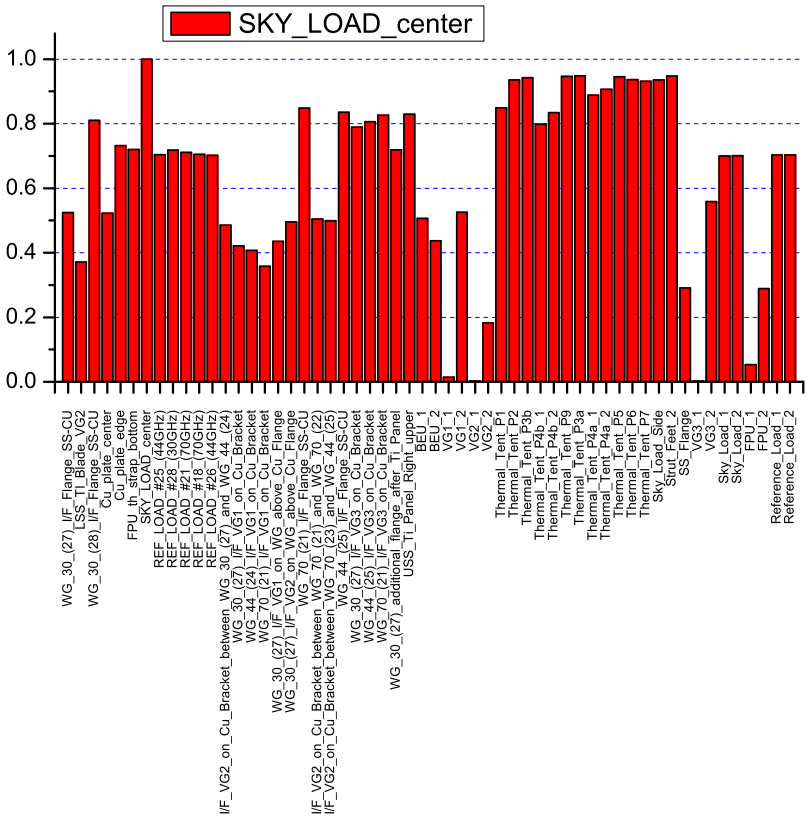

Figure 11: Correlation coefficients of the sky load central pyramid sensor with other sensors in the chamber. It is evident how the thermal tents correlate to it better than the sky control.

Two possible heat inputs to the sensor on the pyramid could be considered, with comparable values:

- The radiative worst case of a homogeneous 70 K shroud has a heat load of about 0.396 mW on a pyramid with ideal emissivity
- The conductive load of the sensor leads thermalized at 70 K (thermal tent P1 panel) is of about 0.181 mW

Taking into account that the warmer panels of the shroud are P1, which is the bottom shroud, and P9, whose sight towards the pyramids is covered with an MLI shield surrounding FPU thermal

straps, while the vertical line of sight of the pyramid is covered mainly by the 25 K FPU, a reduced radiative heat load can be actually estimated. The average temperature of the remaining panels is about 56 K, which corresponds to a 0.154 mW load.

The sensor located on the side of the load is not responding as expected to temperature variations as showed in the Fig. 3.2.2. The sensor is stabilizing at a colder temperature with respect to the Al base.

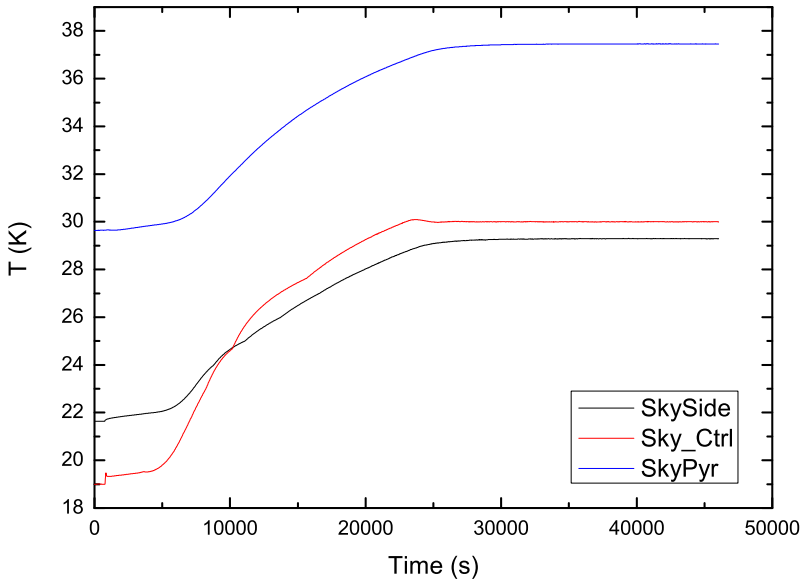

Figure 12: Temperature data for sky control (black), sky side (red) and central pyramid (blue) during a sky load step. The sky side curve crosses the sky base one.

4 Instrument functionality

4.1 Introduction

Tests described in this section regard the functionality of the instrument, with especial focus on radiometers health and behaviour. They have demonstrated to be a very important step in the LFI understanding: moreover, they have been essential in the investigation of failures and non ideal behaviours. Their power has been fully recognized and understood only with the test campaign already running: actually, those tests that were firstly thought only as a qualitative verification of the LFI functioning, if everything works properly, revealed to have a much stronger valence when the instrument showed non ideal behaviours or failures.

Test here described are those foreseen in the test plan ([AD4]), in warm (named AMB_01 and AMB_02) and cold (CRYO_01) conditions. In addition to these tests, some others have been added (and are discussed here) to investigate several non ideal behaviours that showed up during the test campaign.

The main objectives of the radiometers functional test campaign have been:

- to verify the LNA bias settings;
- to verify the LNA drain currents corresponding to input biases: this is the only housekeeping parameter truly measured in the FEM;
- to verify the saturation level of the DAE AD converter;
- to verify the phase switches functionality;
- to verify the correct sky/reference identification;
- to compare functionality between warm and cold conditions;
- to compare functionality in warm conditions between beginning and end of the test campaign.

Secondary, but not less important, objectives have been:

- switch ON procedures;
- monitoring of drain current stability;
- monitoring of scientific signal stability and noise properties;
- check for failures in the RF and DC receiver parts;
- check for failures or non ideal response in the DAE. This part is treated in detail in Annex **add reference and annex**

4.2 Experimental conditions

Tests have been run mainly in two configurations:

- LFI mounted on the EGSE, outside the cryochamber;
- LFI mounted inside the cryo-chamber.

In both configurations, the characteristic parameters of the harness have been supposed to be the same and representative of the flight setup at satellite level. A strong limitation in the recovery of the bias voltages at FEM level is represented by the fact that the voltage is known at the level of the DAE so that a residual uncertainty remains on the estimate of the actual FEM bias values.

Only drain currents are really measured at FEM level: that is why they have been considered as the figure of merit to check the LNAs true setup.

Other general setup conditions influencing the parameters under monitoring are:

1. the FPU temperature: it has an effect on FEM drain currents, $I_{\rm d}$, gain and noise temperature (radiometric voltage output, $V_{\rm out}$), depending on the specific channel. Generally, $I_{\rm d}$ and $V_{\rm out}$ have been observed to be directly proportional to the FPU temperature;
2. the BEU temperature: effects temperature changes at BEMs level are different depending on the channel. The overall effect reflects in all cases as a change in $V_{\rm out}$. In particular, BEU temperature increasing produces:

- voltage increasing (as a combination of BEM gain and stand-alone response) in 30 and 44 GHz RCAs;
- voltage decreasing (especially as a BEM stand-alone response) in 70 GHz RCAs.

3. The sky and reference loads temperature;

4. then DAE temperature, which may have an impact on the DAE calibration tables if the DAE gain and offset are significantly different from 1 and 0 respectively (which was never the case for functionality tests).

Other differences (probably due to the slightly different grounding and to the environmental conditions) can be observed depending on the LFI is operated outside (on the MGSE) or inside the cryochamber (and also in this situation some differences can be observed from vacuum to room pressure conditions). Unfortunately, in most of the warm functional tests (all those performed outside the cryochamber) the FPU temperature and the temperatures of the loads have not been monitored, since no sensor was foreseen for these conditions. For completeness, it must be added that tests have been often performed under different thermal setup of the BEU and/or in non stationary thermal conditions: it increased the difficulty to compare between absolute results from tests, only nominally performed with the same setup.

About harness, it must be noted here that all channels belonging to the same power group are interconnected: a bias change operated on a channel reflects, with various weights, also on others. In some cases, this link (represented by the mass return common line) has been observed also between channels belonging to different power groups. This is why different bias tables are needed to power FEMs under different switch on configurations; moreover, since the power provided by the DAE is limited, this sharing produces a voltage drop when all the LFI is on, causing in some cases a very weak scientific output when the LFI is warm (FEM gain decreases with temperature icreasing).

4.3 Test flow

A summary of the main test performed, useful at least for the purpose of this section, is presented in Tab. 2.

Table 2: Functional test flow summary. Tests have been divided into three phases logically separated. Cooling down divides STEP 1 and 2; warm-up separates STEP 2 and 3. During STEP 3 several actions have been performed: instrument removal from cryo-chamber, RCA 24 repair and RCA 18 refurbishment, mounting of wire-protecting metal shields on 70 GHz FEMs, and problem fixing. Final pre-shipment tests. RBEM2 temperature has been taken to compare between tests, since this parameter was always recorded and seems to be in some way representative of the environmental behaviour. Data from sensors containing information on FPU and LOADs temperature have not been recorded apart from in a few tests performed inside the cryo-chamber.

TEST SECTION	TEST	NAME	OBJECTIVE	CRYOCHAMBER	MGSE	T (RBEM2)	T(FPU)	CHANNELS	PW BEM	FAILURES	NON IDEALITIES	
STEP 1	AMB_01	AMB_0016	WARM ACAs FUNCTIONALITY	NO	YES	23-26.6	UNK	ALL	ALL	RCA 24-VG1 (M1)		
	AMB_02	AMB_0052	WARM LFI FUNCTIONALITY	YES	NO	24-26.3	UNK	ALL	ALL	RCA 24-VG1 (M1)	RCA 23 Id DROP	
		AMB_0028	DEBUGGING								RCA 23 Id DROP	
COOLDOWN												
STEP 2	CRYO_01	XXX_0019	COLD ACAs FUNCT	YES	NO			ALL	ALL	RCA 24 VG1 (M1)	RCA 28 SATURATION	RCA 28 SKY/REF
WARMUP										RCA 18 (ph/sw)	RCA 23 HIGH Id	
STEP 3	AMB_01	AMB_0074	WARM ACAs FUNCTIONALITY	YES	NO	39-40.6	299.7	ALL	ALL	RCA 24-VG1 (M1)		RCA 28 SKY/REF
										RCA 18 (ph/sw)		
	AMB_02	XXX_140	WARM LFI FUNCTIONALITY	YES	NO	41.1	300.5	ALL	ALL	RCA 24-VG1 (M1)		
										RCA 18 (ph/sw)		RCA 28 SKY/REF
RCA 24 & 18 recovery, metal shields on 70 GHz												
	AMB_02	AMB_0079	WARM LFI FUNCTIONALITY	NO	YES	20.5-23.5		ALL (5)	ALL	RCA 19, 20, 21	RCA 23 BURST NOISE	RCA 28 SKY/REF
metal shields removed from RCA 19,20		AMB_0083	WARM LFI FUNCTIONALITY	NO	YES	21.4-20.2		18-26	PW group			
		AMB_0084	WARM LFI FUNCTIONALITY	NO	YES	21.4-20.2		23-25	PW group		RCA 23 BURST NOISE	
		AMB_0085	WARM LFI FUNCTIONALITY	NO	YES	21.4-20.2		19-20-28	PW group			RCA 28 SKY/REF
		AMB_0086	WARM LFI FUNCTIONALITY	NO	YES	21.4-20.2		27-24-21-22	PW group	RCA 21		
		AMB_0090	WARM LFI FUNCTIONALITY	NO	YES	19.0-23.1		ALL	ALL	RCA 21	RCA 23 BURST NOISE	RCA 28 SKY/REF
met shields removed from RCA 21												
		AMB_0093	WARM LFI FUNCTIONALITY	NO	YES			ALL	ALL		RCA 23 BURST NOISE	RCA 28 SKY/REF
metal shields problem fixed											RCA 23 Id DROP	RCA 28 SKY/REF
PRE SHIPMENT FINAL TESTS	AMB_01	AMB_0100		NO	YES	20.5-25.9		ALL	ALL		RCA 23 BURST NOISE	RCA 28 SKY/REF
	AMB_02	AMB_0101		NO	YES	25.4-26.2		ALL	ALL		RCA 23 BURST NOISE	RCA 28 SKY/REF

These tests can be divided in three parts:

- first warm functional test (AMB_01 and AMB_02): the LFI is switched on warm, using RCA warm biases, and its functionality is investigated. During this test, RCA 24 failure in the V_{g1} stage was found. RCA 23 I_d instability was found.
- Cryogenic functionality (CRYO_01): the LFI is switched on with "non optimised" bias, calculated taking into account the cryo-harness drop related with the operative temperature. Functionality is investigated and problems found at warm level have been checked again in order to understand if they present in occurrence with specific bias settings / temperature. During this test RCA 24 still showed the failure. In add, RCA 18 showed a phase switch failure. Furthermore the output of RCA 28 showed oscillations that impacted on all LFI output inducing spurious fluctuations. Also identification of sky/reference samples was not successful for all channels.
- Warm functional tests after cryo calibrations (AMB_01, AMB_02) : they are the final functional tests. This section has been maybe the most complicated during the test campaign and took a long time to be completed. It can be divided in three steps.

  1. Warm functionality at the end of cryogenic tests (instrument still in the cryo facility, RCA 24 and RCA 18 were still not working)
  2. Warm functionality after RCA 24 recovery and RCA 18 half-FEM refurbishment. Here an apparent failure was found on RCA 19 (V_{g2}) , 20 (phase switch) , 21 (phase switch). These failure were subsequently understood to be caused by bias wires damaged by the insertion of metal protecting plates on 70 GHz FEMs. Furthermore non idealities in the output from RCA23-R0D0 (Burst noise) was also observed.
  3. Final warm functional tests (before shipment): all failures were recovered. Burst noise still observed on RCA 23.

4.4 Results

4.4.1 Step1: first warm tests

Data are taken from files AMB_0016 and AMB_0052, corresponding to tests AMB_01 and AMB_02 foreseen by the test plan. Here the LFI was switched on for the first time with bias values evaluated from specifications given at RCA level and taking into account an estimate of the voltage drop in the cryo harness.

In Tables 3 and 4 we report the details of measurements performed in these tests. For each channel, a simple symmetry test has been performed in order to investigate the Phase switches health. If we name V_{1S}, V_{1R} and V_{1S}, V_{1R} the sky and ref outputs from the two legs (1 and 2) of one half FEM, phase switch amplitude balance must yield $(V_{1S} + V_{1R})/(V_{1R} + V_{1S}) \sim 1$. Unity means that phase switch is perfectly balanced; a large deviation from unity suggests a problem in the phase switch. Results can be found in column PH/SW in table 2 and 3.

Test AMB_0016 showed that all phase switches are behaving properly (separation is observed for all channels corresponding to the final bias reported in TAB2: these bias are in some cases the result of some changes in phase switch drain currents, able to produce separation). It must be highlighted here that, at this step of the functionality tests, the phase switch diode D2-M1 of RCA 18 was properly working: it is clearly shown in Fig 13.

Regarding RCA 24 it was not clear if already at this stage there was a problem in the V_{g1} line of the M1 branch (a failure that was confirmed in later tests). A possible indication of failure came from the AMB_0052 in which I_d (M1) was significantly lower than I_d (M2) (see Tab. 4.

Table 3: AMB_01 (from file AMB_0016); on the left side bias (input) and drain currents (measured) are indicated. On the right side scientific voltages (V_{out}) on different channels, when each ACA is switched on separately. V_{out} is recorded in "chopped" conditions (A/C 4KHz switched ON , B/D state 0). Index "i" means "0" for M (main) channels and "1" for S (side) channels. BEM voltage (with BEM only switched ON, FEM OFF) is also given, corresponding to each diode.

RCA #	Detector ID		SCOS Parameter	VG1 DEC	VG2 DEC	VD DEC	I1 DEC	I2 DEC	SCOS Parameter	Expecte d Id (mA)	ACA ON	i-0 SKY Volt	i-0 REF Volt	i-0 PH/SW	i-1 SKY Volt	i-1 REF Volt	i-1 PH/SW		BEM ON
CH27	00	00	LP001320	234	114	234	205	205	LM051322	21.39	M1	2.160	2.140	0.998	2.360	2.390	1.000	00	0.0311
	01	01	LP002320	234	114	232	205	205	LM052322	21.1	M2	2.570	2.540		2.490	2.520		01	0.0364
	02	10	LP003320	234	115	238	205	205	LM053322	21.89	S1	2.291	2.240	1.007	1.870	1.900	0.995	10	0.0367
	03	11	LP004320	234	114	233	205	205	LM054322	21.39	S2	2.150	2.130		1.750	1.760		11	0.0317
CH24	04	00	LP005320	229	229	255	205	205	LM055322	31.95	M1	0.021	0.020	1.007	0.018	0.019	0.994	00	0.005
	05	01	LP006320	229	229	255	205	205	LM056322	32.66	M2	0.012	0.012		0.012	0.013		01	0.0061
	06	10	LP007320	230	230	255	205	205	LM057322	33.74	S1	0.006	0.005	1.000	0.007	0.007	1.006	10	0.0048
	07	11	LP008320	230	230	255	205	205	LM058322	33.9	S2	0.007	0.006		0.008	0.009		11	0.0066
CH21	08	00	LP009320	173	134	255	255	255	LM059322	24.17	S2	0.263	0.257	1.002	0.236	0.240	1.000	00	0.0083
	09	01	LP010320	122	119	255	255	255	LM060322	24.11	S1	0.178	0.173		0.159	0.163		01	0.0077
	0A	10	LP011320	156	135	255	255	255	LM061322	24.23	M1	0.0978	0.0930	1.009	0.0958	0.1007	0.990	10	0.0151
	0B	11	LP012320	153	120	255	255	255	LM062322	24.24	M2	0.0714	0.0680		0.0671	0.0704		11	0.0189
CH22	0C	00	LP013320	120	126	255	255	255	LM063322	22.68	S2	0.328	0.304	1.017	0.386	0.415	0.981	00	0.0181
	0D	01	LP014320	96	78	255	255	255	LM064322	23.07	S1	0.293	0.279		0.339	0.354		01	0.0158
	0E	10	LP015320	108	78	255	255	255	LM065322	22.7	M1	0.304	0.286	1.014	0.353	0.376	0.987	10	0.0129
	0F	11	LP016320	96	76	255	255	255	LM066322	22.94	M2	0.284	0.274		0.325	0.339		11	0.0166
CH23	10	00	LP017320	114	81	255	255	255	LM067322	23.70	S2	1.073	1.103	0.996	0.556	0.542	1.001	00	0.0422
	11	01	LP018320	99	78	255	255	255	LM068322	22.42	S1	0.898	0.920		0.4888	0.476		01	0.0482
	12	10	LP019320	94	84	255	255	255	LM069322	22.28	M1	0.494	0.495	1.021	0.577	0.571	0.982	10	0.0627
	13	11	LP020320	135	130	255	255	255	LM070322	22.50	M2	0.780	0.808		1.055	1.019		11	0.0296
CH25	14	00	LP021320	229	228	255	205	205	LM071322	30.02	M1	0.093	0.089	0.978	0.094	0.098	1.026	00	0.0067
	15	01	LP022320	228	228	255	205	205	LM072322	29.37	M2	0.142	0.133		0.129	0.139		01	0.0064
	16	10	LP023320	229	229	255	205	205	LM073322	30.96	S1	0.032	0.030	1.012	0.025	0.026	1.000	10	0.0062
	17	11	LP024320	230	229	255	205	205	LM074322	31.43	S2	0.028	0.027		0.026	0.027		11	0.0047
CH28	18	00	LP025320	234	114	243	206	205	LM075322	20.5	M1	1.490	1.470	0.991	1.960	1.980	1.005	00	0.025
	19	01	LP026320	234	115	240	205	206	LM076322	22.79	M2	1.960	1.910		2.240	2.280		01	0.0311
	1A	10	LP027320	233	115	241	205	206	LM077322	23.39	S1	2.430	2.390	1.002	2.130	2.160	0.998	10	0.0263
	1B	11	LP028320	234	115	244	206	205	LM078322	23.08	S2	2.580	2.550		2.250	2.270		11	0.0268
CH20	1C	00	LP029320	112	88	255	255	255	LM079322	23.44	S2	0.393	0.380	1.007	0.420	0.437	0.990	00	0.0198
	1D	01	LP030320	72	132	255	255	255	LM080322	23.18	S1	0.369	0.361		0.388	0.397		01	0.0213
	1E	10	LP031320	87	114	255	255	255	LM081322	22.87	M1	0.309	0.298	0.997	0.291	0.302	1.003	10	0.0219
	1F	11	LP032320	105	132	255	255	255	LM082322	23.16	M2	0.344	0.331		0.317	0.330		11	0.0202
CH19	20	00	LP033320	69	75	255	255	255	LM083322	22.6	S2	0.291	0.283	0.995	0.259	0.264	1.005	00	0.0136
	21	01	LP034320	117	108	255	255	255	LM084322	23.07	S1	0.363	0.352		0.362	0.370		01	0.0219
	22	10	LP035320	132	135	255	255	255	LM085322	22.98	M1	0.292	0.277	1.017	0.293	0.307	0.984	10	0.0161
	23	11	LP036320	75	129	255	255	255	LM086322	23	M2	0.206	0.199		0.209	0.215		11	0.0210
CH18	24	00	LP037320	130	84	255	255	255	LM087322	22.48	S2	0.463	0.475	1.002	0.453	0.441	0.996	00	0.0415
	25	01	LP038320	87	132	255	255	255	LM088322	22.28	S1	0.345	0.359		0.375	0.360		01	0.0414
	26	10	LP039320	108	99	255	255	255	LM089322	22.02	M1	0.574	0.573	1.016	0.767	0.769	0.983	10	0.0341
	27	11	LP040320	118	132	255	255	255	LM090322	22.56	M2	0.623	0.641		0.897	0.871		11	0.0421
CH26	28	00	LP041320	229	228	255	205	205	LM091322	29.5	M1	0.059	0.056	1.029	0.063	0.067	0.973	00	0.0054
	29	01	LP042320	229	228	255	205	205	LM092322	30.28	M2	0.032	0.031		0.040	0.041		01	0.0065
	2A	10	LP043320	229	228	255	205	205	LM093322	29.75	S1	0.076	0.073	1.005	0.082	0.086	0.991	10	0.0067
	2B	11	LP044320	229	228	255	205	205	LM094322	30.08	S2	0.053	0.050		0.052	0.055		11	0.0067

Table 4: AMB_02 (from file AMB_0052); on the left side bias (input) and drain currents (measured) are indicated. On the right side scientific voltages ($V_{\rm out}$) on different channels, when all LFI is switched on simultaneously. $V_{\rm out}$ is recorded in "chopped" conditions (A/C 4KHz switched ON , B/D state 0). BEM voltage (with BEM only switched ON, FEM OFF) is also given, corresponding to each diode. Phase switches symmetry test is reported in the rightmost column.

RCA #	Detector ID		SCOS Parameter	VG1 DEC	VG2 DEC	VD DEC	I1 DEC	I2 DEC	SCOS Parameter	Expected Id (mA)	LFI ON	A/C SW SKY Volt	A/C SW REF Volt	PH/SW
CH27	00	00	LP001320	250	130	255	261	261	LM051322	18.54	00	1.550	1.566	0.985
	01	01	LP002320	250	130	255	261	261	LM052322	18.3	01	1.606	1.573	
	02	10	LP003320	250	130	255	261	261	LM053322	18.76	10	1.238	1.248	0.990
	03	11	LP004320	250	130	255	261	261	LM054322	18.45	11	0.987	0.975	
CH24	04	00	LP005320	241	241	255	205	205	LM055322	25.25	00	0.008	0.008	1.000
	05	01	LP006320	241	241	255	205	205	LM056322	23.15	01	0.009	0.009	
	06	10	LP007320	241	241	255	205	205	LM057322	25.71	10	0.005	0.005	1.008
	07	11	LP008320	241	241	255	205	205	LM058322	25.72	11	0.007	0.007	
CH21	08	00	LP009320	217	178	255	255	255	LM059322	17.79	00	0.026	0.026	1.006
	09	01	LP010320	118	163	255	255	255	LM060322	15.69	01	0.024	0.024	
	0A	10	LP011320	133	178	255	255	255	LM061322	15.69	10	0.050	0.050	1.004
	0B	11	LP012320	151	163	255	255	255	LM062322	16.85	11	0.049	0.049	
CH22	0C	00	LP013320	166	172	255	255	255	LM063322	16.7	00	0.066	0.068	0.968
	0D	01	LP014320	142	124	255	255	255	LM064322	16.37	01	0.056	0.054	
	0E	10	LP015320	154	124	255	255	255	LM065322	16.23	10	0.069	0.071	0.956
	0F	11	LP016320	142	121	255	255	255	LM066322	16.31	11	0.065	0.061	
CH23	10	00	LP017320	153	121	255	255	255	LM067322	15.45	00	0.113	0.113	0.994
	11	01	LP018320	149	128	255	255	255	LM068322	16.16	01	0.131	0.130	
	12	10	LP019320	143	134	255	255	255	LM069322	16.08	10	0.182	0.186	0.982
	13	11	LP020320	185	179	255	255	255	LM070322	16.72	11	0.091	0.090	
CH25	14	00	LP021320	242	242	255	205	205	LM071322	23.91	00	0.006	0.006	0.993
	15	01	LP022320	242	242	255	205	205	LM072322	23.46	01	0.008	0.008	
	16	10	LP023320	242	242	255	205	205	LM073322	24.25	10	0.025	0.024	1.020
	17	11	LP024320	242	242	255	205	205	LM074322	24.5	11	0.026	0.026	
CH28	18	00	LP025320	247	128	255	261	261	LM075322	20.16	00	0.685	0.743	0.923
	19	01	LP026320	247	128	255	261	261	LM076322	19.78	01	0.912	0.843	
	1A	10	LP027320	246	128	255	205	206	LM077322	20.15	10	2.337	2.350	1.006
	1B	11	LP028320	247	128	255	206	205	LM078322	19.7	11	2.078	2.117	
CH20	1C	00	LP029320	151	127	255	255	255	LM079322	17.15	00	0.090	0.089	1.011
	1D	01	LP030320	112	172	255	255	255	LM080322	17.17	01	0.086	0.087	
	1E	10	LP031320	126	153	255	255	255	LM081322	16.95	10	0.099	0.098	1.015
	1F	11	LP032320	145	172	255	255	255	LM082322	17.23	11	0.103	0.105	
CH19	20	00	LP033320	109	114	255	255	255	LM083322	16.61	00	0.065	0.064	1.022
	21	01	LP034320	157	148	255	255	255	LM084322	17.16	01	0.072	0.074	
	22	10	LP035320	172	174	255	255	255	LM085322	17.02	10	0.088	0.087	1.012
	23	11	LP036320	115	168	255	255	255	LM086322	16.94	11	0.085	0.086	
CH18	24	00	LP037320	177	132	255	255	255	LM087322	16.3	00	0.109	0.110	0.992
	25	01	LP038320	135	180	255	255	255	LM088322	16.27	01	0.148	0.147	
	26	10	LP039320	156	147	255	255	255	LM089322	15.9	10	0.077	0.078	0.994
	27	11	LP040320	165	129	255	255	255	LM090322	16.22	11	0.087	0.087	
CH26	28	00	LP041320	241	242	255	205	205	LM091322	24.05	00	0.010	0.010	1.000
	29	01	LP042320	242	241	255	205	205	LM092322	23.47	01	0.011	0.011	
	2A	10	LP043320	241	241	255	205	205	LM093322	23.73	10	0.015	0.015	1.000
	2B	11	LP044320	241	241	255	205	205	LM094322	23.53	11	0.016	0.016	

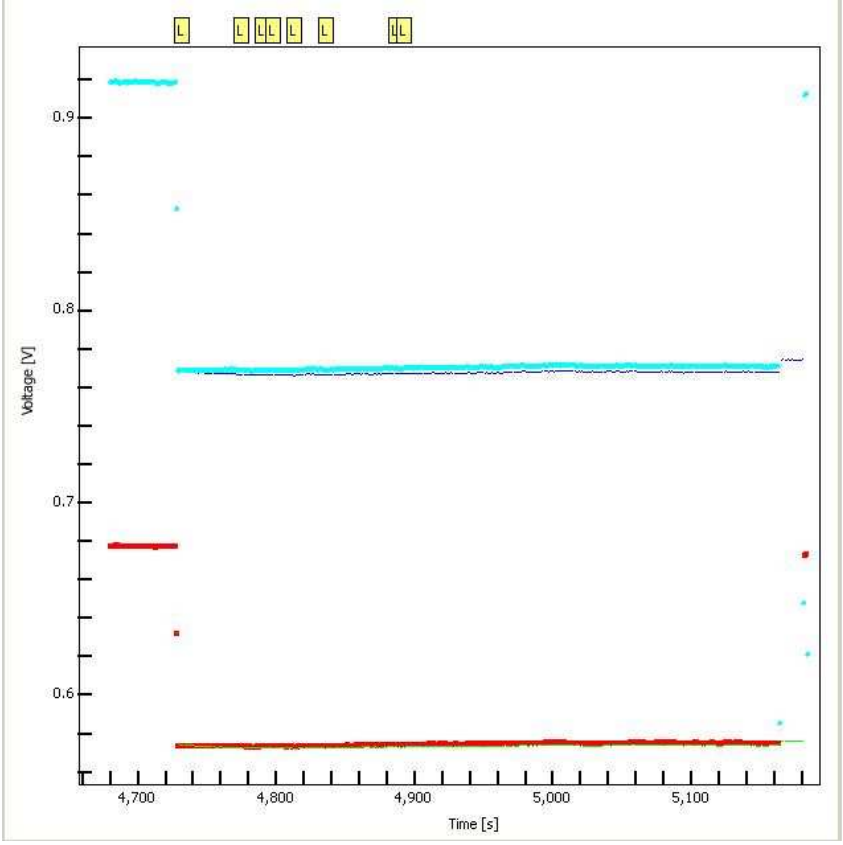

Figure 13: RCA 18 M1; phase switch functionality test. When the 4KHz is enabled on AC, both traces (sky and ref) are non null for each BEM diode (00 and 01): also if traces seem to be not well separated (their difference is about 1 mV on R0D0 and 2 mV on R0D1) this scenario is well different from that shown in the cold functional tests where the problem was firstly observed) and in the last warm functional tests (until test AMB_0079, where half fem was refurbished).

4.4.2 Step2: cryo functionality tests

Bias settings The first difficulty was found in finding the bias setup able to reproduce RCA conditions. The theoretical cryo-harness resistance R (foreseen from AAS thermo-electric model) was not able to provide the expected $I_{\rm d}$ currents when the FEMs were powered with specific bias. Drain currents were in many cases higher than expected: they have been then used to correct the R parameter: correction was applied by power groups and its effect was the same of an offset subtraction from bias.

Cold functional tests are based on these corrected bias tables, able to provide the expected drain currents but in one case : RCA 23 (detector 11) $I_{\rm d}$ remained still high also after correction.

The switch ON bias settings and currents measured in the CRYO_01 test (dataset XXX_0019) are reported in 5.

Table 5: CRYO_01 (from file XXX_0019); bias (input) and drain currents (measured) are indicated. Column I1-bis refers to changes applied to phase switch current I1 to highlight sky-ref separation. To be noted RCA 23 S2 (detector 11) drain current much higher than in the other legs of the same FEM.

RCA #	Detector ID		SCOS Parameter	VG1 DEC	VG2 DEC	VD DEC	I1 DEC	I1-bis DEC	I2 DEC	SCOS Parameter	Expected Id
CH27	00	00	LP001320	242	109	152	153	100	205	LM051322	10.06
	01	01	LP002320	242	110	153	178	60	204	LM052322	7.95
	02	10	LP003320	241	94	153	151		179	LM053322	8.74
	03	11	LP004320	242	123	152	153		179	LM054322	8.47
CH24	04	00	LP005320	227	221	179	126		253	LM055322	13.08
	05	01	LP006320	227	220	179	152		252	LM056322	10.76
	06	10	LP007320	223	221	148	126		249	LM057322	13.55
	07	11	LP008320	215	221	154	127		252	LM058322	13.3
CH21	08	00	LP009320	191	207	127	255		255	LM059322	13.22
	09	01	LP010320	186	181	122	255		255	LM060322	13.22
	0A	10	LP011320	187	191	131	255		255	LM061322	13.08
	0B	11	LP012320	186	181	127	255		255	LM062322	14.25
CH22	0C	00	LP013320	185	192	123	255	100	255	LM063322	10.42
	0D	01	LP014320	182	178	122	255	100	255	LM064322	11.92
	0E	10	LP015320	182	182	118	255		255	LM065322	15.8
	0F	11	LP016320	183	185	125	255		255	LM066322	15.8
CH23	10	00	LP017320	190	193	124	255		255	LM067322	13.18
	11	01	LP018320	196	196	119	255		255	LM068322	21.9
	12	10	LP019320	193	187	121	255		255	LM069322	12.68
	13	11	LP020320	196	190	120	255	150	255	LM070322	11.50
CH25	14	00	LP021320	228	220	180	152		252	LM071322	12.05
	15	01	LP022320	228	217	182	153		249	LM072322	11.66
	16	10	LP023320	224	221	163	153		180	LM073322	12.75
	17	11	LP024320	224	221	162	126		178	LM074322	12.78
CH28	18	00	LP025320	245	89	155	127		181	LM075322	10.10
	19	01	LP026320	245	131	154	128		180	LM076322	10.48
	1A	10	LP027320	237	94	156	127		255	LM077322	9.36
	1B	11	LP028320	245	123	156	128		255	LM078322	10.91
CH20	1C	00	LP029320	189	201	123	255		255	LM079322	18.7
	1D	01	LP030320	189	201	129	255		255	LM080322	14.75
	1E	10	LP031320	189	199	118	255		255	LM081322	15.85
	1F	11	LP032320	189	202	123	255		255	LM082322	15.07
CH19	20	00	LP033320	190	200	124	255		255	LM083322	14.75
	21	01	LP034320	196	200	118	255		255	LM084322	15.2
	22	10	LP035320	188	194	118	255		255	LM085322	12.86
	23	11	LP036320	200	189	121	255		255	LM086322	14.01
CH18	24	00	LP037320	192	208	117	255		255	LM087322	20.75
	25	01	LP038320	192	190	142	255		255	LM088322	18.05
	26	10	LP039320	193	193	118	255		255	LM089322	12.06
	27	11	LP040320	187	195	120	255	200	255	LM090322	13.61
CH26	28	00	LP041320	193	227	168	152		253	LM091322	14.54
	29	01	LP042320	192	216	170	178		230	LM092322	10.59
	2A	10	LP043320	236	234	166	153		249	LM093322	14.54
	2B	11	LP044320	233	255	172	179		252	LM094322	10.6

Non idealities and failures Cold functionality checks showed non idealities or failures that have been fixed before delivery. Discussion of these failures is presented in this section following chronological order.

RCA 28 saturation

Standard switch on procedure, when applied to RCA 28, produced saturation in the scientific output and an anomalous increasing of currents flowing on several other channels together with the simultaneous increasing of scientific output. Some showed saturation also if not belonging to the same power group of RCA 28 and with the BEM only powered (FEM OFF). This puzzling problem has been partially explained as an oscillation induced by RCA 28 on other channels through the BEU, but was not fully understood. This undesired feature was never observed during warm functional tests.

Nevertheless, a customized switch on procedure was individuated for channel 28, independent on the bias level applied and depending only on the order followed to power on V_{g1} , V_{g2} and V_d belonging to M1 and M2. The application of this procedure allowed to switch on LFI28 systematically with no saturation at all. The "custom" procedure has been incorporated in the script "LFI_switch_ON" called to power ON RCA 28.

RCA 18: phase switch failure

Diode D2 (M1) belonging to RCA 18 showed very high loss suggesting a failure in the phase switch itself (or in the line biasing the phase switch). When the A/C 4KHz was on, scientific output from diodes R0D0 and R0D1 was alternatively non zero and zero. When the 4KHz was activated on B/D no output was observed. The problem was then understood but not solved: the RCA 18 was then operated (until the problem was fixed in the last warm test section) taking advantage of the B/D switching redundancy. However, also in this case the radiometer output was affected by a very poor isolation because of the phase switch failure (the phase shifter plastic board was found broken): Sky-Ref separation was then due to the different loss states (corresponding to the two phase shifter states) instead of to a real difference in the input power.

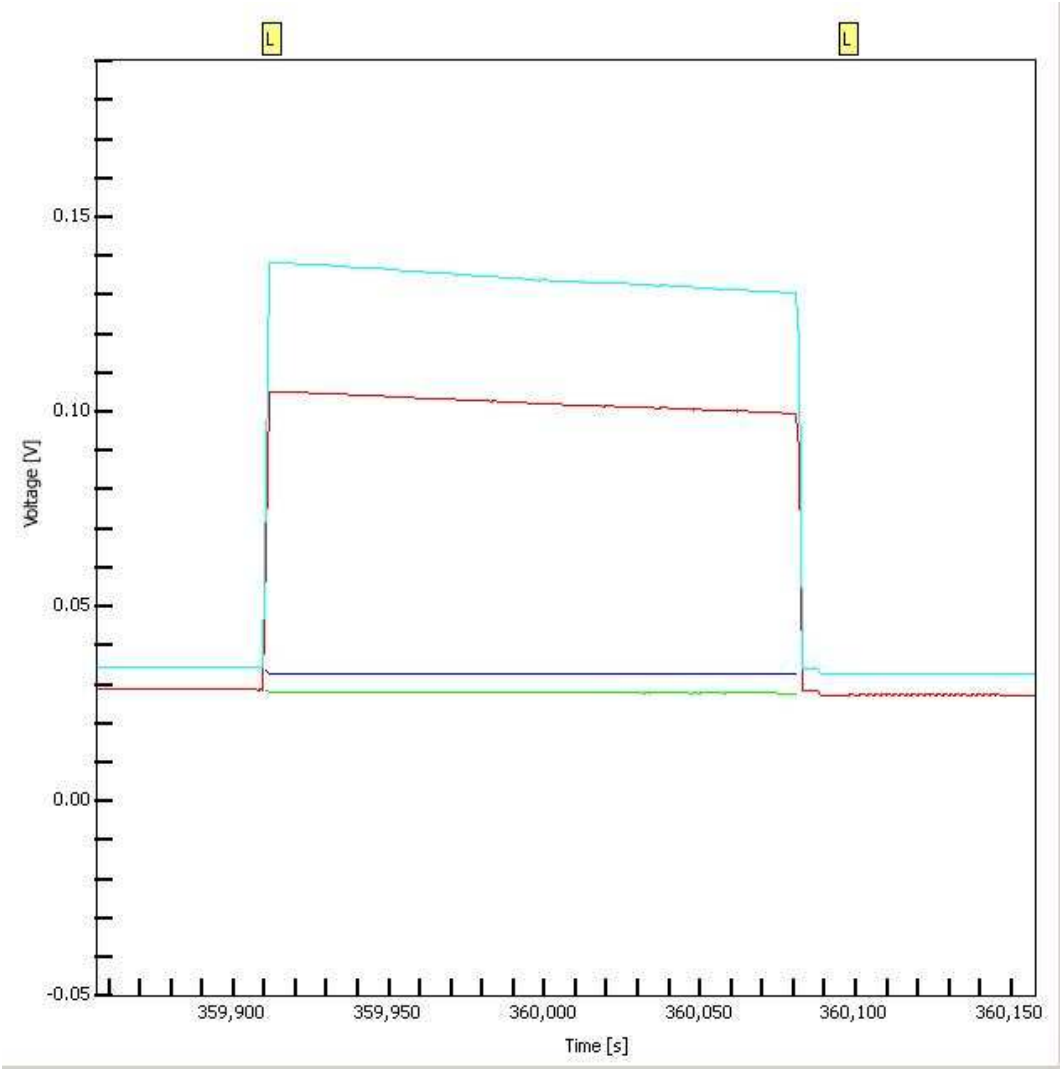

Figure 14: Phase switch failure on RCA 18: no change observed in R0D0-ref and R0D1 sky when 4KHs is activated on A/C with respect to the BEM stand alone level.

RCA 24: V_{g1} failure This failure was discovered when it was apparent that channel M1 was insensitive to V_{g1} changes and that the corresponding drain current was lower than expected. The problem was identified and fixed at the end of the second warm functional test after the calibration campaign. The problem was a short circuit in the V_{g1} stage produced by a glue excess from the pin connectors.

Figure 15: RCA 24-M1: drain current as a function of V_{g1} . Curves correspond to different values of V_d reported in the legend. Response is flat in V_{g1} while I_d increases with V_d .

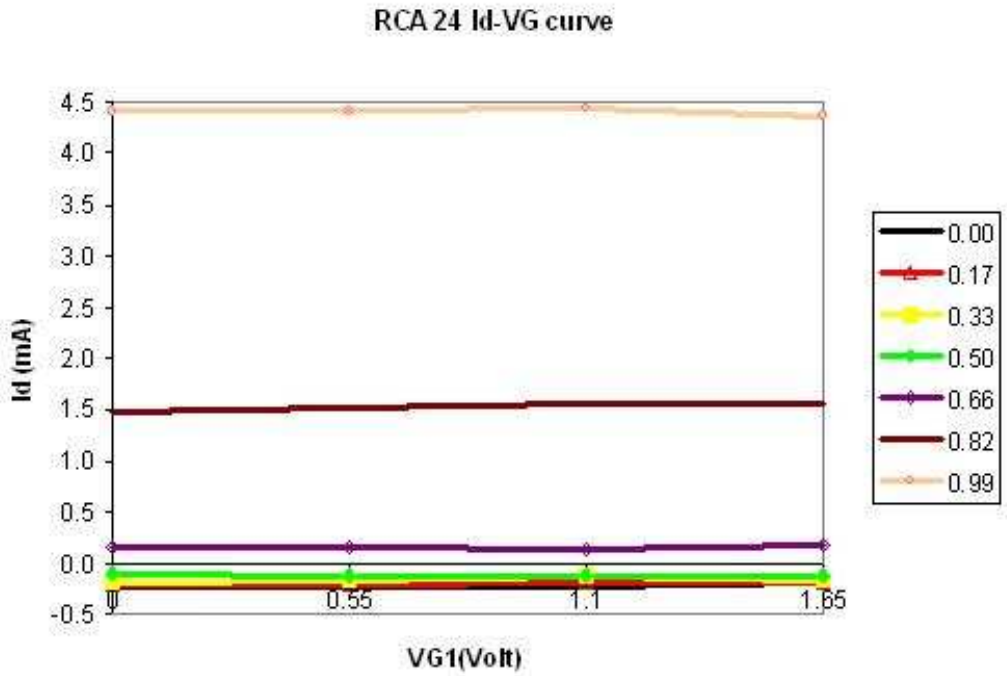

4.4.3 Step 3: second warm tests (after calibration tests)

Debugging problems still open at the end of the calibration campaign. The first test (dataset AMB_0074) was performed with the LFI still in the cryochamber in vacuum conditions with the objective to characterise the instrument functionality after warm up by switching on all ACAs one-by-one. RCA 18 and RCA 24 still showed the same problems.

Two dedicated tests were then run to further investigate the problem in RCA 28 (saturation after switch on). At warm conditions, however, the anomalous saturation never showed up after several switch-on sequences (see Fig.16).

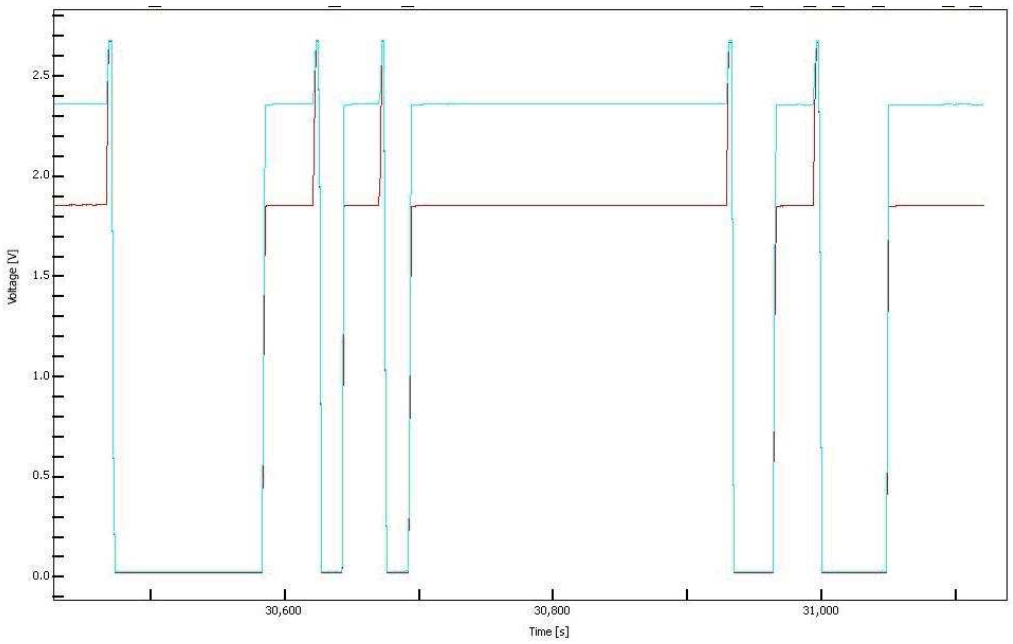

Figure 16: RCA 28 is switched ON-OFF several times using the standard procedure: red and cyan trace represetn $V_{\rm out}$ (R0D0) and $V_{\rm out}$ (R0D1), respectively.

Warm tests after recovery of RCAs 18 and 24. After the cryochamber was opened and the LFI positioned on MGSE electric tests were performed on the connectors wiring the two FEMs which revealed without doubt that the failure on RCA 24 and 18 was indeed in the FEMs level: therefore the RCA 18 radiometer (half FEM) was substituted with the spare unit and the RCA 24 failure was identified and fixed by the JBO team in record-time. At the same time, protective metal shields were mounted on the 70 GHz FEMs in order to protect the bias wires from contact with the HFI during integration: this apparently minor operation determined important anomalies that appeared as FEM failures on RCAs 19, 20 and 21 (dataset AMB_0079).

In detail:

- RCA 19 was not responding to M1-Vg2 changes;
- RCA 20 showed a failure in one phase switch diode (M1 leg);
- RCA 21 showed a failure in one phase switch diode (S1 leg)

LFI was then switched on for 5 minutes to acquire simultaneously data on other radiometers and then switched off to preserve instrument integrity.

Comparison of results between tests XXX_0140 and AMB_0079 is presented in Tab. 6; it must be noticed that the two tests have been performed in very different environmental conditions (BEU temperatures differ by about 20 C, FPU temperatures unknown), voltage comparison was not straight ad required to extrapolate data from test XXX_0140 to AMB_0079 conditions using results from BEU temperature susceptibility tests performed on 30 and 44 GHz RCAs and BEM stand-alone temperature susceptibilty results at 70 GHz.

Table 6: Comparison between test XXX_0140 and AMB_0079; $I_{\rm d}$ and $V_{\rm out}$ are compared. Differences are expressed as percent variation $[Id_{\rm AMB79} - Id_{\rm XXX_1 40}]/Id_{\rm XXX_1 40}$ and $[V_{\rm AMB79} - V_{\rm XXX_1 40}]/V_{\rm XXX_1 40}$. Channel RCA18 (M1-M2) is highlighted since this was the unit refurbished with the spare unit, between the two tests.

		vg1	vg2	VD	I1	I2	Id		V(UNCH)	Vsky	Vref	PH/SW	PH/SW
		DEC	DEC	DEC	DEC	DEC	%		%	%	%	140	79
CH27	M1	250	130	241	205	205	0.16	00	1.36	1.40	2.15	1.00	1.00
	M2	250	130	237	205	205	0.05	01	-0.09	-0.88	-0.05	1.00	1.00
	S1	250	130	255	205	205	0.24	10	-16.24	-16.18	-16.02	1.00	1.00
	S2	250	130	255	205	205	0.20	11	0.50	0.05	0.59	1.01	1.00
CH24	M2	241	241	255	205	205	-1.82	00	-17.56	-18.60	-18.87	0.98	0.99
	M1	241	241	255	205	205	10.41	01	-6.73	-8.08	-7.80	1.01	1.01
	S2	241	241	255	205	205	1.67	10	-17.17	-19.05	-19.05	1.00	1.00
	S1	241	241	255	205	205	1.71	11	2.24	2.24	2.24	1.00	1.00
CH21	S2	217	178	255	255	255	1.37	00	-2.70	-1.07	-0.72	1.02	1.01
	S1	118	163	255	255	255	0.58	01	-5.04	-3.09	-3.77	0.99	0.99
	M1	133	178	255	255	255	0.58	10	-35.64	-38.98	-38.97	1.01	1.01
	M2	151	163	255	255	255	0.81	11	-30.04	-33.59	-33.65	1.00	1.00
CH22	S2	166	172	255	255	255	0.98	00	-5.81	-6.28	-6.91	1.02	1.03
	S1	142	124	255	255	255	0.67	01	-2.31	-3.48	-2.55	0.98	0.97
	M1	154	124	255	255	255	0.88	10	-2.78	-1.85	-3.12	1.01	1.03
	M2	142	121	255	255	255	0.94	11	3.71	2.38	3.80	0.99	0.98
CH23	S2	162	130	255	255	255	0.90	00	1.86	5.85	4.80	0.98	0.99
	S1	148	127	255	255	255	1.48	01	6.08	9.44	10.47	1.01	1.01
	M1	141	133	255	255	255	0.86	10	4.34	-0.12	1.04	0.99	0.98
	M2	183	177	255	255	255	1.23	11	2.88	1.15	0.35	1.01	1.01
CH25	M1	242	242	255	205	205	1.89	00	19.95	20.20	17.29	0.96	0.99
	M2	242	242	255	205	205	1.85	01	29.43	25.56	30.04	1.02	1.00
	S1	242	242	255	205	205	2.08	10	1.08	-0.34	-0.34	1.00	0.99
	S2	242	242	255	205	204	2.09	11	12.21	13.47	12.21	1.00	1.01
CH28	M1	247	128	255	206	205	1.04	00	14.58	14.64	15.42	0.99	1.00
	M2	247	128	255	205	206	0.93	01	-3.63	-5.65	-3.56	1.01	1.00
	S1	246	128	255	205	206	-3.29	10	7.14	7.27	8.08	0.99	0.99
	S2	247	128	255	206	205	0.89	11	14.40	13.55	14.50	1.02	1.01
CH20	S2	151	127	255	255	255	2.77	00	-4.50	-37.50	-2.91	1.01	0.65
	S1	112	172	255	255	255	2.44	01	-3.85	-3.06	-37.37	0.99	1.18
	M1	127	154	255	255	255	2.30	10	8.77	9.35	10.48	1.01	1.01
	M2	145	172	255	255	255	2.44	11	12.24	12.22	12.11	0.99	0.99
CH19	S2	109	114	255	255	255	2.09	00	-52.62	-50.73	-51.42	1.01	1.01
	S1	157	148	255	255	255	2.44	01	-47.56	-44.23	-44.93	0.99	0.99
	M1	172	174	255	255	255	-37.65	10	-11.37	2.30	1.25	1.01	1.02
	M2	115	168	255	255	255	2.30	11	-12.11	0.64	1.80	0.99	0.98
CH18	S2	177	132	255	255	255	1.56	00	50.56	64.10	57.50	0.97	1.01
	S1	135	180	255	255	255	1.46	01	52.89	63.55	69.23	1.03	1.00
	M1	156	147	255	255	255	-6.10	10	4.51	3.53	2.30	0.98	0.99
	M2	165	129	255	255	255	0.96	11	7.07	5.26	5.32	1.01	1.01
CH26	M2	241	242	255	205	205	2.11	00	-6.52	-6.52	-7.41	0.98	1.00
	M1	242	241	255	205	205	1.87	01	18.71	14.98	17.50	1.02	1.01
	S2	241	241	255	205	205	2.12	10	7.84	9.14	8.64	0.98	0.99
	S1	241	241	255	205	205	2.04	11	17.39	16.20	17.39	1.01	1.00

The data in the above table can be analysed according to three criteria.
Comparison of drain currents.

- $I_{\rm d}$ of RCA24-M1 increased by 10%, meaning that Vg1 RCA 24 recovery was positive.

- $I_{\rm d}$ dropped down by about 37% on RCA 19-M1, indicating a problem in this channel.

Comparison of voltage outputs.

- Channels RCA 27 and 28: also after voltage correction, $V_{\rm out}$ are quite different, probably since during test XXX_0140 they suffered saturation due to BEU temperature.

- Channel RCA 21: although drain currents are comparable on M1 and M2, $V_{\rm out}$ dropped down (-35%) on R0D0 and R0D1, indicating a problem in one phase switch.

- Channel RCA 20: drain currents are comparable on S1 and S2 while $V_{\rm out}$ dropped down (-37%) on R1D0 and R1D1, indicating a problem in one phase switch;

- Channel RCA 19: $V_{\rm out}$ is reduced by 50% on R0D0, R0D1 which is in agreement with the observed drop in $I_{\rm d}$.

Symmetry check.

- RCA 20: problem in phase switch (ratio 0.65) not present in test XXX_0140.

Further investigation revealed that the failure was caused by bias wires that were damaged by cutting edges in the metal protecting plates. After mechanically reworking these plates and repairing the wires the instrument functionality was completely recovered (see tests in datasets AMB_0083-84-85-86).

Anomalies in RCA23. Two anomalous behaviours were found on RCA23 at this stage:

1. Burst noise (a.k.a. pop-corn noise) affecting output R1D1; was observed for the first time in test AMB_0079 (i.e after the LFI removal from cryo chamber);

2. Drain current abrupt drops, affecting S1: although they have been discovered for the first time during test AMB_0090, they have been found "a posteriori" in previous tests at least twice (XXX_0028 and AMB_0052).

Burst noise. An example of this effect is represented in Fig.17: it is a random period drop of the voltage with typical amplitude of about 2 mV peak to peak. This feature seems to affect only the output associated to BEM diode in position 1,1; nothing similar is observed on the other outputs.

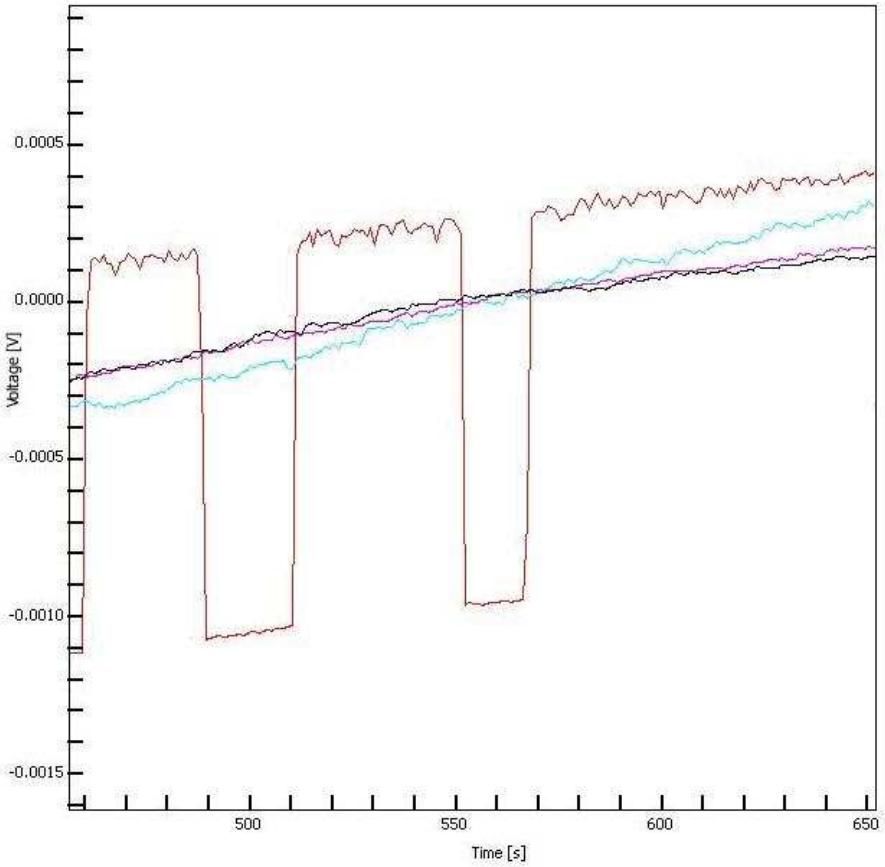

Figure 17: burst noise effect on RCA23 R1D1 (red trace): here the FEM was is switched OFF. The mean voltage value has been removed from the data before plotting.

Data in the above figure indicate that this effect originates in the BEM and is independent of the FEM input level. Being basically a common mode effect is very effectively removed in the differential data as it is shown in Figs.18 and 19.

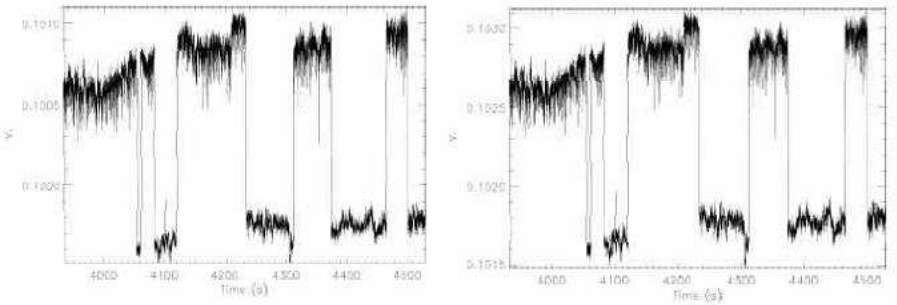

Figure 18: Burst noise affecting sky and ref signals.

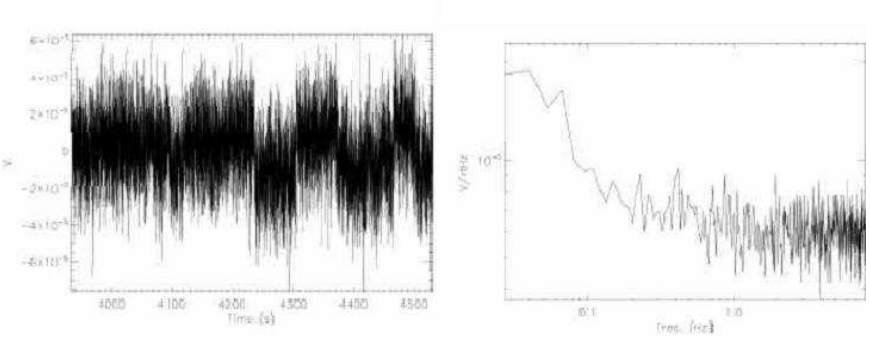

Figure 19: Burst noise is mostly removed when data are differentiated. FFT spectrum on the right.

Current drops. Current drops have been observed for the first time during test AMB_0090. It manifests in two ways (see Fig. 20): current in channel S1 drops down abruptly by about 2mA while BEM voltage output increases in diodes R1D0 and R1D1.

In test AMB_0090 the drop seems to occur in coincidence with a phase switch status change: B/D switching, phase switch polarization changed from 0 to 1 in A/C. In particular, current did never rise back to the previous value but stabilised on an intermediate level. This effect was observed only on channel S1, at least at this macroscopic level.

A very similar effect was also observed in warm tests before the cryogenic campaign, in particular in test AMB_0052 and AMB_0028. No drops were ever observed during cryogenic tests.

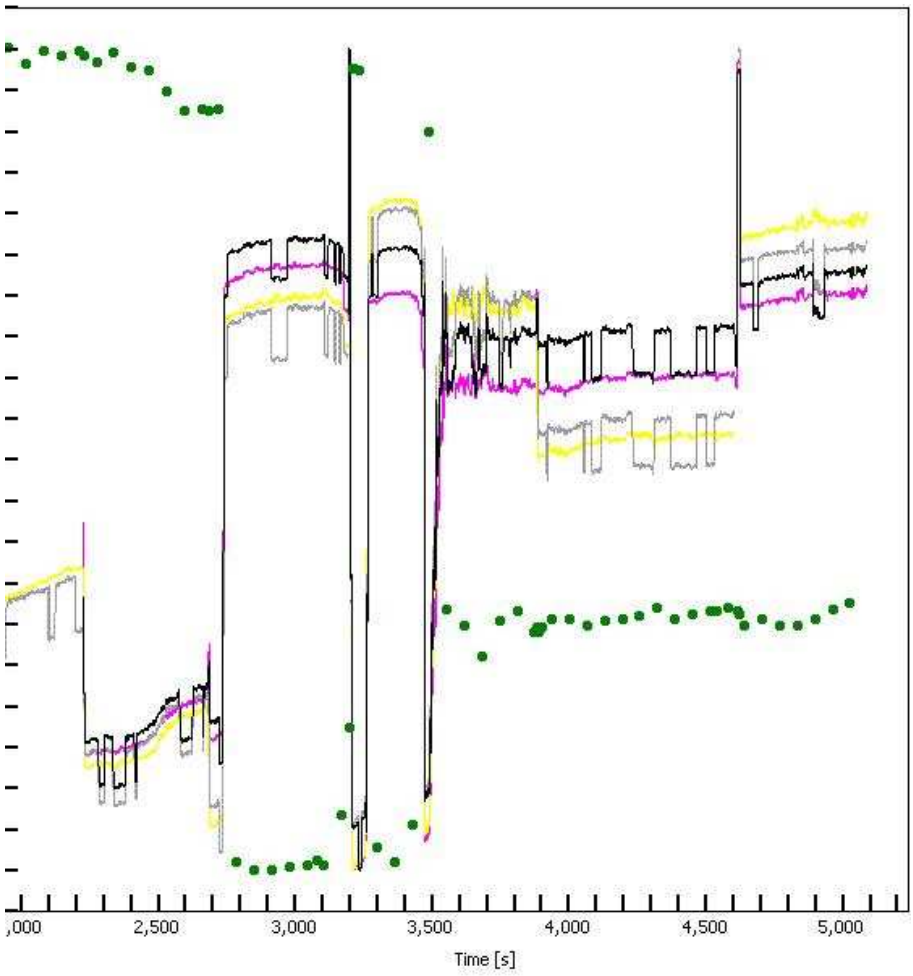

Figure 20: RCA 23 current drop: current (id-S1) is shown with green dots. R1D0 and R1D1 BEM out voltages are shown in black, grey, magenta, yellow (4KHz is ON); burst noise is also evident.

4.4.4 Final warm tests (before shipment)

AMB_01 and AMB_02 were repeated before delivery in a condition in which most of the problems had been definitively fixed. The scenario befor these last tests can be summarised as follows:

- RCA 18: half-FEM (M-arm) substituted
- RCA 19, 20, 21: broken wires repaired, metal shields mechanically worked and replaced.
- RCA 23 burst noise on R1D1: investigated, still present, not affecting differentiated data.
- RCA 23 drain current drops on S1: investigated, appearing only a few times and only at warm.

- RCA 24 Vg1(M1): repaired, properly working.
- RCA 28 switch on saturation: not present at warm and with customized switch on procedure at cold.
- RCA 28 tag inversion sky-ref: still open, to be investigated.

AMB_01 and AMB_02 were performed with the LFI on MGSE. They correspond respectively to datasets AMB_0100 and AMB_0101. Data and results are collected in Tables 7, 8 (AMB_01) and 9 (AMB_02).

Table 7: AMB_01 (dataset AMB_0100) ACAs ON.

RCA #	Detector ID		SCOS Parameter	VG1 DEC	VG2 DEC	VD DEC	I1 DEC	I2 DEC	SCOS Parameter	Expected Id (mA)	ACA ON	i-0 SKY Volt	i-0 REF Volt	i-0 PH/SW	i-1 SKY Volt	i-1 REF Volt	i-1 PH/SW	BEM ON
CH27	00	00	LP001320	234	114	180	205	205	LM051322	19.23	M1	1.760	1.780	1.00	1.980	1.960	1.00	00 0.03
	01	01	LP002320	234	114	180	205	205	LM052322	18.93	M2	2.160	2.180		2.150	2.130		01 0.04
	02	10	LP003320	234	115	200	205	205	LM053322	21.14	S1	2.510	2.560	0.99	2.140	2.100	1.01	10 0.04
	03	11	LP004320	234	114	200	205	205	LM054322	20.68	S2	2.340	2.360		1.940	1.930		11 0.03
CH24	04	00	LP005320	229	229	255	205	205	LM055322	34.99	M1	0.027	0.028	0.99	0.025	0.024	1.01	00 0.01
	05	01	LP006320	229	229	255	205	205	LM056322	34.42	M2	0.017	0.017		0.018	0.017		01 0.01
	06	10	LP007320	230	230	255	205	205	LM057322	36.41	S1	0.006	0.006	1.01	0.008	0.008	0.98	10 0.01
	07	11	LP008320	230	230	255	205	205	LM058322	35.9	S2	0.008	0.008		0.010	0.010		11 0.01
CH21	08	00	LP009320	173	134	255	255	255	LM059322	24.29	S2	0.295	0.292	1.00	0.267	0.268	1.01	00 0.01
	09	01	LP010320	122	119	255	255	255	LM060322	24.28	S1	0.186	0.181		0.162	0.166		01 0.01
	0A	10	LP011320	156	135	255	255	255	LM061322	24.35	M1	0.111	0.106	1.00	0.104	0.109	0.99	10 0.01
	0B	11	LP012320	153	120	255	255	255	LM062322	25.21	M2	0.069	0.065		0.079	0.083		11 0.02
CH22	0C	00	LP013320	120	126	255	255	255	LM063322	23.87	S2	0.340	0.320	1.01	0.404	0.428	0.98	00 0.02
	0D	01	LP014320	96	78	255	255	255	LM064322	23.55	S1	0.294	0.282		0.342	0.354		01 0.01
	0E	10	LP015320	108	78	255	255	255	LM065322	23.23	M1	0.312	0.299	1.01	0.369	0.387	0.99	10 0.01
	0F	11	LP016320	96	76	255	255	255	LM066322	23.35	M2	0.287	0.278		0.333	0.345		11 0.02
CH23	10	00	LP017320	114	81	255	255	255	LM067322	22.89	S2	1.137	1.184	0.99	0.597	0.574	1.00	00 0.04
	11	01	LP018320	99	78	255	255	255	LM068322	24.53	S1	0.974	1.007		0.535	0.517		01 0.05
	12	10	LP019320	94	84	255	255	255	LM069322	23.45	M1	0.530	0.547	1.01	0.666	0.643	0.99	10 0.06
	13	11	LP020320	135	130	255	255	255	LM070322	23.52	M2	0.838	0.872		1.171	1.125		11 0.03
CH25	14	00	LP021320	229	228	255	205	205	LM071322	32.53	M1	0.118	0.123	1.02	0.127	0.123	0.97	00 0.01
	15	01	LP022320	228	228	255	205	205	LM072322	32.10	M2	0.173	0.184		0.179	0.167		01 0.01
	16	10	LP023320	229	229	255	205	205	LM073322	33.57	S1	0.043	0.045	0.99	0.039	0.037	1.00	10 0.01
	17	11	LP024320	230	229	255	205	205	LM074322	34.04	S2	0.040	0.042		0.042	0.041		11 0.01
CH28	18	00	LP025320	234	114	200	206	205	LM075322	22.39	M1	1.590	1.610	1.01	2.160	2.136	0.99	00 0.03
	19	01	LP026320	234	115	240	205	206	LM076322	25.09	M2	2.120	2.170		2.560	2.500		01 0.03
	1A	10	LP027320	233	115	200	205	206	LM077322	22.34	S1	1.560	1.590	1.00	1.420	1.400	1.00	10 0.03
	1B	11	LP028320	234	115	200	206	205	LM078322	21.80	S2	1.706	1.730		1.510	1.490		11 0.03
CH20	1C	00	LP029320	112	88	255	255	255	LM079322	23.84	S2	0.432	0.426	1.00	0.464	0.472	1.00	00 0.02
	1D	01	LP030320	72	132	255	255	255	LM080322	23.6	S1	0.376	0.370		0.398	0.406		01 0.02
	1E	10	LP031320	87	114	255	255	255	LM081322	23.38	M1	0.318	0.310	0.99	0.296	0.303	1.01	10 0.02
	1F	11	LP032320	105	132	255	255	255	LM082322	23.6	M2	0.352	0.339		0.319	0.332		11 0.02
CH19	20	00	LP033320	69	75	255	255	255	LM083322	23.34	S2	0.260	0.258	0.99	0.241	0.240	1.01	00 0.01
	21	01	LP034320	117	108	255	255	255	LM084322	23.66	S1	0.360	0.350		0.363	0.369		01 0.02
	22	10	LP035320	132	136	255	255	255	LM085322	23.72	M1	0.293	0.283	1.01	0.303	0.313	0.99	10 0.01
	23	11	LP036320	75	129	255	255	255	LM086322	23.82	M2	0.206	0.201		0.213	0.218		11 0.02
CH18	24	00	LP037320	130	84	255	255	255	LM087322	23.22	S2	0.474	0.493	1.00	0.488	0.469	1.00	00 0.03
	25	01	LP038320	87	132	255	255	255	LM088322	23.08	S1	0.368	0.377		0.397	0.378		01 0.04
	26	10	LP039320	108	99	255	255	255	LM089322	21.88	M1	0.437	0.422	1.00	0.559	0.578	1.00	10 0.03
	27	11	LP040320	118	132	255	255	255	LM090322	23.08	M2	0.670	0.650		0.948	0.973		11 0.04
CH26	28	00	LP041320	229	228	255	205	205	LM091322	32.73	M1	0.077	0.081	0.98	0.096	0.090	1.03	00 0.01
	29	01	LP042320	229	228	255	205	205	LM092322	32.28	M2	0.043	0.044		0.057	0.056		01 0.01
	2A	10	LP043320	229	228	255	205	205	LM093322	32.57	S1	0.098	0.102	0.99	0.119	0.114	1.01	10 0.01
	2B	11	LP044320	229	228	255	205	205	LM094322	32.32	S2	0.070	0.073		0.078	0.074		11 0.01

Table 8: AMB_01 (dataset AMB_0100) RCA on.

RCA #	Detector ID		SCOS Parameter	VG1 DEC	VG2 DEC	VD DEC	I1 DEC	I2 DEC	SCOS Parameter	Expected Id (mA)	RCA ON	B/D SW SKY Volt	B/D SW REF Volt	PH/SW
CH27	00	00	LP001320	247	127	170	205	205	LM051322	17.77	00	1.730	1.750	1.005
	01	01	LP002320	247	127	180	205	205	LM052322	18.6	01	2.060	2.100	
	02	10	LP003320	247	128	180	205	205	LM053322	19.31	10	2.290	2.320	1.002
	03	11	LP004320	247	128	180	205	205	LM054322	18.37	11	2.190	2.230	
CH24	04	00	LP005320	241	241	255	205	205	LM055322	34.19	00	0.007	0.007	0.986
	05	01	LP006320	241	241	255	205	205	LM056322	33.64	01	0.008	0.008	
	06	10	LP007320	241	241	255	205	205	LM057322	34.71	10	0.005	0.005	0.999
	07	11	LP008320	241	241	255	205	205	LM058322	34.33	11	0.007	0.007	
CH21	08	00	LP009320	217	178	255	255	255	LM059322	24.27	00	0.067	0.067	0.997
	09	01	LP010320	218	163	255	255	255	LM060322	24.15	01	0.066	0.067	
	0A	10	LP011320	133	178	255	255	255	LM061322	24.16	10	0.113	0.113	1.010
	0B	11	LP012320	151	163	255	255	255	LM062322	25.06	11	0.115	0.117	
CH22	0C	00	LP013320	166	172	255	255	255	LM063322	25.08	00	0.291	0.299	0.974
	0D	01	LP014320	142	124	255	255	255	LM064322	25.04	01	0.132	0.129	
	0E	10	LP015320	154	124	255	255	255	LM065322	24.23	10	0.150	0.155	0.986
	0F	11	LP016320	142	121	255	255	255	LM066322	24.16	11	0.273	0.271	
CH23	10	00	LP017320	162	130	255	255	255	LM067322	23.03	00	0.455	0.468	0.982
	11	01	LP018320	148	127	255	255	255	LM068322	24.69	01	0.527	0.523	
	12	10	LP019320	141	133	255	255	255	LM069322	23.19	10	0.591	0.600	0.989
	13	11	LP020320	183	177	255	255	255	LM070322	24.04	11	0.300	0.300	
CH25	14	00	LP021320	242	242	255	205	205	LM071322	30.4	00	0.038	0.040	1.023
	15	01	LP022320	242	242	255	205	205	LM072322	29.88	01	0.033	0.037	
	16	10	LP023320	242	242	255	205	205	LM073322	30.74	10	0.010	0.010	0.989
	17	11	LP024320	242	242	255	205	205	LM074322	31.08	11	0.008	0.008	
CH28	18	00	LP025320	248	128	200	206	205	LM075322	21.43	00	1.440	1.470	0.982
	19	01	LP026320	248	128	200	205	206	LM076322	21.56	01	1.880	1.850	
	1A	10	LP027320	247	129	200	205	206	LM077322	20.99	10	1.680	1.690	0.994
	1B	11	LP028320	247	129	200	206	205	LM078322	20.84	11	1.510	1.500	
CH20	1C	00	LP029320	151	127	255	255	255	LM079322	24.47	00	0.362	0.359	1.017
	1D	01	LP030320	112	172	255	255	255	LM080322	24.56	01	0.343	0.352	
	1E	10	LP031320	127	154	255	255	255	LM081322	24.23	10	0.437	0.443	0.993
	1F	11	LP032320	145	172	255	255	255	LM082322	24.8	11	0.429	0.429	
CH19	20	00	LP033320	109	114	255	255	255	LM083322	23.49	00	0.364	0.371	0.988
	21	01	LP034320	157	148	255	255	255	LM084322	24.62	01	0.368	0.366	
	22	10	LP035320	172	174	255	255	255	LM085322	24.93	10	0.292	0.297	0.987
	23	11	LP036320	115	168	255	255	255	LM086322	24.86	11	0.283	0.281	
CH18	24	00	LP037320	177	132	255	255	255	LM087322	23.6	00	0.254	0.251	1.020
	25	01	LP038320	135	180	255	255	255	LM088322	23.6	01	0.249	0.256	
	26	10	LP039320	156	147	255	255	255	LM089322	22.28	10	0.673	0.683	0.987
	27	11	LP040320	165	129	255	255	255	LM090322	23.32	11	0.486	0.481	
CH26	28	00	LP041320	241	242	255	205	205	LM091322	30.34	00	0.014	0.015	0.973
	29	01	LP042320	242	241	255	205	205	LM092322	29.99	01	0.018	0.018	
	2A	10	LP043320	241	241	255	205	205	LM093322	30.13	10	0.024	0.024	0.975
	2B	11	LP044320	241	241	255	205	205	LM094322	29.8	11	0.027	0.026	

Table 9: AMB_02 (dataset AMB_0101) LFI ON; both A/C and B/D 4KHz states are represented.

RCA #	Detector ID		SCOS Parameter	VG1 DEC	VG2 DEC	VD DEC	I1 DEC	I2 DEC	SCOS Parameter	Expected Id (mA)	LFI ON	A/C SW SKY Volt	A/C SW REF Volt	PH/SW	B/D SW SKY Volt	B/D SW REF Volt	PH/SW
CH27	00	00	LP001320	250	130	200	205	205	LM051322	15.42	00	1.154	1.169	1.001	1.160	1.177	0.999
	01	01	LP002320	250	130	200	205	205	LM052322	15.11	01	1.215	1.232		1.224	1.238	
	02	10	LP003320	250	130	200	205	205	LM053322	15.62	10	1.078	1.103	0.991	1.084	1.103	0.996
	03	11	LP004320	250	130	200	205	205	LM054322	15.17	11	0.905	0.911		0.904	0.916	
CH24	04	00	LP005320	241	241	255	205	205	LM055322	28.82	00	0.007	0.007	0.987	0.007	0.007	0.993
	05	01	LP006320	241	241	255	205	205	LM056322	28.5	01	0.008	0.008		0.008	0.008	
	06	10	LP007320	241	241	255	205	205	LM057322	29.37	10	0.005	0.005	1.000	0.005	0.005	1.000
	07	11	LP008320	241	241	255	205	205	LM058322	29.34	11	0.007	0.007		0.007	0.007	
CH21	08	00	LP009320	217	178	255	255	255	LM059322	20.23	00	0.030	0.030	1.010	0.030	0.029	1.016
	09	01	LP010320	218	163	255	255	255	LM060322	17.72	01	0.028	0.028		0.027	0.028	
	0A	10	LP011320	133	178	255	255	255	LM061322	17.79	10	0.058	0.057	1.024	0.059	0.058	1.007
	0B	11	LP012320	151	163	255	255	255	LM062322	19.27	11	0.055	0.057		0.056	0.057	
CH22	0C	00	LP013320	166	172	255	255	255	LM063322	18.99	00	0.075	0.074	1.025	0.076	0.075	1.018
	0D	01	LP014320	142	124	255	255	255	LM064322	18.59	01	0.086	0.089		0.087	0.089	
	0E	10	LP015320	154	124	255	255	255	LM065322	18.68	10	0.069	0.068	1.025	0.069	0.068	1.010
	0F	11	LP016320	142	121	255	255	255	LM066322	18.6	11	0.083	0.085		0.084	0.085	
CH23	10	00	LP017320	162	130	255	255	255	LM067322	17.95	00	0.134	0.136	0.992	0.130	0.137	0.968
	11	01	LP018320	148	127	255	255	255	LM068322	19.15	01	0.164	0.163		0.159	0.157	
	12	10	LP019320	141	133	255	255	255	LM069322	17.70	10	0.173	0.177	0.981	0.180	0.183	0.989
	13	11	LP020320	183	177	255	255	255	LM070322	18.15	11	0.087	0.086		0.090	0.090	
CH25	14	00	LP021320	242	242	255	205	205	LM071322	26.8	00	0.035	0.036	0.986	0.035	0.037	0.959
	15	01	LP022320	242	242	255	205	205	LM072322	26.28	01	0.034	0.035		0.036	0.035	
	16	10	LP023320	242	242	255	205	205	LM073322	27.31	10	0.010	0.010	0.999	0.010	0.010	0.994
	17	11	LP024320	242	242	255	205	205	LM074322	27.7	11	0.008	0.008		0.008	0.008	
CH28	18	00	LP025320	247	128	200	206	205	LM075322	17.08	00	0.574	0.577	0.998	0.580	0.589	0.985
	19	01	LP026320	247	128	200	205	206	LM076322	16.79	01	0.755	0.755		0.771	0.759	
	1A	10	LP027320	246	128	200	205	206	LM077322	16.94	10	0.722	0.731	0.993	0.734	0.735	0.997
	1B	11	LP028320	247	128	200	206	205	LM078322	16.59	11	0.645	0.644		0.652	0.649	
CH20	1C	00	LP029320	151	127	255	255	255	LM079322	19.75	00	0.115	0.115	1.011	0.116	0.115	1.016
	1D	01	LP030320	112	172	255	255	255	LM080322	19.79	01	0.108	0.110		0.108	0.110	
	1E	10	LP031320	127	154	255	255	255	LM081322	19.59	10	0.127	0.126	1.008	0.127	0.127	1.007
	1F	11	LP032320	145	172	255	255	255	LM082322	19.87	11	0.134	0.135		0.134	0.136	
CH19	20	00	LP033320	109	114	255	255	255	LM083322	19	00	0.084	0.083	1.019	0.085	0.085	1.011
	21	01	LP034320	157	148	255	255	255	LM084322	19.79	01	0.090	0.092		0.091	0.093	
	22	10	LP035320	172	174	255	255	255	LM085322	19.77	10	0.107	0.107	1.001	0.106	0.105	1.010
	23	11	LP036320	115	168	255	255	255	LM086322	20.03	11	0.104	0.104		0.101	0.102	
CH18	24	00	LP037320	177	132	255	255	255	LM087322	18.2	00	0.129	0.128	1.008	0.127	0.126	1.010
	25	01	LP038320	135	180	255	255	255	LM088322	18.02	01	0.175	0.176		0.171	0.173	
	26	10	LP039320	156	147	255	255	255	LM089322	16.34	10	0.089	0.090	0.986	0.090	0.092	0.985
	27	11	LP040320	165	129	255	255	255	LM090322	17.91	11	0.100	0.099		0.101	0.100	
CH26	28	00	LP041320	241	242	255	205	205	LM091322	27.04	00	0.013	0.013	1.003	0.013	0.013	0.976
	29	01	LP042320	242	241	255	205	205	LM092322	26.55	01	0.016	0.016		0.016	0.016	
	2A	10	LP043320	241	241	255	205	205	LM093322	26.83	10	0.020	0.021	0.993	0.020	0.021	0.979
	2B	11	LP044320	241	241	255	205	205	LM094322	26.42	11	0.022	0.022		0.023	0.023	

4.4.5 Comparison with previous tests

Comparison with *Step 3* tests Data from the AMB_01 repetition (dataset AMB_0100) have been compared with: AMB_0074 and AMB_0083, AMB_0084, AMB_0085 and AMB_0086. Comparison is displayed in Fig. 21

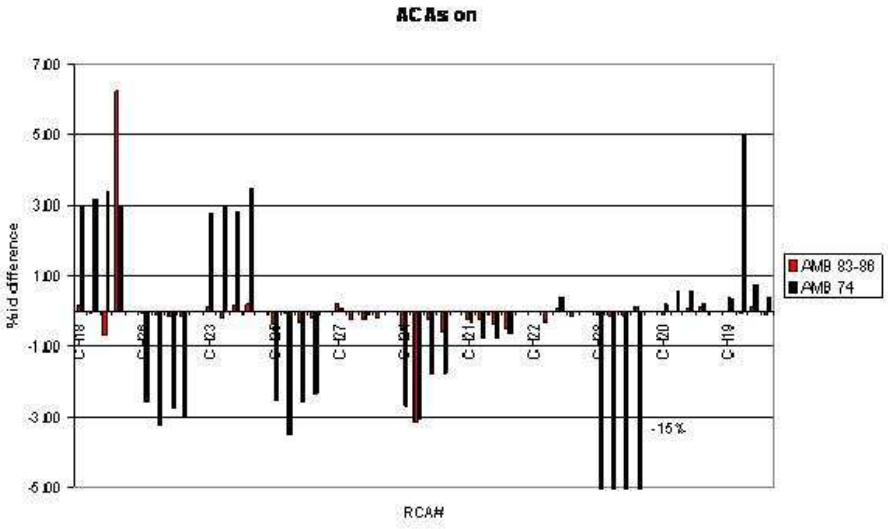

Figure 21: Comparison of different AMB_01 tests. AMB_0074 was performed inside the cryochamber, before fixing RCAs 18 and 24 and with RCA 28 saturating due to high bias applied. AMB_0083-86 have been performed after RCA 18 refurbishment, RCA 19, 20, 24 failure fixing. On Y axis is represented the percentage difference in $V_{\rm out}$ and $I_{\rm d}$.

Data from the AMB_02 repetition have been compared with: XXX_0140 and AMB_0079 (see Fig. 22 for comparison of drain currents and Figs. 23 and 24 for comparison of output voltage in two switching conditions.

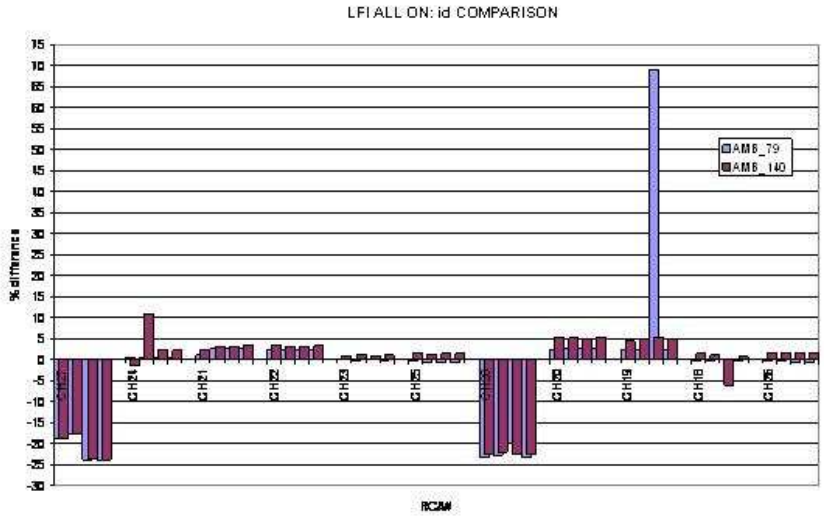

Figure 22: Drain currents from test AMB_0101 are compared with other AMB_02 datasets. (XXX_0140, before fixing RCAs 18 and 24 and AMB_0079 after fixing RCAs 18 and 24). In both these tests RCA 28 and RCA 27 were biased in near saturating conditions; therefore differences in these RCAs are due only to saturation.

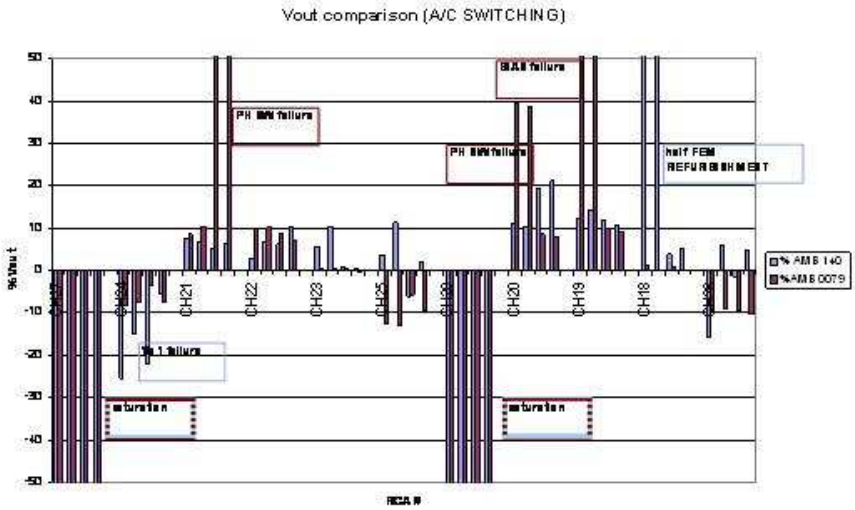

Figure 23: Same as in Fig. 22 for voltage outputs in A/C switching condition

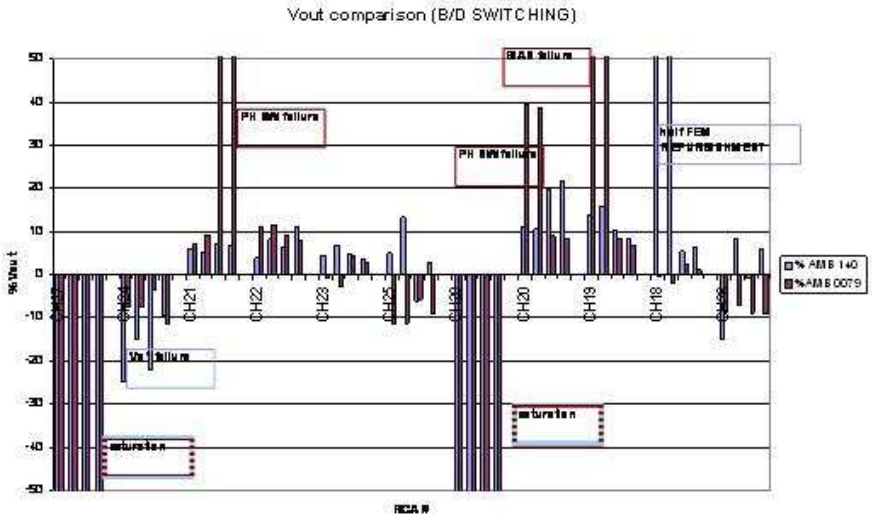

Comparison presented in the following plots indicates that:

Figure 24: Same as in Fig. 22 for voltage outputs in B/D switching condition

- Drain currents are in agreement with tests performed in comparable conditions: differences are due only to problems affecting radiometers in the past tests. This agreement suggests that FEM LNAs are now all working properly.

- Results from phase switches symmetry check indicate that PH/SW are behaving properly both in A/C and B/D 4KHz switching condition.

- In all cases the instrument was working properly scientific outputs are in agreement within 10% with old tests, whereas a disagreement is present in problemaric cases (e.g. saturation or failures); comparison shows in a deterministic way disagreement and agreement where a problem was present or removed.

Comparison with *Step 1* tests Data from AMB_01 (AMB_0100 dataset) have been compared with: AMB_0016 (see Table 10 and Fig. 25).

Table 10: Comparison between AMB_0100 and AMB_0016; yellow line refers to the RCA 18 refurbishment. Differences are in terms of percentage discrepancy in $I_{\rm d}$ and $V_{\rm out}$

RCA #	Detector ID		VG1 DEC	VG2 DEC	VD DEC	I1 DEC	I2 DEC	SCOS Parameter	Id	LFI ON	ACA ON	i-0 SKY	i-0 REF	i-1 SKY	i-1 REF	i-0 SKY•REF	i-1 SKY•REF	<UNCH>		BEM ON
									%			%	%	%	%	%	%	%		%
CH27	00	00	0	0	-54	0	0	LM051322	-10.1	00	M1	-18.52	-16.82	-16.10	-17.99	-17.67	-17.05	-17.67	00	2.8939
	01	01	0	0	-52	0	0	LM052322	-10.3	01	M2	-15.95	-14.17	-13.65	-15.48	-15.07	-14.57	-14.57	01	4.3956
	02	10	0	0	-38	0	0	LM053322	-3.4	10	S1	9.56	14.29	14.44	10.53	11.90	12.47	11.90	10	3.5422
	03	11	0	0	-33	0	0	LM054322	-3.3	11	S2	8.84	10.80	10.86	9.66	9.81	10.26	10.26	11	4.1009
CH24	04	00	0	0	0	0	0	LM055322	9.5	00	M1	30.24	20.87	20.00	17.65	25.29	18.84	25.29	00	6.0000
	05	01	0	0	0	0	0	LM056322	5.4	01	M2	39.50	26.09	48.33	34.92	32.30	41.46	41.46	01	6.5574
	06	10	0	0	0	0	0	LM057322	7.9	10	S1	10.91	14.81	13.70	10.81	12.84	12.24	12.84	10	8.3333
	07	11	0	0	0	0	0	LM058322	5.9	11	S2	20.00	25.00	25.30	17.65	22.48	21.43	21.43	11	7.5758
CH21	08	00	0	0	0	0	0	LM059322	0.5	00	S2	12.17	13.62	13.14	11.67	12.88	12.39	12.39	00	-9.6386
	09	01	0	0	0	0	0	LM060322	0.7	01	S1	4.49	4.62	1.89	1.84	4.56	1.86	4.56	01	-12.9870
	0A	10	0	0	0	0	0	LM061322	0.5	10	M1	13.50	13.98	8.56	8.04	13.73	8.30	13.73	10	-9.9338
	0B	11	0	0	0	0	0	LM062322	4.0	11	M2	24.51	24.71	18.03	17.90	24.61	17.96	17.96	11	-9.5238
CH22	0C	00	0	0	0	0	0	LM063322	5.2	00	S2	3.66	5.26	4.66	3.13	4.43	3.87	3.87	00	-8.2873
	0D	01	0	0	0	0	0	LM064322	2.1	01	S1	0.34	1.08	0.80	0.00	0.70	0.39	0.70	01	-6.9620
	0E	10	0	0	0	0	0	LM065322	2.3	10	M1	2.63	4.55	4.50	2.82	3.56	3.64	3.56	10	-8.5271
	0F	11	0	0	0	0	0	LM066322	1.8	11	M2	0.92	1.31	2.46	1.77	1.11	2.11	2.11	11	-9.6386
CH23	10	00	0	0	0	0	0	LM067322	-3.4	00	S2	5.96	7.31	7.36	5.92	6.64	6.65	6.65	00	-5.4502
	11	01	0	0	0	0	0	LM068322	9.4	01	S1	8.46	9.46	9.45	8.61	8.97	9.04	8.97	01	-3.7344
	12	10	0	0	0	0	0	LM069322	5.3	10	M1	7.29	10.44	15.42	12.57	8.87	14.01	8.87	10	-5.9011
	13	11	0	0	0	0	0	LM070322	4.5	11	M2	7.44	7.87	11.00	10.40	7.66	10.70	10.70	11	-2.0270
CH25	14	00	0	0	0	0	0	LM071322	8.4	00	M1	26.88	38.20	35.11	25.51	32.42	30.21	32.42	00	5.9701
	15	01	0	0	0	0	0	LM072322	9.3	01	M2	21.83	38.20	38.76	20.14	29.75	29.10	29.10	01	10.9375
	16	10	0	0	0	0	0	LM073322	8.4	10	S1	35.33	51.00	55.60	41.54	42.95	48.43	42.95	10	3.2258
	17	11	0	0	0	0	0	LM074322	8.3	11	S2	42.86	54.81	63.08	50.37	48.73	56.60	56.60	11	10.6383
CH28	18	00	0	0	-43	0	0	LM075322	9.2	00	M1	6.71	9.52	10.20	7.88	8.11	9.04	8.11	00	4.0000
	19	01	0	0	0	0	0	LM076322	10.1	01	M2	8.16	13.61	14.29	9.65	10.85	11.95	11.95	01	-16.3987
	1A	10	0	0	-41	0	0	LM077322	-4.5	10	S1	-35.80	-33.47	-33.33	-35.19	-34.65	-34.27	-34.65	10	2.6616
	1B	11	0	0	-44	0	0	LM078322	-5.5	11	S2	-33.88	-32.16	-32.89	-34.36	-33.02	-33.63	-33.63	11	2.9851
CH20	1C	00	0	0	0	0	0	LM079322	1.7	00	S2	9.92	12.11	10.45	8.01	11.00	9.21	9.21	00	-9.0909
	1D	01	0	0	0	0	0	LM080322	1.8	01	S1	1.90	2.49	2.58	2.27	2.19	2.42	2.19	01	-10.7981
	1E	10	0	0	0	0	0	LM081322	2.2	10	M1	2.91	4.03	1.72	0.33	3.46	1.01	3.46	10	-8.6758
	1F	11	0	0	0	0	0	LM082322	1.9	11	M2	2.33	2.42	0.63	0.61	2.37	0.62	0.62	11	-7.4257
CH19	20	00	0	0	0	0	0	LM083322	3.3	00	S2	-10.76	-8.94	-7.03	-8.98	-9.86	-8.01	-8.01	00	-11.7647
	21	01	0	0	0	0	0	LM084322	2.6	01	S1	-0.83	-0.57	0.28	-0.27	-0.70	0.00	-0.70	01	-13.2420
	22	10	0	0	0	0	0	LM085322	3.2	10	M1	0.34	2.17	3.41	1.95	1.23	2.67	1.23	10	-8.0745
	23	11	0	0	0	0	0	LM086322	3.6	11	M2	0.00	1.01	1.91	1.40	0.49	1.65	1.65	11	-8.5714
CH18	24	00	0	0	0	0	0	LM087322	3.3	00	S2	2.38	3.79	7.73	6.35	3.09	7.05	7.05	00	-10.9792
	25	01	0	0	0	0	0	LM088322	3.6	01	S1	3.77	5.01	5.87	5.00	4.40	5.44	4.40	01	-9.7561
	26	10	0	0	0	0	0	LM089322	-0.6	10	M1	-23.92	-26.35	-27.12	-24.94	-25.14	-26.02	-25.14	10	-9.0909
	27	11	0	0	0	0	0	LM090322	2.3	11	M2	7.54	1.40	5.69	11.71	4.43	8.65	8.65	11	-7.3634
CH26	28	00	0	0	0	0	0	LM091322	10.9	00	M1	30.29	45.16	50.79	33.68	37.51	41.97	37.51	00	3.7037
	29	01	0	0	0	0	0	LM092322	6.6	01	M2	34.70	41.42	44.95	37.35	38.02	41.10	41.10	01	9.2308
	2A	10	0	0	0	0	0	LM093322	9.5	10	S1	29.12	40.66	45.22	32.87	34.77	38.90	34.77	10	4.8632
	2B	11	0	0	0	0	0	LM094322	7.4	11	S2	32.51	45.71	50.58	36.33	38.95	43.27	43.27	11	5.9701

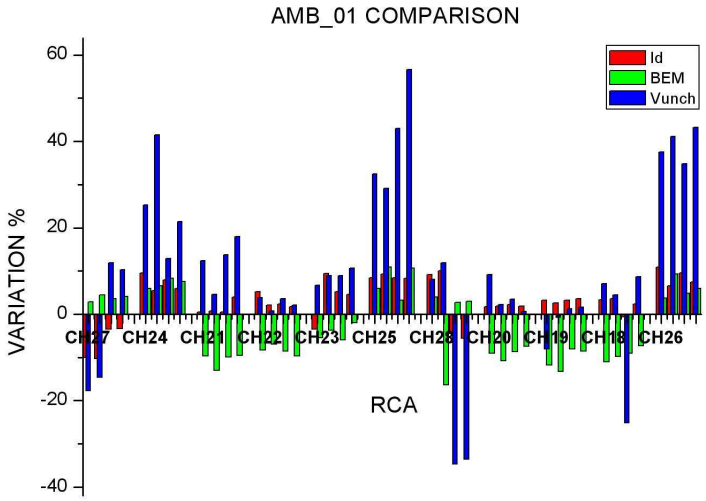

Figure 25: Same as in previous table in graphical form.

Data from AMB_02 (AMB_0101 dataset) have been compared with: AMB_0052 (see Table 11 and Fig. 26).

Table 11: Comparison between AMB_0101 and AMB_0052

RCA #	Detector ID			SCOS Parameter	VG1 DEC	VG2 DEC	VD DEC	I1 DEC	I2 DEC	SCOS Parameter	Expected Id (mA)	LFI ON	A/C SW SKY	A/C SW REF
CH27	00	00	M1	LP001320	0	0	-55	-56	-56	LM051322	-16.8	00	-25.5	-25.4
	01	01	M2	LP002320	0	0	-55	-56	-56	LM052322	-17.4	01	-24.3	-21.7
	02	10	S1	LP003320	0	0	-55	-56	-56	LM053322	-16.7	10	-12.9	-11.6
	03	11	S2	LP004320	0	0	-55	-56	-56	LM054322	-17.8	11	-8.3	-6.6
CH24	04	00	M2	LP005320	0	0	0	0	0	LM055322	14.1	00	-11.3	-8.8
	05	01	M1	LP006320	0	0	0	0	0	LM056322	23.1	01	-7.0	-7.0
	06	10	S2	LP007320	0	0	0	0	0	LM057322	14.2	10	8.0	8.0
	07	11	S1	LP008320	0	0	0	0	0	LM058322	14.1	11	7.4	5.8
CH21	08	00	S2	LP009320	0	0	0	0	0	LM059322	13.7	00	15.8	15.0
	09	01	S1	LP010320	0	0	0	0	0	LM060322	12.9	01	16.4	16.5
	0A	10	M1	LP011320	0	0	0	0	0	LM061322	13.4	10	15.9	15.8
	0B	11	M2	LP012320	0	0	0	0	0	LM062322	14.4	11	12.5	16.9
CH22	0C	00	S2	LP013320	0	0	0	0	0	LM063322	13.7	00	19.7	22.0
	0D	01	S1	LP014320	0	0	0	0	0	LM064322	13.6	01	23.9	24.6
	0E	10	M1	LP015320	0	0	0	0	0	LM065322	15.1	10	23.9	25.4
	0F	11	M2	LP016320	0	0	0	0	0	LM066322	14.0	11	23.9	23.2
CH23	10	00	S2	LP017320	0	0	0	0	0	LM067322	16.2	00	18.8	19.9
	11	01	S1	LP018320	0	0	0	0	0	LM068322	18.5	01	25.2	25.6
	12	10	M1	LP019320	0	0	0	0	0	LM069322	10.1	10	-6.8	-5.6
	13	11	M2	LP020320	0	0	0	0	0	LM070322	8.6	11	-5.1	-5.2
CH25	14	00	M1	LP021320	0	0	0	0	0	LM071322	12.1	00	34.6	38.8
	15	01	M2	LP022320	0	0	0	0	0	LM072322	12.0	01	37.6	43.8
	16	10	S1	LP023320	0	0	0	0	0	LM073322	12.6	10	22.5	24.1
	17	11	S2	LP024320	0	0	0	0	0	LM074322	13.1	11	42.1	41.9
CH28	18	00	M1	LP025320	0	0	-55	-55	-56	LM075322	-15.3	00	-16.2	-22.3
	19	01	M2	LP026320	0	0	-55	-56	-55	LM076322	-15.1	01	-17.2	-10.4
	1A	10	S1	LP027320	0	0	-55	0	0	LM077322	-15.9	10	-69.1	-68.9
	1B	11	S2	LP028320	0	0	-55	0	0	LM078322	-15.8	11	-69.0	-69.6
CH20	1C	00	S2	LP029320	0	0	0	0	0	LM079322	15.2	00	28.1	28.9
	1D	01	S1	LP030320	0	0	0	0	0	LM080322	15.3	01	25.5	26.1
	1E	10	M1	LP031320	0	0	0	0	0	LM081322	15.6	10	28.0	29.0
	1F	11	M2	LP032320	0	0	0	0	0	LM082322	15.3	11	29.7	29.0
CH19	20	00	S2	LP033320	0	0	0	0	0	LM083322	14.4	00	29.7	29.7
	21	01	S1	LP034320	0	0	0	0	0	LM084322	15.3	01	24.6	23.9
	22	10	M1	LP035320	0	0	0	0	0	LM085322	16.2	10	21.7	23.3
	23	11	M2	LP036320	0	0	0	0	0	LM086322	18.2	11	21.9	21.0
CH18	24	00	S2	LP037320	0	0	0	0	0	LM087322	11.7	00	18.3	16.2
	25	01	S1	LP038320	0	0	0	0	0	LM088322	10.8	01	18.0	19.7
	26	10	M1	LP039320	0	0	0	0	0	LM089322	2.8	10	14.9	15.6
	27	11	M2	LP040320	0	0	0	0	0	LM090322	10.4	11	14.9	13.8
CH26	28	00	M2	LP041320	0	0	0	0	0	LM091322	12.4	00	27.0	29.0
	29	01	M1	LP042320	0	0	0	0	0	LM092322	13.1	01	30.8	33.3
	2A	10	S2	LP043320	0	0	0	0	0	LM093322	13.1	10	29.3	31.2
	2B	11	S1	LP044320	0	0	0	0	0	LM094322	12.3	11	36.6	36.6

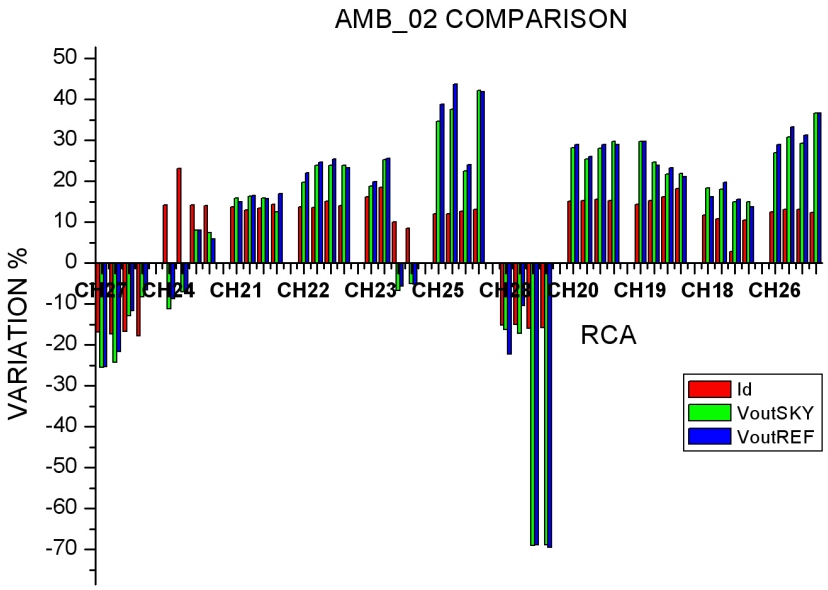

Figure 26: Same as in previous table in graphical form.

The main results of this comparison are:

- Drain currents are generally higher than in the incoming functional tests (probably because of higher FPU temperature). RCA 27 and RCA 28 show lower currents, but this is due to lower V_d applied to avoid DAE saturation. RCA 18 M1 show lower currents, but no comparison can be made for this half-FEM (M1 and M2) since it was changed with the spare unit.
- Agreement with *Step 1* tests seems to be better for test AMB_01, when individual ACAs are switched on separately. Maybe it can be explained with the fact that, when all LFI is on, parameters that can be change increase because of the harness interconnections. In particular, agreement is very good for 70 GHz channels (within 5%) while seems to be more poorer for 30 and 44 GHz channels.

4.5 Conclusions

Functional tests revealed to be extremely important to understanding the LFI behaviour and to investigate failures. Comparison between tests performed at various levels allowed to understand where problems occurred and to make guess about their possible solutions. Unfortunately this comparison has not been always straight, because of the different environmental and setup conditions adopted during the tests. Moreover, sensor monitoring was in some cases insufficient missing at all, which made the analysis much more complicated.

Failure of RCA 24 V_{g1} bias was not identified during the incoming tests (STEP1). Further practice and accuracy gained during the campaign taught us how to focus attention on possible source of non ideal features giving much more confidence on the interpretation of the instrument

output during functional tests. Some failures and non idealities were discovered during cryogenic tests (STEP2: RCA 24, and RCA 18 failure; RCA 28 saturation, RCA 28 sky ref identification) or during the second section of warm functional tests (STEP3: RCA 19, 20, 21 bias wires failure; RCA 23 burst noise and drain current variations).

At the end of the test campaign, after the various failures were fixed, LFI functionality has been demonstrated. A marginal issue remains open on RCA 23 (sudden drain current drops), that we have not been able to reproduce and then fix. The problem, however, showed up only a few times and only during warm tests.

5 Receiver tuning

5.1 Phase switch bias currents

5.1.1 Experimental

Phase switch current balancing has been the first step in receiver tuning after cryogenic functionality tests. The objective is to find, for each phase switch, the optimal currents I_1 and I_2 to the two switch diodes in order maximise the amplitude match.

According to the test procedure (see [AD3]) each radiometer was set in the optimal bias configuration found at RCA level and then bias currents were changed around this point along a line in the $[I_1, I_2]$ plane. During the test the other half of the radiometer was kept in the OFF position (i.e. no biases given to LNA and phase switch).

In Fig. 27 we show, as an example, the radiometric voltage output (LFI25, radiometer R0 in this case) during the tuning of the M1 phase switch currents. We can see how in correspondence of the optimal bias currents to the difference between the odd and even samples is minimised as a result of the optimised phase switch amplitude balance.

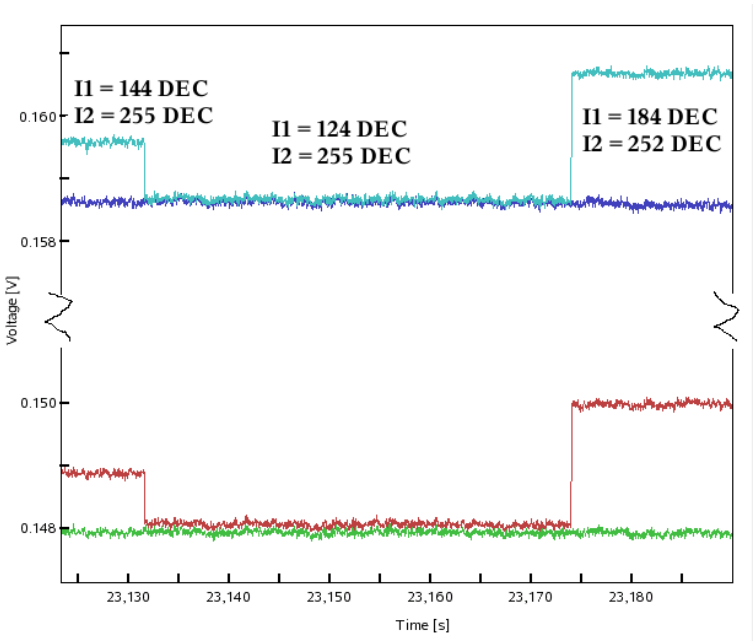

Figure 27: Radiometric voltage output from radiometer R0 (LFI25) during the tuning of M1 phase switch bias currents

In Table 12 we list the tests used for the data analysis.

We remind that this tuning has been performed only for the 30 and 44 GHz chains. In the 70 GHz receivers the phase switch currents have all been set to the maximum value of the DAE range in order to minimise the rise time which was considerably longer than in 30 and 44 GHz receivers.

Table 12: List of tests used in the data analysis for phase switch bias tuning

Feed ID	FEM ch.	Test ID
#24	M1	TUN_0005
	M2	TUN_0005
	S1	TUN_0009
	S2	TUN_0005
#25	M1	TUN_0006
	M2	TUN_0006
	S1	TUN_0006
	S2	TUN_0006
#26	M1	TUN_0007
	M2	TUN_0007
	S1	TUN_0009
	S2	TUN_0007

Feed ID	FEM ch.	Test ID
#27	M1	TUN_0001
	M2	TUN_0001
	S1	TUN_0001
	S2	TUN_0009
#28	M1	TUN_0008
	M2	TUN_0008
	S1	TUN_0008
	S2	TUN_0009

5.1.2 Optimal bias configuration

In the following two tables we summarise the optimal bias configuration coming from RCA and RAA test campaigns.

In the first table we report RAA optimal points in decimal units corresponding to the command given to the DAE to bias the switches, while in the second table we summarise the RCA and RAA bias currents in physical units.

More detailed plots containing the complete sets of data points acquired at RCA and RAA levels is available in Annex 16. The complete details of the data analysis of the tests performed during the RAA test campaign is available in Annex 17

Table 13: Summary of 30 and 44 GHz optimal phase switch currents in terms of decimal codes used to command the DAE. Only RAA values are reported.

Feed ID	FEM ch.	I_1 (DEC)	I_2 (DEC)
#24	M1	152	252
	M2	91	255
	S1	87	234
	S2	96	255
#25	M1	124	255
	M2	89	255
	S1	93	255
	S2	121	255
#26	M1	118	255
	M2	136	255
	S1	159	255
	S2	114	255

Feed ID	FEM ch.	I_1 (DEC)	I_2 (DEC)
#27	M1	148	210
	M2	169	214
	S1	138	192
	S2	148	184
#28	M1	153	180
	M2	101	204
	S1	112	197
	S2	108	200

Table 14: Summary of 30 and 44 GHz optimal phase switch currents in physical units. Measurements both at RCA and RAA levels are reported

		I_1 (mA)			I_2 (mA)		
Feed ID	FEM ch.	RAA	RCA	Δ (%)	RAA	RCA	Δ (%)
#24	M1	0.591	0.593	0.3	0.980	0.897	-9.3
	M2	0.355	0.494	28.1	0.992	0.986	-0.6
	S1	0.340	0.497	31.6	0.911	0.982	7.2
	S2	0.374	0.491	23.8	0.992	0.971	-2.2
#25	M1	0.482	0.718	32.9	0.992	0.982	-1.0
	M2	0.348	0.596	41.6	0.991	0.986	-0.5
	S1	0.363	0.599	39.4	0.992	0.982	-1.0
	S2	0.472	0.597	20.9	0.992	0.971	-2.2
#26	M1	0.460	0.695	33.8	0.992	0.897	-10.6
	M2	0.530	0.596	11.1	0.992	0.986	-0.6
	S1	0.618	0.698	11.5	0.992	0.982	-1.0
	S2	0.444	0.597	25.6	0.991	0.971	-2.1
#27	M1	0.576	0.597	3.5	0.817	0.800	-2.1
	M2	0.658	0.697	5.6	0.832	0.797	-4.4
	S1	0.537	0.591	9.1	0.747	0.699	-6.9
	S2	0.577	0.597	3.4	0.716	0.698	-2.6
#28	M1	0.596	0.597	0.2	0.700	0.702	0.3
	M2	0.394	0.494	20.2	0.794	0.695	-14.2
	S1	0.437	0.497	12.1	0.767	0.707	-8.5
	S2	0.421	0.499	15.6	0.778	0.702	-10.8

5.1.3 Criticalities and recommendations

Tuning phase switch bias currents is a relatively simple task and yields unambiguous results. On the other hand we have observed, for some channels, discrepances from the optimal points found at RCA level up to $\sim 40\%$. This discrepancy was somewhat unexpected and its cause has not been fully understood yet.

We therefore believe that the test procedure must be revised for its use in flight conditions during the CPV phase. In particular we think that the sampling strategy of bias currents must be changed in order to sample bias values in a reasonably wide square matrix in the $[I_1, I_2]$ plane.

R.1: ***phase switch tuning procedure for CPV phase should foresee sampling bias currents in a square matrix around the optimal point found during RAA testing.***

5.2 Drain voltage

5.2.1 Experimental

Drain currents have been set on the basis of the values used at RCA level and that resulted from tuning activity performed at FEM level. In particular the RCA values have been modified following a procedure (discussed in [AD3] which takes into account the cryoharness resistance and aims at reproducing drain currents measured at RCA level.

5.2.2 Optimal bias configuration

Table 15: Summary of LFI 30 and 44 GHz optimal V_d bias points

30 GHz					
Feed ID	FEM ch.	RAA DEC	RAA V	RCA V	Δ %
#27	M1	156	0.87	0.97	-11.1
	M2	157	0.87	0.97	-10.4
	S1	157	0.87	0.98	-11.1
	S2	156	0.87	0.98	-11.2
#28	M1	157	0.87	0.96	-8.8
	M2	156	0.87	0.95	-8.8
	S1	157	0.87	0.96	-9.1
	S2	158	0.88	0.96	-9.0

44 GHz					
Feed ID	FEM ch.	RAA DEC	RAA V	RCA V	Δ %
#24	M1	200	1.18	1.51	-21.8
	M2	183	1.18	1.53	-22.9
	S1	152	1.03	1.53	-32.3
	S2	157	1.01	1.48	-31.7
#25	M1	184	1.14	1.51	-24.1
	M2	185	1.15	1.53	-24.7
	S1	167	1.05	1.53	-31.2
	S2	166	1.04	1.48	-29.3
#26	M1	170	1.06	1.51	-29.3
	M2	171	1.07	1.53	-29.9
	S1	173	1.07	1.53	-29.7
	S2	170	1.07	1.48	-27.8

Table 16: Summary of LFI 70 GHz optimal V_d bias points

Feed ID	FEM ch.	RAA DEC	RAA V	RCA V	Δ %
#18	M1	121	0.48	0.38	26.7
	M2	123	0.48	0.39	25.5
	S1	139	0.55	0.43	28.5
	S2	115	0.45	0.34	34.0
#19	M1	124	0.49	0.37	32.0
	M2	126	0.50	0.38	30.6
	S1	120	0.47	0.36	31.5
	S2	125	0.49	0.39	26.2
#20	M1	121	0.48	0.36	33.3
	M2	127	0.50	0.38	31.7
	S1	132	0.52	0.40	29.3
	S2	127	0.50	0.38	31.6

Feed ID	FEM ch.	RAA DEC	RAA V	RCA V	Δ %
#21	M1	141	0.56	0.41	35.7
	M2	136	0.54	0.39	38.1
	S1	136	0.54	0.39	37.9
	S2	132	0.52	0.38	38.6
#22	M1	125	0.49	0.38	30.5
	M2	130	0.51	0.39	33.0
	S1	128	0.50	0.38	31.6
	S2	130	0.51	0.40	28.6
#23	M1	120	0.47	0.39	22.7
	M2	119	0.47	0.38	22.7
	S1	118	0.46	0.37	25.0
	S2	122	0.48	0.39	24.0

5.2.3 Criticalities and recommendations

The control of the LNA bias points at the level of the FEMs is a crucial point which has turned out to be very difficult to achieve. Because the actual bias voltages that are obtained at the FEM for a certaing DAE code depends on the grounding and on the temperature distribution along the cryo-harness we expect that these voltages will be different both during the testing on the satellite and in flight. Furthermore the models that should provide the bias voltages given the thermal

and electrical boundary conditions have proved limited predictive capability so that the model estimates has always to be refined experimentally.

The discrepancies that we observe between the values set at RAA and RCA levels (up to ∼40%) indicate that the assumption to be able to reproduce close-to-optimal conditions at the beginning of the bias tuning phase is likely not to be a correct one.

We therefore believe that the LNA bias tuning strategy (not only the drain, but also the gate voltages) should be revised in order not to depend on such assumption and be able to optimise globally performaces (noise temperature and isolation) and power consumption. The definition of such a procedure will be one of the highest priority issues in the forthcoming activities.

R.2: ***LNA bias tuning procedures should be revised in order not to depend on the assumption that starting points are already very close to the optimal condition.***

5.3 Gate 1 voltage

5.3.1 Experimental

The second step in bias tuning has been finding, for each FEM amplifier, the optimal bias point for the gate 1 voltage, Vg_1. The procedure, in this case, is to acquire data at two sky load temperatures with the twin amplifier in the off position for a series of Vg_1 values. In this case a curve of noise temperature (calculated using the classical Y factor method) *vs.* Vg_1 is built and the optimal point is found in correspondence to this minimum.

Fig. 28 shows an example of such a plot.

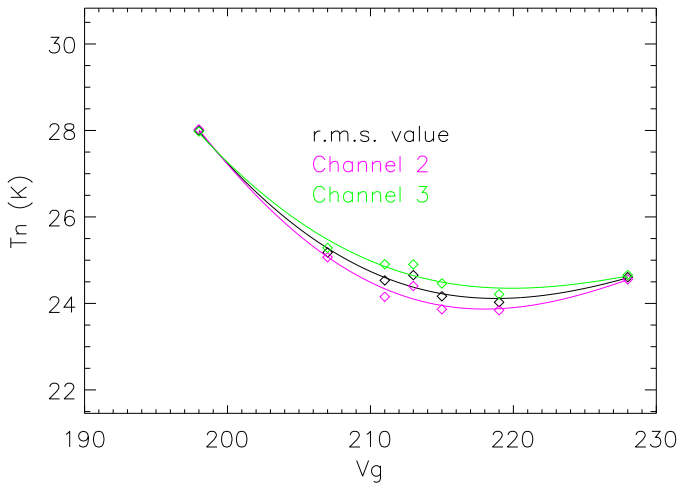

Figure 28: Plot of noise temperature *vs.* Vg_1 (DEC code) for LFI24-S1

In the following table we list the relevant datasets also indicating the value of $T_{\rm sky}$ and the difference in back-end temperature (that ranged in the interval $[37.5 - 38.0]$ K) between the two steps in sky load temperature. The reference load temperature in all the tests ranged between 22.1 and 22.2 K, while the front-end unit was at 26.4 K with a stability of $\lesssim 5$ mK.

Table 17: Datasets relevant for the Vg_1 tuning

30 GHz						
Feed ID	FEM ch.	T_{low}		T_{high}		ΔT_{BEU} (K)
		Test ID	T_{sky} (K)	Test ID	T_{sky} (K)	
#27	All channels	TUN_0020	21.6	TUN_0015	29.4	0.23
#28	M1-M2	TUN_0020	21.6	TUN_0015	29.4	0.25
	S1-S2	TUN_0021	21.6	TUN_0019	29.2	0.31
44 GHz						
Feed ID	FEM ch.	T_{low}		T_{high}		ΔT_{BEU} (K)
		Test ID	T_{sky} (K)	Test ID	T_{sky} (K)	
#24	All channels	TUN_0020	21.6	TUN_0013	29.6	0.18
#25	All channels	TUN_0020	21.6	TUN_0015	29.4	0.18
#26	All channels	TUN_0020	21.6	TUN_0015	29.4	0.19
70 GHz						
Feed ID	FEM ch.	T_{low}		T_{high}		ΔT_{BEU} (K)
		Test ID	T_{sky} (K)	Test ID	T_{sky} (K)	
#18	All channels	TUN_0020	21.6	TUN_0013	29.9	0.47
#19	All channels	TUN_0020	21.6	TUN_0013	29.9	0.47
#20	All channels	TUN_0020	21.6	TUN_0013	29.9	0.42
#21	All channels	TUN_0020	21.6	TUN_0013	29.8	0.35
#22	All channels	TUN_0020	21.6	TUN_0013	29.7	0.29
#23	All channels	TUN_0020	21.6	TUN_0013	29.7	0.19

Detailed results are reported in Annex 18.

5.3.2 Optimal bias configuration

Table 18: Summary of LFI 30 and 44 GHz optimal Vg1 bias points

30 GHz					
Feed ID	FEM ch.	RAA DEC	RAA mV	RCA mV	Δ %
#27	M1	240	1.63	1.77	-7.8
	M2	245	1.75	1.77	-1.1
	S1	238	1.58	1.74	-8.9
	S2	250	1.86	1.75	6.4
#28	M1	243	1.70	1.85	-7.8
	M2	240	1.63	1.86	-12.3
	S1	235	1.51	1.66	-8.7
	S2	245	1.75	1.85	-5.3

44 GHz					
Feed ID	FEM ch.	RAA DEC	RAA mV	RCA mV	Δ %
#24	M1	226	1.30	1.49	-12.5
	M2	227	1.32	1.49	-10.8
	S1	219	1.14	1.21	-5.5
	S2	219	1.14	1.39	-18.4
#25	M1	222	1.21	1.50	-19.6
	M2	224	1.26	1.50	-16.3
	S1	226	1.30	1.41	-7.4
	S2	219	1.14	1.34	-15.1
#26	M1	232	1.44	1.60	-9.5
	M2	232	1.44	1.60	-9.5
	S1	228	1.35	1.69	-20.0
	S2	232	1.44	1.49	-2.8

Table 19: Summary of LFI 70 GHz optimal Vg1 bias points

Feed ID	FEM ch.	RAA DEC	RAA mV	RCA mV	Δ %
#18	M1	224	1.76	1.50	17.3
	M2	179	1.40	1.50	-6.2
	S1	201	1.58	1.45	8.8
	S2	201	1.58	1.50	5.5
#19	M1	215	1.69	1.50	12.4
	M2	220	1.73	1.50	15.1
	S1	215	1.69	1.56	8.1
	S2	220	1.73	1.47	17.4
#20	M1	225	1.77	1.48	19.3
	M2	231	1.81	1.52	18.9
	S1	210	1.65	1.48	11.6
	S2	198	1.55	1.48	5.2

Feed ID	FEM ch.	RAA DEC	RAA mV	RCA mV	Δ %
#21	M1	201	1.58	1.46	7.9
	M2	210	1.65	1.45	13.6
	S1	196	1.54	1.45	6.0
	S2	201	1.58	1.49	6.0
#22	M1	179	1.40	1.42	-1.3
	M2	178	1.40	1.43	-2.2
	S1	204	1.60	1.42	12.3
	S2	220	1.72	1.45	19.3
#23	M1	223	1.75	1.51	16.3
	M2	226	1.77	1.53	16.2
	S1	197	1.55	1.53	1.5
	S2	186	1.46	1.48	-1.2

5.3.3 Criticalities and recommendations

Apart from the points already discussed in Sect. 5.2.3 we add few comments about the noise temperature calculation on which this tuning step is based.

The evaluation of the optimal Vg_1 is based on a *relative* comparison of noise temperature between the various bias points. This means that we are not interested in a precise absolute determination of $T_{\rm noise}$ which can be typically off by a factor 20-40% with respect to the "true" noise temperature. The main factors potentially impacting the absolute determination of noise temperatures are:

1. radiometers working in non nominal conditions (on leg on at a time);
2. different thermal boundary conditions in the data acquired at the two sky load temperatures. The main difference in our case was the temperature of the BEU that, in the worst case, differed by ~ 0.5 K between the two tests. Although this has obviously an impact on the absolute noise temperature value, it does not change the shape of the curve;
3. limited temperature step in the sky load. In particular we used a temperature step of $\sim$8 K in the sky load, which in some cases has limited the accuracy of the noise temperature determination for bias values particularly far from the optimal condition.

The determination of a minimum in the curve was sometimes difficult or impossible. Although ideally one should find a minimum in the $T_{\rm noise}$ vs. Vg_1 curve (see Fig. 28) in many cases the behaviour was not clear-cut so that sometimes we could not rely on the automatic procedure and we had to look at the raw data to identify the optimal bias.

In general we can identify three distinct types of curves (see last column in Table 20):

1. a curve with a well defined minimum in the range of sampled bias values (see Fig. 28),
2. a curve monotonically decreasing towards one end of the Vg_1 range (see Fig. 29, right panel), and:

3. a curve essentially flat or with a very wide minimum (see Fig. 29, left panel).

In two cases (indicated by a question mark in Table 20) we also observed a more complicated behaviour caused by unphysically high noise temperatures for some Vg_1 values which were likely to be originated by a combination of intrinsically high device noise temperature and limited temperature step in the sky load (which strongly limited the accuracy in $T_{\rm noise}$ calculated by the Y factor).

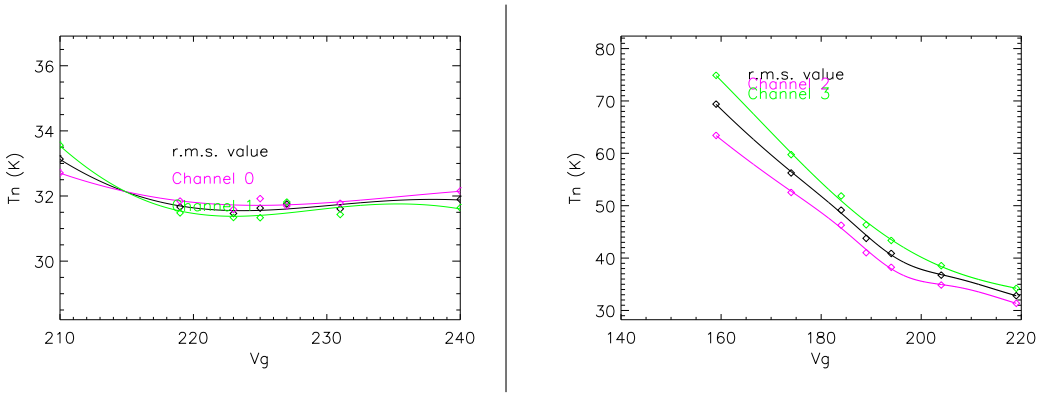

Figure 29: Examples of curve which are flat (left panel) and monotonically decreasing in the sampled range of Vg_1 values.

In the cases that required direct look at the raw data, the following criteria were followed to finally establish the bias value to be set:

- the noise temperature had to be at or close to the minimum value measured in the sampled bias interval;
- the drain current had to be not too high compared to the values expected from RCA measurements;
- the gain between two amplifiers in the same radiometer had to be not too unbalanced in order not to jeopardize the Vg_2 tuning step.

A rough check on the gain balance on the two legs of each radiometer could be done by evaluating drain currents and voltage outputs for the different Vg_1 values set in the two amplifiers.

Table 20: Behaviour of the $T_{\rm noise}$ vs Vg_1 curves according to the three categories explained above.

Feed ID	FEM ch.	Curve type
#18	S2	mono
	S1	mono
	M1	?
	M2	?
#19	S2	mono
	S1	mono
	M1	mono
	M2	mono
#20	S2	mono
	S1	mono
	M1	mono
	M2	mono
#21	S2	flat
	S1	?
	M1	min
	M2	mono
#21	S2	mono
	S1	flat
	M1	min
	M2	min
#23	S2	?
	S1	min
	M1	mono
	M2	min

Feed ID	FEM ch.	Curve type
#24	M1	min
	M2	min
	S1	min
	S2	min
#25	M1	flat
	M2	flat
	S1	flat
	S2	min
#26	M1	flat
	M2	flat
	S1	mono
	S2	flat
#27	M1	flat
	M2	flat
	S1	min
	S2	mono
#28	M1	flat
	M2	flat
	S1	mono
	S2	mono

In summary we can state the following additional recommendations concerning LNA bias tuning:

R.3: ***LNA bias tuning procedures should be performed by exploiting a step in sky load temperature not less than 10 K.***

R.4: ***Stability of thermal boundaries (e.g. BEU, FEU) must be guaranteed within the time frame during which a single radiometric leg is tested.***

5.4 Gate 2 voltage

5.4.1 Experimental

The third step in bias tuning consisted in fixing the gate 1 voltages to the optimal values found with the Vg_1 tuning procedure and then operating the receivers in nominal switching mode acquiring data at two sky load temperatures while varying the gate 2 voltages for each radiometer around a starting value corresponding to the optimal value found during the RCA test campaign.

For each pair of Vg_2 the receiver isolation, I, is computed and the optimal value is determined as the pair of gate 2 voltages that maximise I. It is worth noting that the bias sampling strategy has been very similar to the one followed for the phase switch bias tuning, i.e. the Vg_2 values for the two amplifiers have not been sampled in a square matrix, but along a line around the starting values.

In the following table we summarise the relevant datasets also indicating the value of $T_{\rm sky}$ and the difference in back-end temperature (that was $\sim$ 37.5 K) between the two steps in sky load

temperature.

Table 21: Datasets relevant for the Vg_2 tuning

30 GHz						
Feed ID	FEM ch.	$T_{\rm low}$		$T_{\rm high}$		$\Delta T_{\rm BEU}$ (K)
		Test ID	$T_{\rm sky}$ (K)	Test ID	$T_{\rm sky}$ (K)	
#27	M1-M2	TUN_0036	18.5	TUN_0031	30.0	0.14
	S1-S2	TUN_0036	18.5	TUN_0031	30.0	0.13
#28	M1-M2	TUN_0036	18.5	TUN_0031	30.0	0.30
	S1-S2	TUN_0036	18.5	TUN_0031	30.0	0.16
44 GHz						
Feed ID	FEM ch.	$T_{\rm low}$		$T_{\rm high}$		$\Delta T_{\rm BEU}$ (K)
		Test ID	$T_{\rm sky}$ (K)	Test ID	$T_{\rm sky}$ (K)	
#24	M1-M2	TUN_0047	18.6	TUN_0048	30.0	0.27
	S1-S2	TUN_0036	18.5	TUN_0031	30.0	0.11
#25	M1-M2	TUN_0036	18.5	TUN_0031	30.0	0.12
	S1-S2	TUN_0036	18.5	TUN_0031	30.0	0.12
#26	M1-M2	TUN_0036	18.5	TUN_0031	30.0	0.12
	S1-S2	TUN_0047	18.6	TUN_0048	30.0	0.31
70 GHz						
Feed ID	FEM ch.	$T_{\rm low}$		$T_{\rm high}$		$\Delta T_{\rm BEU}$ (K)
		Test ID	$T_{\rm sky}$ (K)	Test ID	$T_{\rm sky}$ (K)	
#18	M1-M2	TUN_0047	18.6	TUN_0048	30.0	0.31
	S1-S2	TUN_0036	18.5	TUN_0031	30.0	-0.1
#19	M1-M2	TUN_0036	18.5	TUN_0031	30.0	0.07
	S1-S2	TUN_0036	18.5	TUN_0031	30.0	0.08
#20	M1-M2	TUN_0036	18.5	TUN_0031	30.0	0.09
	S1-S2	TUN_0047	18.6	TUN_0048	30.0	0.31
#21	M1-M2	TUN_0036	18.5	TUN_0031	30.0	0.09
	S1-S2	TUN_0047	18.6	TUN_0048	30.0	0.27
#22	M1-M2	TUN_0047	18.6	TUN_0048	30.0	0.28
	S1-S2	TUN_0047	18.6	TUN_0048	30.0	0.28
#23	M1-M2	TUN_0047	18.6	TUN_0048	30.0	0.29
	S1-S2	TUN_0047	18.6	TUN_0048	30.0	0.29

Detailed results are reported in Annex 19 and 20.

5.4.2 Optimal bias configuration

Table 22: Summary of LFI 30 and 44 GHz optimal Vg_2 bias points

30 GHz					
Feed ID	FEM ch.	RAA DEC	RAA mV	RCA mV	Δ %
#27	M1	108	-1.28	-1.23	3.9
	M2	108	-1.28	-1.42	-9.9
	S1	86	-1.28	-1.62	-21.3
	S2	126	-1.28	-1.03	23.9
#28	M1	101	-1.19	-1.80	-33.9
	M2	112	-1.19	-0.83	43.5
	S1	88	-1.19	-1.70	-30.3
	S2	121	-1.18	-1.01	16.8

44 GHz					
Feed ID	FEM ch.	RAA DEC	RAA mV	RCA mV	Δ %
#24	M1	234	1.49	1.35	10.7
	M2	204	1.49	1.34	11.0
	S1	213	1.49	1.34	10.8
	S2	225	1.49	1.34	10.8
#25	M1	221	0.78	1.35	-41.7
	M2	212	0.79	1.25	-37.0
	S1	216	0.79	1.34	-41.5
	S2	220	0.79	1.34	-41.4
#26	M1	221	1.00	1.24	-19.2
	M2	219	1.00	1.46	-31.7
	S1	226	1.00	1.13	-11.2
	S2	217	1.00	1.63	-38.6

Table 23: Summary of LFI 70 GHz optimal Vg_2 bias points

Feed ID	FEM ch.	RAA DEC	RAA mV	RCA mV	Δ %
#18	M1	225	1.44	1.50	-3.7
	M2	168	1.44	1.52	-5.1
	S1	197	1.44	1.47	-2.1
	S2	205	1.44	1.61	-10.5
#19	M1	198	1.56	1.52	2.7
	M2	196	1.56	1.47	6.3
	S1	204	1.56	1.56	0.1
	S2	201	1.56	1.56	0.3
#20	M1	204	1.43	1.55	-7.8
	M2	206	1.43	1.57	-9.2
	S1	211	1.43	1.57	-9.1
	S2	201	1.43	1.57	-9.1

Feed ID	FEM ch.	RAA DEC	RAA mV	RCA mV	Δ %
#21	M1	207	1.53	1.49	2.5
	M2	187	1.53	1.41	8.2
	S1	197	1.53	1.41	8.2
	S2	213	1.53	1.61	-5.2
#22	M1	204	1.30	1.42	-8.5
	M2	176	1.30	1.44	-9.7
	S1	184	1.30	1.39	-6.2
	S2	199	1.30	1.50	-13.4
#23	M1	182	1.75	1.46	20.1
	M2	195	1.75	1.48	18.4
	S1	166	1.75	1.53	14.8
	S2	223	1.75	1.50	16.6

5.4.3 Criticalities and recommendations

6 Basic performances

NOTE: this section has been rewritten. Please refer to [AD5] for the older version.

With the term "basic performances" we identify those parameters that depend on the average radiometric output (in other words that do not depend on the detailed noise properties). In particular we determined the following parameters: receiver noise temperature, photometric calibration[1], response linearity and receiver isolation.

6.1 Experimental

Basic properties are derived by tests in which the average radiometric output is measured at different levels of the Sky load signal (see [RD5] for more details). Therefore the ideal test should be conducted with clearly spaced temperature steps in the sky load temperature with no variation in the other thermal stages.

Potentially useful tests. In Table 24 we list the various tests that were potentially usable for calculation of radiometric basic properties. For each test we report the sky load temperature, the time window in which the acquisition was characterised by stable conditions and some notes concerning the test. In Fig. 30 we report, for each test, the temperatures at the main thermal boundaries. The four colours correspond to the four steps in the sky load temperature.

Table 24: List of tests performed during the second calibration run potentially useful for the calculation of radiometric basic properties

Test ID	T_{sky} (K)	Time window	Notes
LIS_0007	32	[8400,9000]	Short acquisition before sky load cooldown
LIS_0008	18.5	[50000, 60000]	Sky load cooldown. Stable at the end of the curve
LIS_0009	19	[254000, 255000]	Stable acquisition
LIS_0010	30	[300000, 312000]	Sky load warmup. Stable at the end
LIS_0011	30	[317000, 318000]	Stable acquisition
LIS_0012	30	[319000, 321000]	Stable acquisition
LIS_0013	30	[352350, 352500]	Stable acquisition
LIS_0014	26	[419000, 420500]	Stable acquisition after sky load cooldown (recorded in ST3_0001)

Selection of tests with optimal thermal conditions. If we now look for the tests in which thermal conditions remain relatively unchanged apart from the sky load temperature we see that:

[1] It is worth highlighting that the photometric constant calculated on ground will not be used directly in the routine operations data analysis, but will be recalculated in flight using the CMB dipole. Ground measurement are nevertheless important because they provide a first order knowledge of the instrument performances extrapolated at flight conditions.

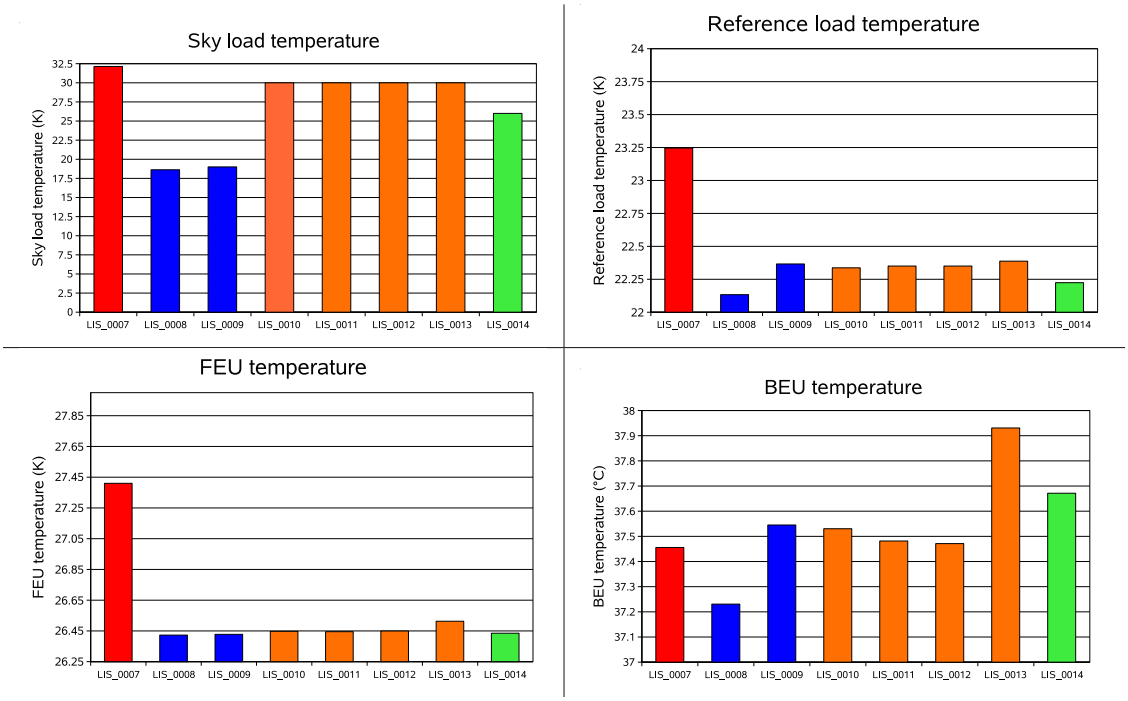

Figure 30: Values of main temperature boundaries (during stable acquisitions) in tests listed in Table 24

- test LIS_0007 was characterised by a FEU temperature and a reference load temperature which were ∼1K larger compared to the other tests;
- FEU and reference load temperatures were very stable in all the other tests ($\lesssim$ 50 mK);
- BEU temperature showed variations within 200 mK apart from LIS_0008 and LIS_0013 (in this case the difference in temperature between these two tests was $\sim$ 0.5 K).

In order to perform the calculation with the least impact from thermal non idealities we have therefore decided not to consider LIS_0007 and to choose LIS_0009, LIS_0011 and LIS_0014 for the remaining temperature steps. In Tab. 25 we summarise the main temperatures recorded in the three tests.

Table 25: Main temperatures during basic calibration temperature steps.

Test ID	$T_{\rm sky}$(K)	$T_{\rm ref}$ (K)	$T_{\rm FEU}$ (K)	$T_{\rm BEU}$ (C)
LIS_0009	19.00	22.34	26.40	37.53
LIS_0014	25.00	22.20	26.45	37.48
LIS_0011	30.00	22.32	26.40	37.67

Sky and reference load temperature sensors. Calculation of basic properties (in particular noise temperature and photometric calibration) depend critically on the choice of the temperature

sensor used to monitor the sky and reference load temperatures.

On the sky load four temperature sensors have been installed:

- two sensors on the back metal plate (1 control and 1 redundant);
- one temperature sensor on the ECCOSORB at the side of the sky load;
- one temperature senson on an ECCOSORB pyramid at the centre of the sky load.

Unfortunately during the cold tests we have observed anomalous behaviour of the two ECCOSORB sensors so that they could not be used as reliable temperature monitors. Therefore an experimetal and modeling actvity has been performed to estimate the ECCOSORB temperature using the metal plate temperature sensors. This activity led to an estimation of the temperature difference between the metal plate and the ECCOSORB centre for each one of the three input temperatures (see Tab. 26).

Table 26: Input temperatures ($T_{\rm in}$) estimated with the sky load thermal model compared to the sky load back plate measurement ($T_{\rm sensor}$).

Test ID	$T_{\rm sensor}$ (K)	$T_{\rm in}$ (K)
LIS_0009	19.00	22.05
LIS_0014	25.00	28.96
LIS_0011	30.00	32.91

On the reference loads 7 sensors were placed:

- two sensors on the HFI dummy (one control and one redundant)
- one sensor on the metal support of the LFI28 reference load (used for LFI27 and LFI28);
- one sensor on the metal support of the LFI25 reference load (used for LFI24 and LFI25);
- one sensor on the metal support of the LFI26 reference load (used for LFI26);
- one sensor on the metal support of the LFI18 reference load (used for LFI18 and LFI19);
- one sensor on the metal support of the LFI21 reference load (used for LFI20 through LFI23).

6.2 Photometric calibration, noise temperature and linearity

6.2.1 Calculation at test conditions

Noise temperature and calibration constant can be calculated by fitting the $V_{\rm out}(T_{\rm in})$ data with the most representative model. For example, in the simple case of a linear radiometer this model reads:

$$V_{\rm out} = G_0(T_{\rm in} + T_{\rm noise}) \tag{1}$$

A more representative model of the LFI receiver response is provided by the following relationship:

$$V_{\rm out} = \frac{G_0(T_{\rm sky} + T_{\rm noise})}{1 + b\,G_0(T_{\rm sky} + T_{\rm noise})} \tag{2}$$

where $V_{\rm out}$ is the voltage output, $T_{\rm sky}$ is the sky load input antenna temperature, $T_{\rm noise}$ is the noise temperature, G_0 is the photometric calibration constant in the limit of linear response and b is a non linearity parameter. For linear receivers $b = 0$, while for the LFI receivers, which show a slightly compression at high input temperatures, $b \gtrsim 0$.

The experimental conditions during the RAA tests were not ideal for this kind of test, this because of the long time required to induce temperature steps on the sky load, for the poor thermal decoupling between the sky load temperature and the reference loads temperature and for the minimal temperature monitoring available on the sky load pyramids.

In Fig. 31 we show the three LIS Voltage - Temperature points for RCA25. These data show that data with a sort of "anti-compression", also called "extension", i.e. the voltage tends to rise with the input temperature. This behaviour has been seen in all detectors and made the non linear fit with Eq. 2 very problematic. The situation was also worsened by the fact that the fit is performed only with three points (for three parameters)

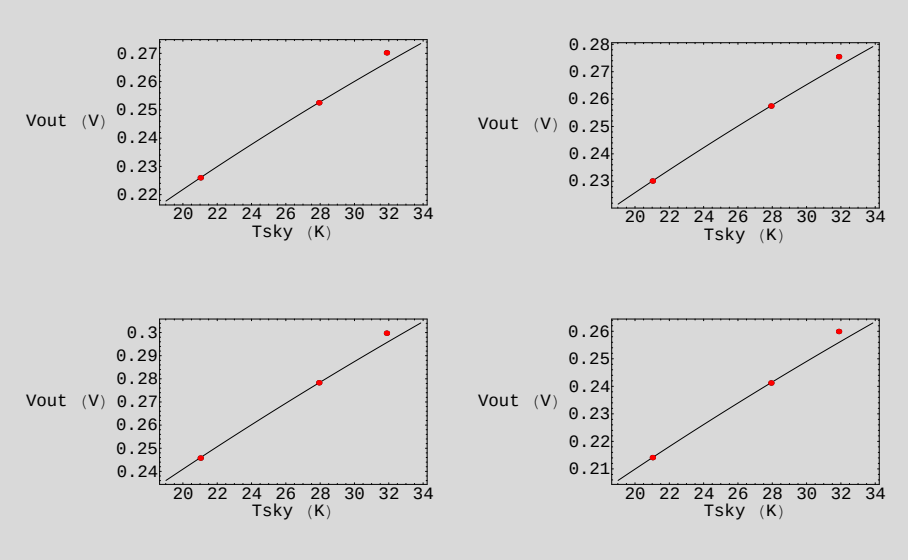

Figure 31: Receiver output for the four detectors of LFI25 during RAA tests

Because fitting a three parameters function with just three data points is quite marginal and it actually leads to results affected by the unexplained "extension" of the points at high temperature we have constrained the fitting routine around the nonlinear parameter b. Basically the idea is that because the non linearity is determined mainly by the BEMs, this should not be too much different in the RAA tests as the temperature was about the same as during the RCA tests. Therefore the fitting routine constrains b to be in an interval of max $\pm 1\%$ from the RCA value

For each detector the data is represented by two vectors having three values each: $T_{\rm in}$, corresponding to average input antenna temperature and $V_{\rm out}$, corresponding to average output voltage. The three values come from the following tests: LIS_0009 (time window [254000, 255000]), LIS_0011 (time window [317000, 318000]), and LIS_0014 (time window [419000, 420500]).

The temperature values come from the sky load metal plate sensor with a correction in order to get the best estimate of the ECCOSORB temperature.

The procedure is based on the Mathematica function `NMinimize` and the argument to the

function is the χ^2 defined by:

$$\chi^2 = \sum_{i=1}^{N} \frac{(V_{\mathrm{model,i}} - V_{\mathrm{meas,i}})^2}{\sigma_i^2} \tag{3}$$

In Table 27 we summarise the best-fit parameters obtained for all the LFI detectors. Notice that the non-linear parameter b for all the 70 GHz receivers is always very small ($\lesssim 10^{-3}$) which is equivalent, in practice, to a linear response.

Table 27: Best fit parameters obtained from the non linear fit of the RAA data

		R0D0	R0D1	R1D0	R1D1
	b	N/A	N/A	$\lesssim 10^{-3}$	$\lesssim 10^{-3}$
LFI18	G_0 (V/K)	N/A	N/A	0.026	0.022
	T_{noise} (K)	N/A	N/A	37.4	40.5
	b	$\lesssim 10^{-3}$	$\lesssim 10^{-3}$	$\lesssim 10^{-3}$	$\lesssim 10^{-3}$
LFI19	G_0 (V/K)	0.020	0.021	0.016	0.018
	T_{noise} (K)	39.8	38.7	37.5	40.0
	b	$\lesssim 10^{-3}$	$\lesssim 10^{-3}$	$\lesssim 10^{-3}$	$\lesssim 10^{-3}$
LFI20	G_0 (V/K)	0.019	0.018	0.025	0.025
	T_{noise} (K)	42.3	42.2	43.9	43.0
	b	$\lesssim 10^{-3}$	$\lesssim 10^{-3}$	$\lesssim 10^{-3}$	$\lesssim 10^{-3}$
LFI21	G_0 (V/K)	0.025	0.023	0.016	0.014
	T_{noise} (K)	31.9	34.6	43.3	45.9
	b	$\lesssim 10^{-3}$	$\lesssim 10^{-3}$	$\lesssim 10^{-3}$	$\lesssim 10^{-3}$
LFI22	G_0 (V/K)	0.011	0.012	0.014	0.016
	T_{noise} (K)	40.5	38.9	40.8	43.5
	b	$\lesssim 10^{-3}$	$\lesssim 10^{-3}$	$\lesssim 10^{-3}$	$\lesssim 10^{-3}$
LFI23	G_0 (V/K)	0.025	0.029	0.014	0.007
	T_{noise} (K)	40.6	39.2	50.3	54.2
	b	N/A	N/A	1.53	1.51
LFI24	G_0 (V/K)	N/A	N/A	0.005	0.006
	T_{noise} (K)	N/A	N/A	18.7	19.0
	b	1.29	1.21	0.89	1.10
LFI25	G_0 (V/K)	0.008	0.008	0.008	0.007
	T_{noise} (K)	18.6	18.9	18.5	19.0
	b	1.10	1.41	0.95	1.22
LFI26	G_0 (V/K)	0.005	0.006	0.007	0.007
	T_{noise} (K)	19.9	19.0	18.3	18.0
	b	0.11	0.11	0.12	0.11
LFI27	G_0 (V/K)	0.069	0.075	0.067	0.052
	T_{noise} (K)	14.9	14.6	15.3	15.9
	b	0.18	0.15	0.18	0.19
LFI28	G_0 (V/K)	0.076	0.101	0.070	0.060

$T_{\rm noise}$ (K)	11.4	11.8	11.0	11.0

6.2.2 Noise temperature comparison with RCA measurements

In order to compare noise temperature with RCA mesurements we needed to extrapolate it at the focal plane temperature of 20 K (which is the FEM temperature of the RCA tests. For more details refer to [RD3]).

This is a non trivial step to be performed if we want to consider all the elements in the extrapolation. Here we focus on a zero-order approximation based on the following assumptions:

1. the radiometer noise temperature is dominated by the front-end noise temperature, such that $T_{\rm noise} \sim T^{\rm FE}_{\rm noise}$;
2. we neglect any effect on the noise temperature given by resistive losses of the front-end passive components;
3. we assume the variation of $T^{\rm FE}_{\rm noise}$ to be linear in $T_{\rm phys}$.

Under these assumptions the receiver noise temperature at nominal front-end temperature can be written as:

$$T_{\rm noise}(T_{\rm nominal}) = T_{\rm noise}(T_{\rm test}) + \frac{\partial T^{\rm FE}_{\rm noise}}{\partial T_{\rm phys}} \Delta T_{\rm phys} \tag{4}$$

where $\Delta T_{\rm phys} = T_{\rm nominal} - T_{\rm test}$.

In Fig 32 we compare the RAA extrapolated noise temperatures with those measured at RCA level. Error bars indicated on the RAA measurements are indicative of the goodness of the fit and have been derived by performing a small Monte Carlo of the fitting procedure with 20 possible data point triplets in the accuracy range of temperature and voltage measurements.

The agreement for the 30 and 44 GHz is quite good while the same concordance has not been found for all 70 GHz detectors. We believe that this reflects the fact that 30 and 44 GHz RCA were tested in the same laboratory and following the same test procedures during RCA and RAA tests, while some differences exist in the 70 GHz RCA testing procedures which might have introduced uncertainties difficult to estimate.

Results are also reported in Table 28.

6.3 Isolation

6.3.1 Definition and requirement.

The output of the LFI pseudo-correlation receivers is a sequence of sky and reference load signals alternating at twice the phase switch frequency. If the pseudo-correlator is not ideal the separation after the second hybrid is not perfect and a certain level of mixing between the two signals will be present in the output. (*Expand, list the causes of isolation, i.e. hybrid, gain mismatch and phase switch amplitude mismatch*).

A general relationship representing the receiver power output can be written as:

$$\begin{aligned} p_{\rm out} &= aG_{\rm tot}k\beta\left[(1-\epsilon)T_{\rm sky} + \epsilon T_{\rm ref} + T_{\rm noise} + \right. \\ &- \left. r\left((1-\epsilon)T_{\rm ref} + \epsilon T_{\rm sky} + T_{\rm noise}\right)\right] \end{aligned} \tag{5}$$

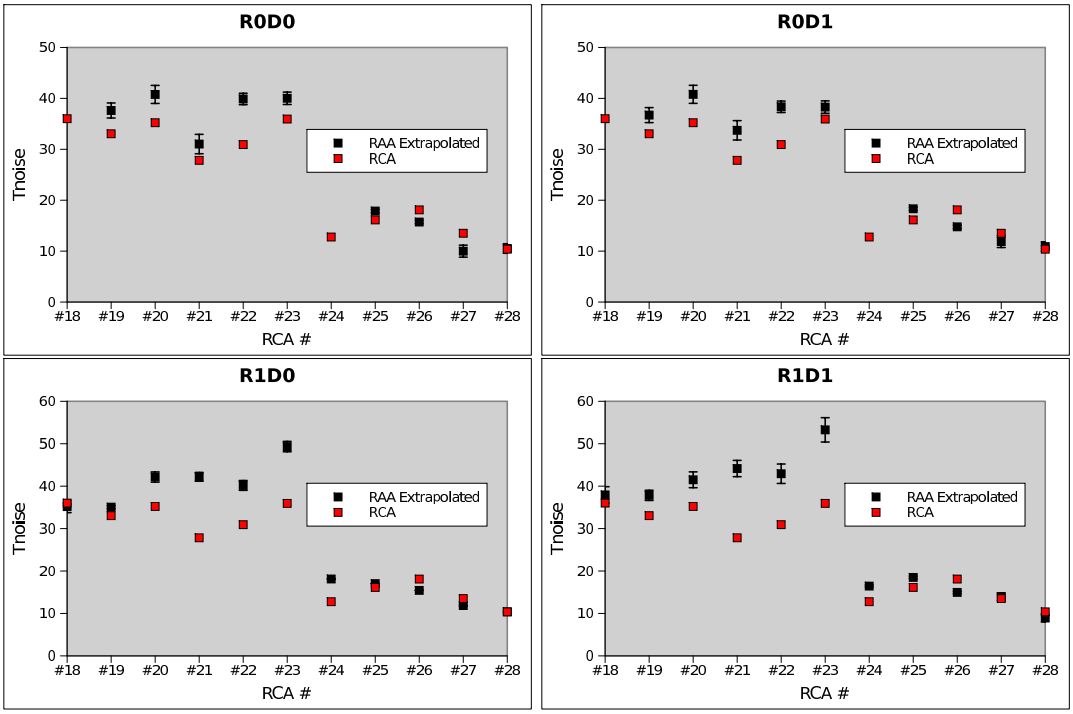

Figure 32: Comparison of RAA and RCA noise temperatures. RAA noise temperatures have been extrapolated to 20 K FEM temperature using Eq. 4.

where the parameters ϵ represents the degree of mixing or, in other words, the isolation.

Let us now imagine the receiver scanning the sky and therefore measuring a variation in the sky signal given by the CMB, $\Delta T_{\rm CMB}$. If we define $r = (T_{\rm sky} + T_{\rm noise})/(T_{\rm ref} + T_{\rm noise})$ and develop Eq. (5) in series up to the first order in ϵ we see that the differential power output is proportional to:

$$p_{\rm out} \propto \Delta T_{\rm CMB}\,(1 - \delta_{\rm iso}) \tag{6}$$

where $\delta_{\rm iso} = \frac{2T_{\rm noise}+T_{\rm sky}+T_{\rm ref}}{T_{\rm noise}+T_{\rm ref}}\epsilon$, which provides an useful relationship to estimate the requirement on the isolation, $\epsilon_{\rm max}$ provided an acceptable level of $\delta_{\rm iso}^{\rm max}$.

If we define $\delta_{\rm iso}^{\rm max} \sim 0.1$ and consider typical values for the LFI receivers ($T_{\rm ref} \sim 4.5$ K and $T_{\rm noise}$ ranging from ~ 10 to ~ 30 K) we find $\epsilon_{\rm max} \sim 0.05$ equivalent to ~ -13 dB, which corresponds to the requirement for LFI receivers.

6.3.2 Measurement.

The isolation is measured by recording the average radiometer voltage outputs, $V_{\rm sky}$ and $V_{\rm ref}$, at two different input temperatures, T_1 and T_2, of the sky load[2]. If $\Delta V_{\rm sky}$ and $\Delta V_{\rm ref}$ are the voltage output variations induced by $\Delta T = T_2 - T_1$ then it is easy to see from Eq. (5) (with the

[2]The test can be conducted, in principle, also by changing the reference load temperature

Table 28: RAA noise temperatures compared with RCA measurements. The second column reports the RAA noise temperature extrapolated at the RCA conditions

	R0D0			R0D1		
	RAA	***RAA Ex***	**RCA**	***RAA***	***RAA Ex***	***RCA***
#18	N/A	N/A	36.01	N/A	N/A	36.06
#19	39.78	37.62	33.05	38.69	36.71	31.50
#20	42.27	40.77	35.22	42.17	40.79	34.23
#21	31.93	31.03	27.83	34.63	33.73	29.39
#22	40.48	39.88	30.93	38.95	38.35	30.30
#23	40.62	40.02	35.94	39.25	38.29	34.15
#24	N/A	N/A	12.77	N/A	N/A	12.44
#25	18.59	17.87	16.13	18.92	18.32	16.83
#26	19.91	15.71	18.10	18.97	14.77	17.25
#27	14.86	10.00	13.51	14.59	11.89	13.26
#28	11.42	10.52	10.38	11.79	10.89	10.72

	R1D0			R1D1		
	RAA	***RAA Ex***	**RCA**	***RAA***	***RAA Ex***	***RCA***
#18	37.46	35.18	33.85	40.46	37.94	35.11
#19	37.46	35.06	32.22	40.05	37.83	33.57
#20	43.95	42.15	36.85	43.00	41.50	34.96
#21	43.28	42.20	35.54	45.95	44.15	37.76
#22	40.78	40.18	30.33	43.53	42.93	31.83
#23	50.35	49.33	33.90	54.23	53.27	31.05
#24	18.72	18.12	13.29	19.03	16.45	13.28
#25	18.54	17.04	16.85	18.97	18.49	16.84
#26	18.26	15.44	16.60	17.96	14.96	16.33
#27	15.35	11.87	13.96	15.95	13.91	14.50
#28	10.98	10.38	9.98	10.90	8.92	9.91

approximation $(1-\epsilon) \simeq 1$) that:

$$\epsilon \simeq \frac{\Delta V_{\rm ref}}{\Delta V_{\rm sky} + \Delta V_{\rm ref}}. \tag{7}$$

If the reference load temperature is not perfectly stable but varies by an amount $\Delta T_{\rm ref}$ during the measurement this can be corrected at first order if we know the photometric constant G_0. In this case Eq. (7) becomes:

$$\epsilon \simeq \frac{\Delta V_{\rm ref} - G_0 \Delta T_{\rm ref}}{\Delta V_{\rm sky} + \Delta V_{\rm ref} - G_0 \Delta T_{\rm ref}}. \tag{8}$$

Measuring accurately the isolation, however, is generally difficult and requires a very stable environment. In fact any change in $\Delta V_{\rm ref}$ caused by other systematic fluctuations (e.g. temperature fluctuations, $1/f$ noise fluctuations) will impact the isolation measurement causing an over or under-estimation depending on the sign of the effect.

To estimate the accuracy in our isolation measurements we have first calculated the uncertainty caused by a systematic error in the reference load voltage output, $\Delta V_{\rm ref}^{\rm sys}$. If we substitute in Eq. (8) $\Delta V_{\rm ref}$ with $\Delta V_{\rm ref} \pm \Delta V_{\rm ref}^{\rm sys}$ and develop at first order in $\Delta V_{\rm ref}^{\rm sys}$ we obtain:

$$\epsilon \sim \epsilon_0 \mp \frac{\Delta V_{\rm sky}}{\Delta V_{\rm sky} + \Delta V_{\rm ref} - G_0 \Delta T_{\rm ref}} \Delta V_{\rm ref}^{\rm sys} \equiv \epsilon_0 \mp \delta\epsilon \tag{9}$$

where we indicate with ϵ_0 the isolation given by Eq. (8).

Then we have estimated $\delta\epsilon$ in our measurement conditions. Because the three temperature steps were implemented in about one day we have evaluated the total power signal stability on this timescale from the long duration test ST1_0002. For each detector datastream we have first removed spurious thermal fluctuations by correlation analysis with temperature sensor data then we calculated the peak-to-peak variation in the reference load datastream.

In Fig. 33 we summarise the measured isolation for all detectors and provide a comparison with similar measurements performed during the RCA test campaign.

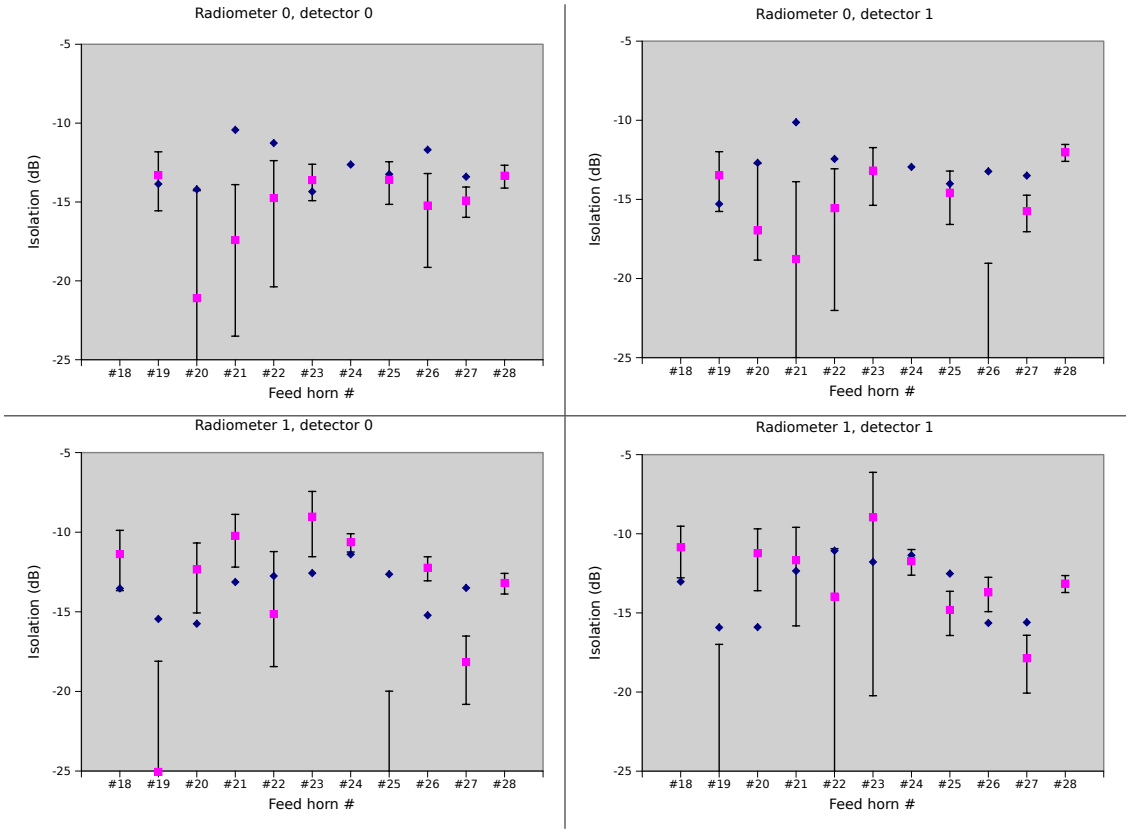

Figure 33: Summary of measured isolation compared with the same measurements performed at RCA level.

From Fig. 33 it is apparent that many of the isolation values measured during the RAA tests are characterised by high uncertainties and the comparison with RCA values not always is within the estimated error bars. Some of the values, in particular, were very low (< 25 dB) and are believed to be too low to be realistic.

Taking into account the limitations given by the measurement setup the results show that the isolation upper limit generally lie within the -13 dB requirement, apart from some cases for which the isolation is ~ -10 dB.

7 Noise properties

7.1 Noise properties

Noise characterization is a key objective in understanding a radiometer performance. Tests were performed during the RAA campaign to determine the main noise parameters of LFI radiometers (although, extra and final noise characterization will be done during flight). These parameters are: white noise level, $1/f$ knee frequency, $1/f$ slope, and noise effective bandwidth. The tests also allow us to check if the data present anomalies in the time and frequency domains.

We investigated LFI RAA noise using data that were acquired in a stable thermal environment ($\sim$ 20 K), using the correct instrument bias configuration. We analyze data in three situations: noise from single diodes in switching conditions, noise from combined diodes in switching conditions for a given radiometer, and noise from unchopped data in different switch states. Here we summarize the main characteristics of the LFI radiometer's noise in each one of these situations. A description of experimental conditions, a comparison between RAA and RCA noise, and a discussion of LFI noise performance are presented as well.

7.2 Switching data

We have examined data from long duration test ST1_0002 to characterize noise from single and combined diodes in switching conditions. The data set was acquired in a stable thermal environment, from 09/02/2006 through 09/04/2006, and it contains 44h18m34s of data acquired in nominal mode (COM5) with optimized bias values.

7.2.1 Thermal environment

During ST1_0002 data acquisition, sky and reference physical temperatures were about 19 K and 22.3 K, respectively (see Fig. 34). Sky Load 1 & 2 temperature sensors presented lower rms ($\pm$0.005 K) than Reference Load 1 & 2 temperature sensors ($\pm$0.05 K). The BEU 2 temperature sensor presents higher rms ($\pm$0.1 K) than BEU 1 ($\pm$0.006 K). There is an evident BEU temperature periodic fluctuation with a 24 h period (ie, the time separation between two consecutive maximums, or minimums, is 24 h). Although it is not so evident, the Sky Load 2 temperature also presents the same periodic behavior (there is a non negligible correlation between Sky Load 2 and BEU 1 of 0.22). This behavior is not evident on Reference 1 & 2 sensors. There is a slow and continuous increase in reference temperature ($\sim$ 0.7 mK/hour), until it reaches a maximum at about 38h4m when an abrupt decrease occurs. The Reference temperature goes from 22.27 K to 22.45 K in about 36 h, then it drops to 22.3 K in about 2.5 h. This reference behavior was due to a small leak in one of the helium tanks of the cryo chamber. Despite long term variations on thermal environment, this test provided several hours of stable data that are useful for characterization of LFI RAA noise properties.

7.2.2 Scientific time ordered data

During ST1_0002 data acquisition, sample rates for 30 GHz, 44 GHz, and 70 GHz channels were 32.5 Hz, 46.5 Hz, and 78.8 Hz, respectively. Long thermal environment fluctuations can be perceived in the sky and reference data by visual inspection of time domain plots, although 70 GHz data show less susceptibility to that. Figure 35 shows an example of long thermal environment fluctuations in the sky data.

Visual inspection of frequency domain plots shows that power spectra from some channels of #18, #21, #24, #25, and #26 present a few spikes in the frequency domain. Radiometers

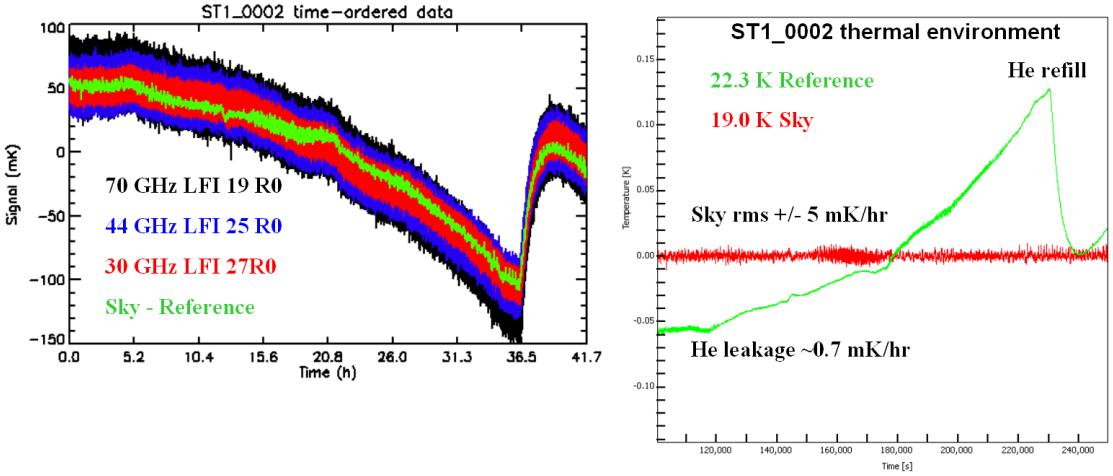

Figure 34: ST1_0002 TOI and thermal environment. The mean was removed from the sky and reference temperature sensors. We overplot the temperature sensor difference on the TOI. The radiometer's data follow the thermal environment behavior. This is a good check for the calibration as well.

#19, #20, #22, #23, #27, and #28 "seem" free of spikes. We have found no evidence that the spikes significantly affect our noise estimations. Figure 34 shows ST1_0002 TOI and thermal environment. Figure 36 show a comparison between power spectra with and without frequency spikes.

7.2.3 Data selection

We computed white noise properties from 10 sections in ST1_0002 (1 hour length each), covering the interval from 100000 s to 136000 s.

To characterize $1/f$, we have used two procedures to obtain an averaged power spectrum to use in the $f_{\rm knee}$ calculation. The first one was based on averaging three ASDs obtained from three sections with 10 hours each, while the second one was based on averaging eigth ASDs obtained from eigth sections with 4 hours each. The two procedures were basically equivalent. The data reported here are relative to the first procedure.

Due to an operational problem, ST1_0002 #26 data were not acquired with correct REBA settings. Therefore, we have used LIS_0009 data test for #26 noise estimation. In this test, the sky was set to 19 K and reference to 22 K, so the thermal environment was very similar to the ST1_0002. In LIS_0009, data were acquired in AVR1 mode, 16 Hz sample rate, and there are only 17 minutes with nominal gain and offsets (ie, 1/f could not be well characterized here). Even though, we were able to estimate white noise, and noise effective bandwidth. We were also able to compare results from AVR1 and COM5 modes for all other channels. White noise and bandwidth results from the comparison of LIS_0009 and ST1_0002 show good agreement.

Finally we obtained calibrated white noise extrapolated to flight conditions according to the procedure described in [RD3].

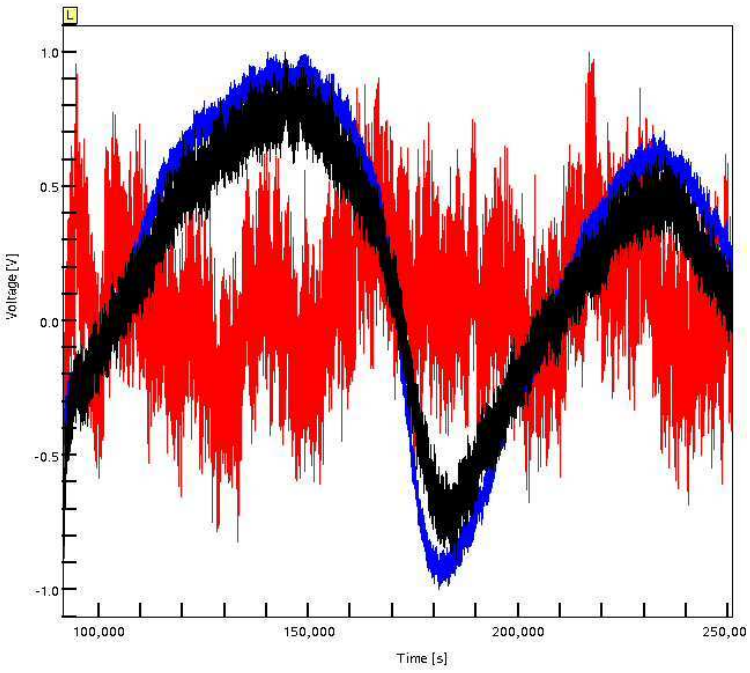

Figure 35: Example of long thermal environment fluctuations in the sky data from ST1_0002 TOI. The 30 GHz and 44 GHz channels (black and blue curves) were more susceptible to that than 70 GHz channels (red curve). The data were normalized to $[-1, 1]$ to highlight the thermal fluctuations. Despite long term variations on thermal environment, this test provided several hours of stable data that are useful for characterization of LFI RAA noise properties. The time separation between two consecutive maximums, or minimums, is about 24 h.

7.2.4 Unchopped data

Here we summarise results obtained with receivers working with phase switches in off condition. The aim of this analysis was to verify that the noise properties were independent from the phase switch state.

The noise parameters for unchopped data have been obtained from tests UNC_0001, UNC_0003, UNC_0004, UNC_0005, UNC_0006, UNC_0007, UNC_0008, UNC_0009, UNC_0010, UNC_0011, and UNC_0012. In all these tests, data were acquired in RAW0 mode data at 8192 Hz, and for each phase switch state there are about 60 seconds of data available. Unfortunately, for some combinations of channels and phase switch states there are no useful data for noise estimation because the data section were too short. During these tests, the thermal environment was very similar to the ST1_0002. To perform UNC analysis, we calibrate each receiver using the same calibration applied to single diode, and we investigate if is there any amplitude spectrum density phase switch dependency.

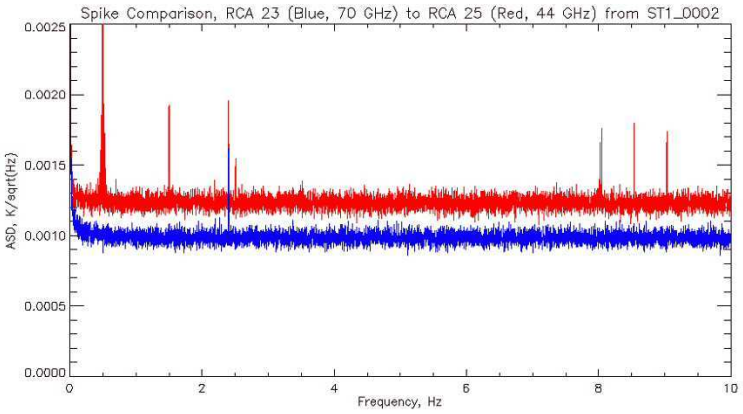

Figure 36: Comparison showing power spectra from differenced data with and without frequency spikes. We have found no evidence that the spikes significantly affect our noise estimations.

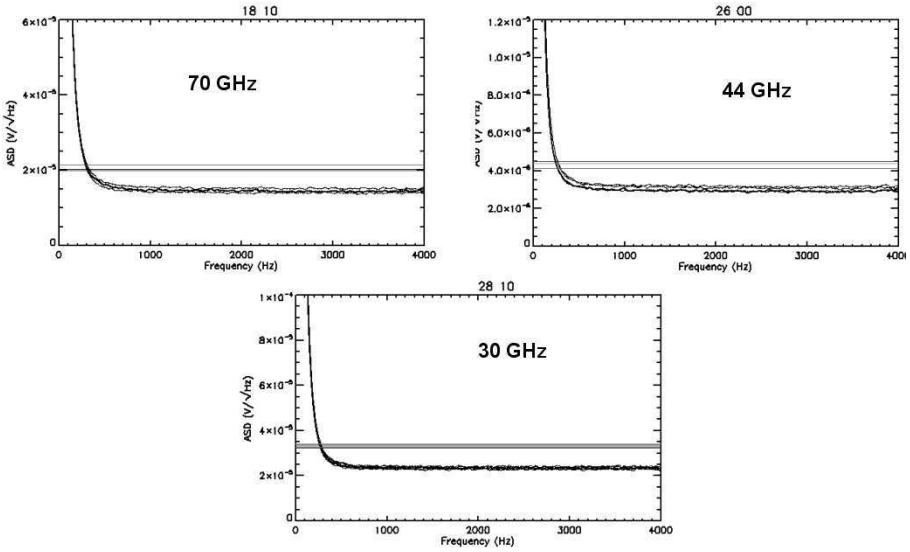

Figure 37: Examples of ASD comparison for all four phase switch states. This comparison shows that there are no ASD phase switch dependence. Small variations in the white noise level are due to the fact that one leg of the radiometer is looking to the reference load, the other leg is looking to the sky load, and there is a temperature difference between them. The solid lines show the white noise times $\sqrt{2}$. The interception between the ASD and the lines gives an estimation of the $1/f$ knee frequency.

7.2.5 Noise internal consistency

LFI receiver noise can be estimated using the radiometer equation

$$\sigma_T = K\left(\frac{T_{\rm sys}+T_{\rm sky}}{\sqrt{\beta\cdot\tau}}\right), \tag{10}$$

where σ_T is the root-mean-square noise, $T_{\rm sys}$ is the system noise temperature, $T_{\rm sky}$ is the sky antenna temperature, β is the effective noise bandwidth, τ is the integration time, and K is the sensitivity constant of the receiver. The relevant sensitivity constants for LFI are $K = 1$ for single detector in unswitched condition (from the fact that we are acquiring data in total power mode), $K = 2$ for single detector differenced data (from the fact that we spend half of the time looking to the reference load and we perform a difference between sky and reference data), and $K = \sqrt{2}$ for combined detector differenced data (from the fact that we average single detector differenced data). This basic relation allows to test internal consistency among data tests. Figure 38 shows an ASD comparison for the three data conditions.

The double-diode difference noise measurements are in agreement with the fact that, because we combine data from two detectors and average them, double-diode difference should present a noise level lower than single-diode difference of about $(\sqrt{\sigma_0^2+\sigma_1^2})/2$, where σ_0 and σ_1 denote white noise of diode 0 and diode 1 for a given radiometer. The UNC white noise measurements are in agreement with the fact that unchopped noise should be lower than single-diode difference noise by a factor of about 2. The only exception is LFI#23 R0 that presents a lower unchopped noise when compared to single difference data. We have found no dependency of the amplitude spectral density with respect to the different switch states. Figure 37 shows examples of ASD for all four phase switch states.

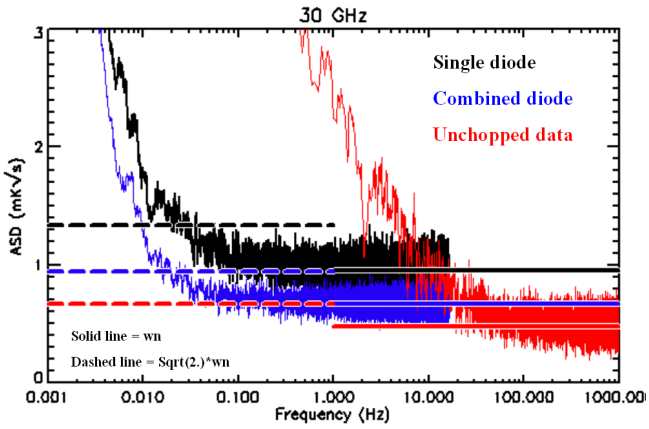

$K = 2$

$K = \sqrt{2}$

$K = 1$

Figure 38: Example of an ASD comparison between single diode, combined diode, and unchopped data. Solid lines show white noise level of each data. Dashed line is the white noise times $\sqrt{2}$. On the right, the sensitivity constant for each data according to Equation 10. These examples show that LFI presents internal consistency among dedicated tests, and consistency with most basic model. The effect of reducing $1/f$ noise due switching is self evident. The effect of improving sensitivity by averaging data is also evident.

7.3 Noise properties summary

NOTE: this section has been mostly modified. Please refer to [AD5] for the older version.

In this section we provide a summary of the various measured noise parameters. For each table, where necessary, we also provide references to the documentation addressing further discussion and analysis. Where possible and meaningful we have provided a comparison with measurements at RCA level. In particular we have not included $1/f$ parameters measured at RCA level as in this case the measurement setup (especially at 70 GHz) was not stable enough for a reliable characterisation.

Table 29 summarises the white noise level for differenced data from each diode.

Table 29: Summary of uncalibrated white noise in $\mu V \times \sqrt{s}$ for differenced data.

	R0D0	R0D1	R1D0	R1D1
#18	7.14	9.75	27.94	21.99
#19	23.66	24.17	18.30	19.41
#20	22.13	22.23	31.69	29.86
#21	23.91	23.02	18.90	18.30
#22	12.12	13.75	14.96	17.02
#23	27.02	29.32	17.02	8.65
#24	1.93	2.33	4.25	3.79
#25	5.30	5.36	6.69	4.96
#26	4.28	4.45	6.25	4.44
#27	44.15	46.76	40.36	37.87
#28	37.39	48.73	33.65	31.14

Noise effective bandwidths are reported in Table 30 and Fig. 39 with a comparison with measurements performed during RCA tests.

The characterisation of the $1/f$ noise has been performed fitting two different noise models. The first one is the simple white noise + $1/f$ described by the following relationship:

$$P(f) = \sigma^2 \left[1 + \left(\frac{f}{f_{\rm knee}}\right)^{\alpha}\right] \tag{11}$$

where $P(f)$ represents the noise power spectrum. Eq. 11 was fitted using both a non linear fitting routine to the whole spectrum and using a simpler double-linear fit to the log-log representation of the power spectrum. The second method was eventually used as prvodided a more roubust fitting method.

The second model was a two $1/f$ component mode described by the following relationship:

$$P(f) = \sigma^2 \left[1 + \left(\frac{f}{f_{\rm knee,1}}\right)^{\alpha_1} + \left(\frac{f}{f_{\rm knee,2}}\right)^{\alpha_2}\right] \tag{12}$$

This second model turned out to provide slightly better fits but we eventually decided to use, as baseline model, the simpler one as it is much more usable also in the context of the DPC simulations, that would have needed important modifications with only a slight improvement in accuracy. Full details of this analysis is provided in [RD7].

Table 30: Summary of noise effective bandwidths measured at RCA and RAA levels.

	R0D0		R0D1		R1D0		R1D1	
	RAA	RCA	RAA	RCA	RAA	RCA	RAA	RCA
#18	N/A	10.19	N/A	10.06	11.83	8.37	14.95	10.54
#19	10.10	8.96	10.40	8.70	10.72	8.51	12.13	11.45
#20	11.64	11.10	10.47	9.61	10.58	10.47	11.66	10.55
#21	12.28	11.63	12.77	11.73	12.23	11.37	10.76	9.82
#22	12.20	10.02	11.45	10.08	12.99	9.79	13.56	8.79
#23	12.71	10.64	14.31	12.12	13.84	12.55	13.54	11.41
#24	N/A	7.71	N/A	5.25	5.89	6.24	7.85	8.21
#25	7.34	6.89	7.42	6.92	5.43	5.04	7.49	7.01
#26	6.20	6.61	6.78	6.85	5.22	5.62	8.40	8.42
#27	7.81	8.60	7.81	8.53	8.71	9.48	7.03	7.82
#28	8.21	9.29	8.11	9.31	8.99	10.21	8.22	9.13

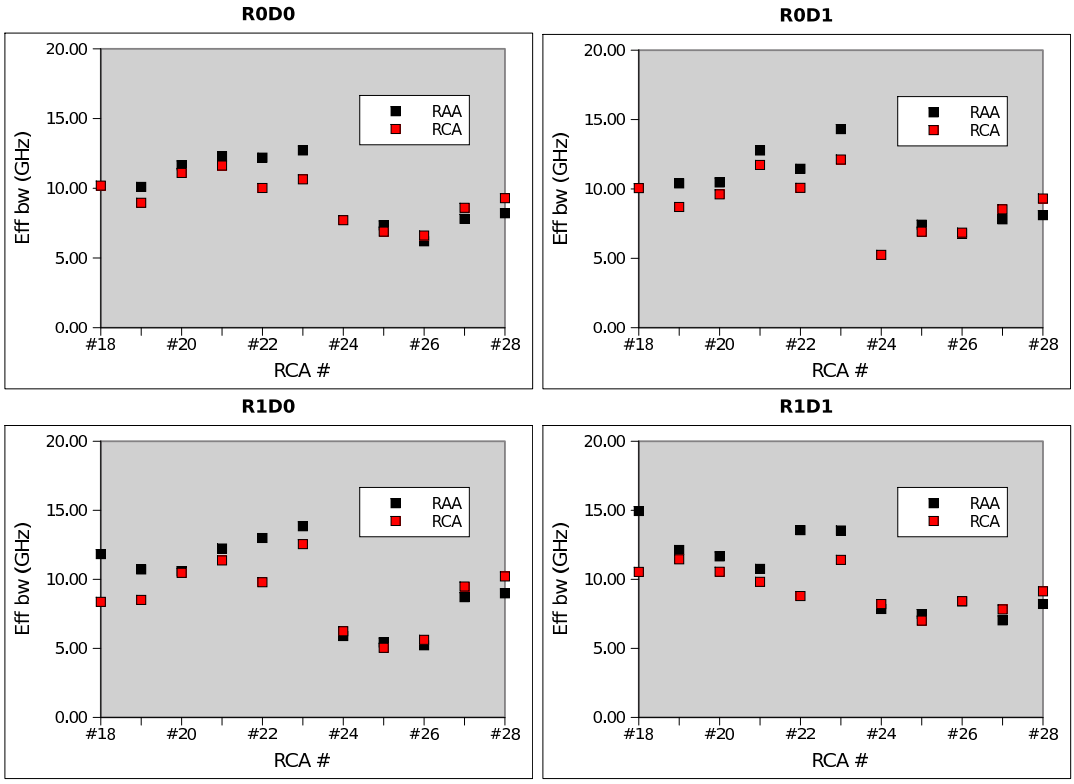

Figure 39: Noise effective bandwidths measured at RCA and RAA levels.

Finally we provide a summary of calibrated white noise (at detector, radiometer and frequency channel levels) estrapolated at 3 K input sky conditions compared with requirement levels.

The estimation of the calibrated white noise in flight conditions from the ground measured data

Table 31: Summary of knee frequencies and slopes measured during RAA tests and obtained with a simple $1/f$ component fit.

	R0D0		**R1D0**		**R0D1**		**R1D1**	
	$f_{\rm knee}$ (mHz)	slope	$f_{\rm knee}$ (mHz)	slope	$f_{\rm knee}$ (mHz)	slope	$f_{\rm knee}$ (mHz)	slope
#18	N/A	N/A	N/A	N/A	7	-1.20	50	-1.17
#19	17	-1.56	23	-1.22	21	-1.44	25	-1.29
#20	12	-1.55	10	-1.99	16	-1.53	20	-1.49
#21	18	-1.64	22	-1.78	32	-1.2	30	-1.19
#22	37	-1.23	31	-1.2	27	-1.18	66	-1.01
#23	21	-1.26	20	-1.44	50	-1.23	69	-1.13
#24	N/A	N/A	N/A	N/A	32	-1.11	36	-1.06
#25	25	-1.31	24	-1.19	14	-1.51	23	-1.33
#26	13	-1.17	9	-1.35	8	-1.16	14	-1.55
#27	22	-1.44	20	-1.39	16	-1.50	17	-1.46
#28	28	-1.31	23	-1.33	26	-1.24	28	-1.16

is not a straightforward and trivial task, especially because it depends on the receiver response that in the 30 and 44 GHz receivers is not linear in the input signal range involved in the extrapolation.

To perform this estimation we have followed two different approaches: the first is based on the following steps:

1. start from the uncalibrated white noise measured during RAA tests;
2. extrapolate the uncalibrated noise to nominal front end unit temperature using the thermal susceptibility parameters estimated at RCA level;
3. extrapolate the uncalibrated noise to 3K temperature input using the radimeter equation;
4. calibrate in temperature units using the basic performance parameters (always measured on the RAA, refer to Section 6).

This approach is described in detail in [RD3].

The second approach is based on the radiometer equation using 3K as the temperature input, Noise temperatures measured during RCA tests and noise effective bandwidths measured during RAA tests. The procedure is discussed in detail on the LFI wiki page:

`http://belzebu.lambrate.inaf.it/twiki/bin/view/LFI/NoiseEstimatedPerformance`

The two approaches have different advantages and disadvantages. In particular the first one has the advantage to start from a direct noise measurement but, on the contrary, involves many steps that somewhat increase the uncertainties. The second is simpler but it relies on an analytical formula instead of a direct noise measurement.

In Table 33 and Fig. 40 we provide a summary of in flight sensitivities per radiometer estimated according the two procedures, while in Table 34 and Fig. 41 we show the estimated in-flight sensitivity per frequency channel. The averaging has been performed using a quadrature weighted averaging using the inverse of noise levels as weights (i.e. detectors with a higher noise have a smaller weight in the average).

The data show that at 30 and 44 GHz the concordance of the two estimates is quite good, while the scatter at 70 GHz is larger, especially for estimates obtained from the uncalibrated white noise measurement.

This is consistent with the smaller uncertainties on the various parameters obtained at 30 and 44 GHz that were calibrated and tested according to the same procedures in the same laboratory.

Table 32: Summary of calibrated white noise per detector at 3 K sky input compared with requirements. Values obtained from uncalibrated white noise measured during the RAA tests.

	R0D0	R0D1	R1D0	R1D1	Requirement
#18	N/A	N/A	667.27	635.66	512.6
#19	767.43	749.54	726.65	723.18	512.6
#20	772.25	826.90	857.58	795.58	512.6
#21	571.14	605.64	756.22	721.73	512.6
#22	613.00	651.31	614.71	677.59	512.6
#23	745.84	657.06	850.67	923.81	512.6
#24	N/A	N/A	523.01	408.83	390.2
#25	490.07	498.11	533.06	486.24	390.2
#26	469.32	412.51	509.78	367.10	390.2
#27	272.03	325.02	307.53	411.81	327.4
#28	300.33	298.53	259.74	239.44	327.4

Table 33: Summary of calibrated white noise per radiometer at 3 K sky input compared with requirements. Values obtained using uncalibrated white noise measured during RAA tests.

From uncalibrated white noise

	R0	R1	Requirement
#18	460†	460	362
#19	536	512	362
#20	565	584	362
#21	415	522	362
#22	447	456	362
#23	494	626	362
#24	324†	325	276
#25	349	360	276
#26	310	302	276
#27	209	249	232
#28	212	176	232

†Value copied from radiometer R1

From radiometer equation

	R0	R1	Requirement
#18	460‡	460	362
#19	480	450	362
#20	500	490	362
#21	480	400	362
#22	420	390	362
#23	410	440	362
#24	260‡	260	276
#25	310	330	276
#26	360	320	276
#27	250	260	232
#28	190	190	232

†Value copied from radiometer R1

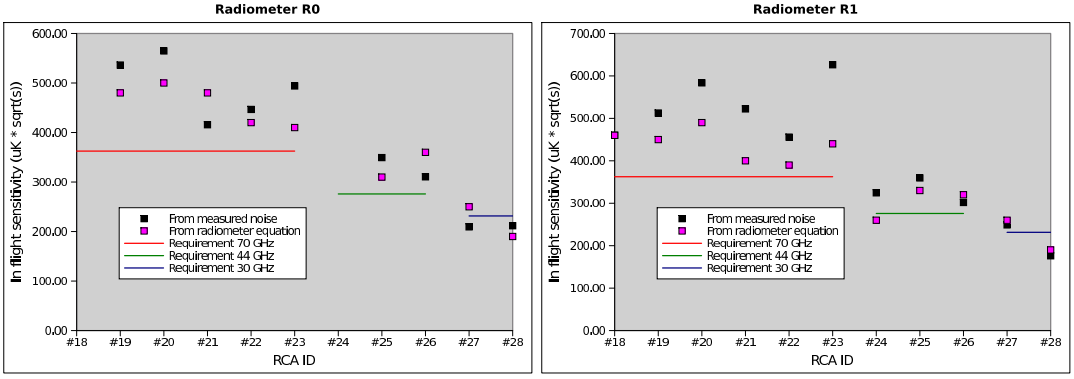

Figure 40: Radiometer in-flight sensitivities calculated with the two methods outlined above. 30 and 44 GHz estimates are in good agreement, while the 70 GHz values are more scattered.

Table 34: Summary of calibrated white noise per frequency channel at 3 K sky input compared with requirements.

From uncalibrated white noise				From radiometer equation			
	Meas. (μK$\times\sqrt{\text{s}}$)	**Req.** (μK$\times\sqrt{\text{s}}$)	Δ (%)		**Meas.** (μK$\times\sqrt{\text{s}}$)	**Req.** (μK$\times\sqrt{\text{s}}$)	Δ (%)
30 GHz	104.22	115.75	10.0%	30 GHz	108.86	115.75	6.0%
44 GHz	133.56	112.64	-18.6%	44 GHz	123.39	112.64	-9.5%
70 GHz	139.05	104.63	-32.9%	70 GHz	128.61	104.63	-22.9%

7.4 RCA and RAA tests results comparison

NOTE: this section has been incorporated into the previous one (7.3). Please refer to [AD5] for the older version.

7.5 Frequency spikes in noise spectrum

NOTE: this section has been rewritten and issued as a separate technical note. Please refer to [AD5] for the older version.

Details about source, characterisation and impact of frequency spikes in the noise spectrum is reported in [RD6].

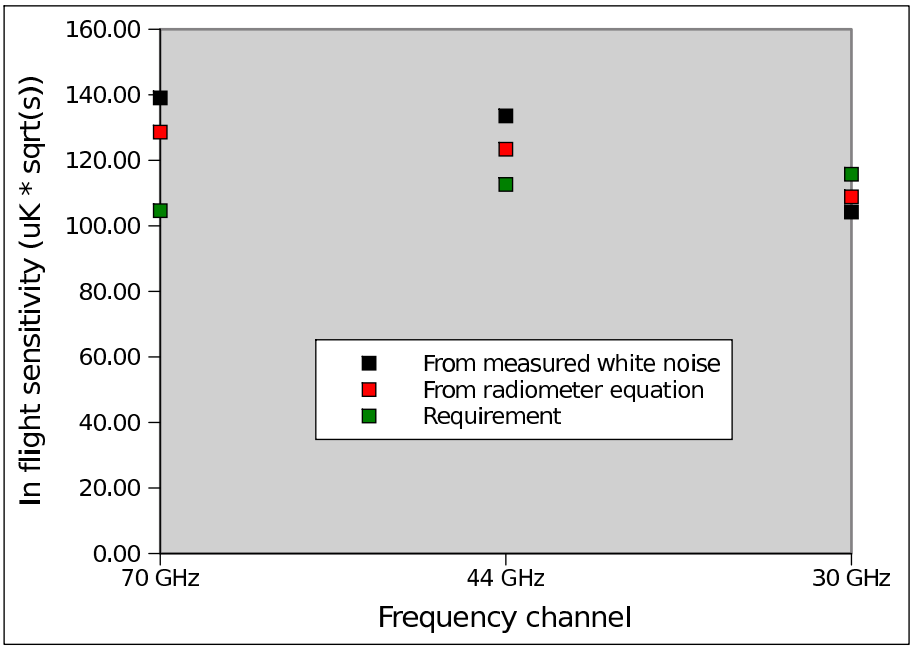

Figure 41: In flight calibrated sensitivities estimated with the two methods described at the beginning of this section compared with requirements.

8 Susceptibility tests

8.1 Susceptibility to front-end temperature fluctuations

8.1.1 Test experimental conditions

The susceptibility to front-end temperature variations has been analysed using three datasets: THF_0011 and THF_0012 which were dedicated tests to study the suceptibility to FEU temperature variations and XXX_0134, i.e. the data acquired during the warm-up test. the first part of the test (the range with the BEU temperature constant). In the following figures, we show of the temperature behaviour in the three datasets.

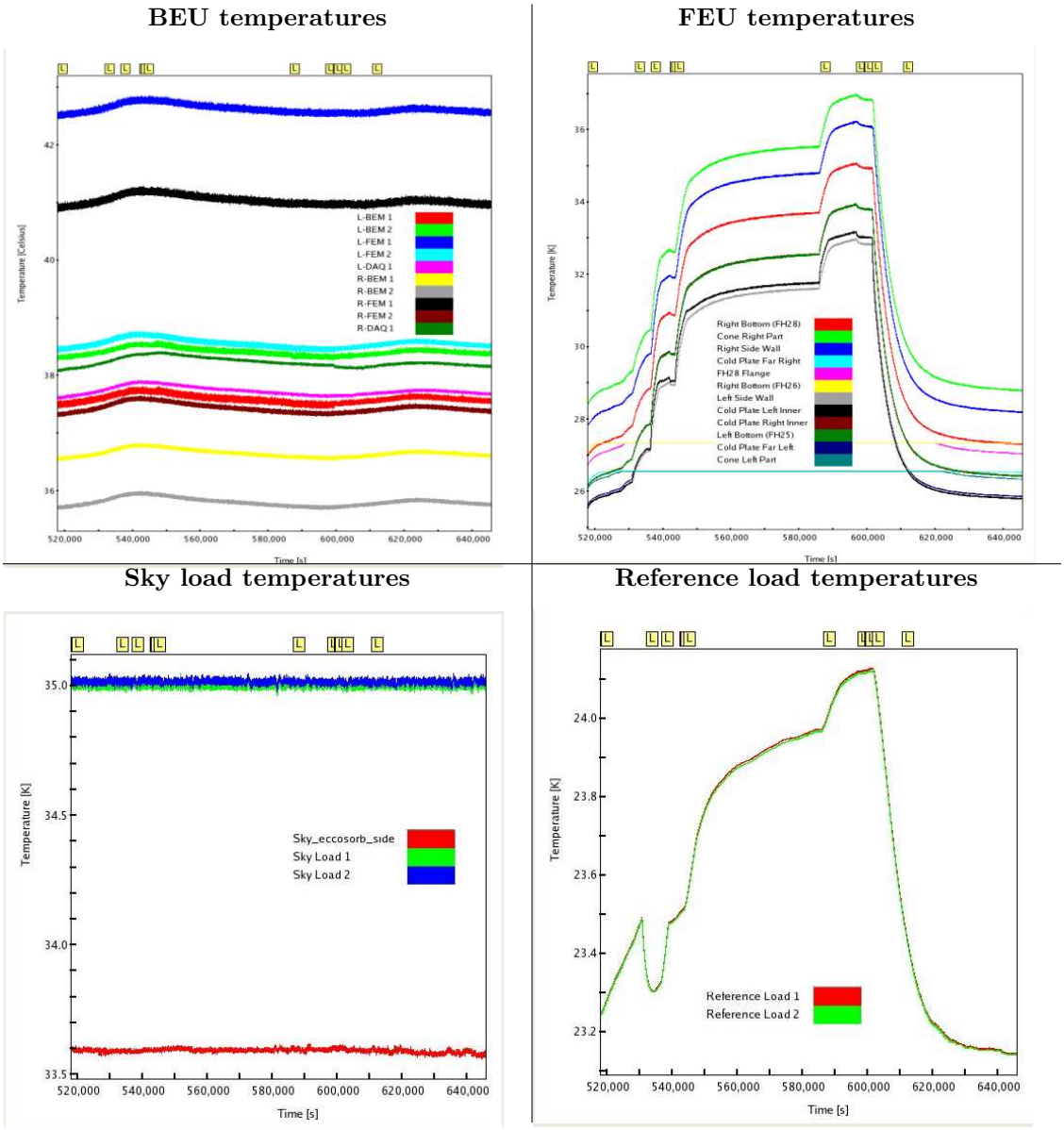

Figure 42: Temperature behaviour during THF_0011 test

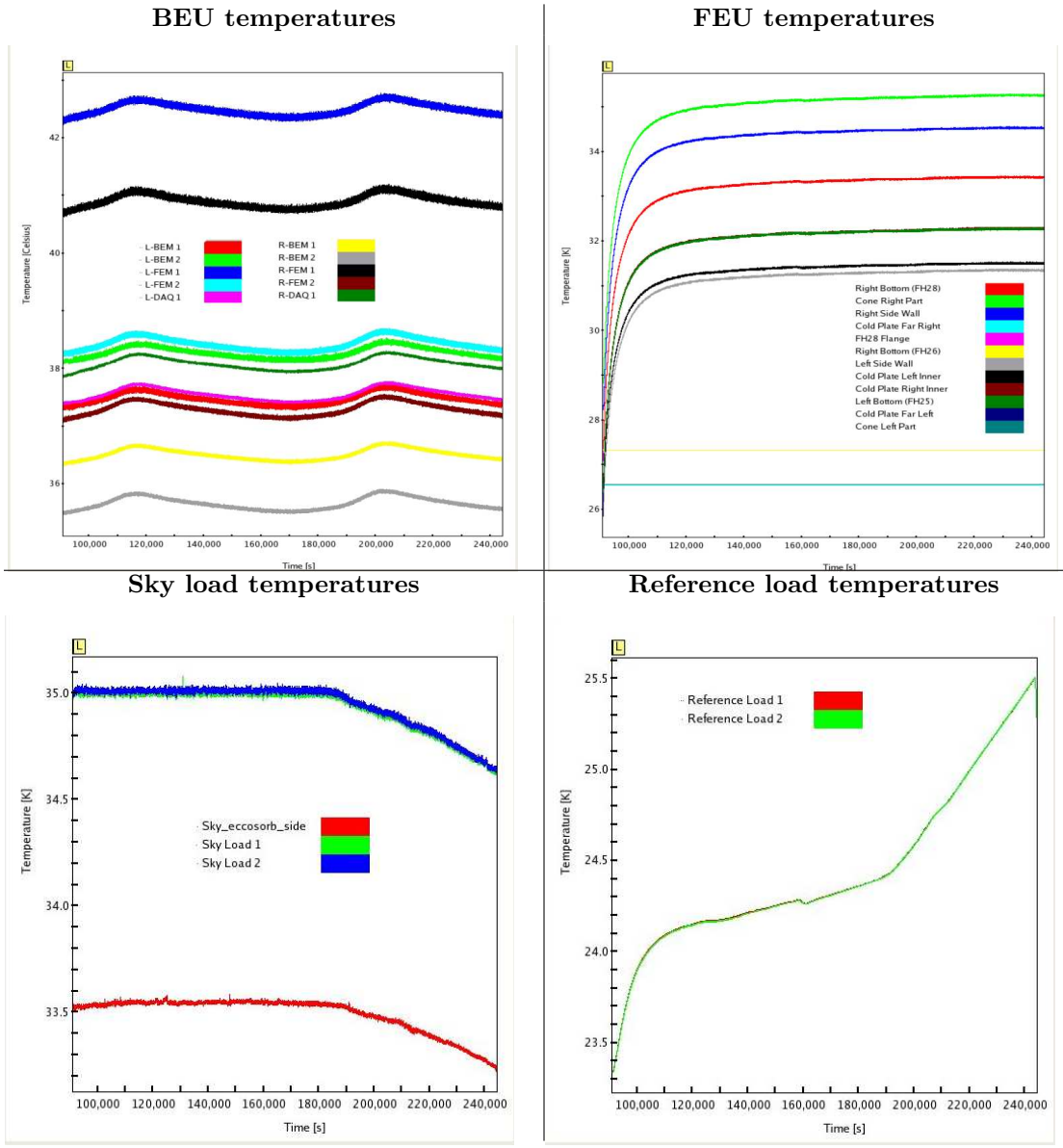

Figure 43: Temperature behaviour during THF_0012 test

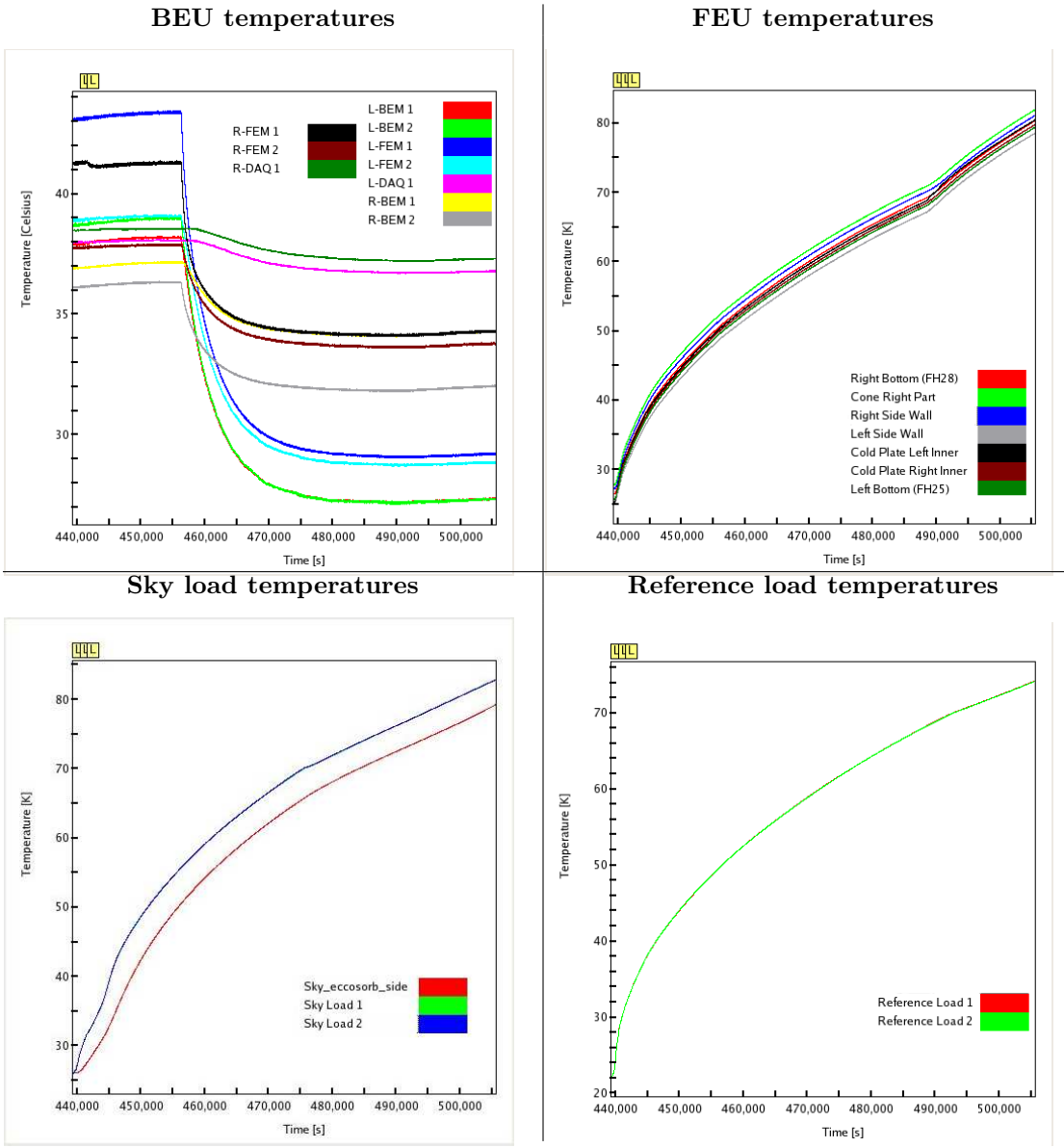

Figure 44: Temperature behaviour during XXX_0134 test

Further analysis conducted on this test has shown that the conditions were far from optimal for a sound characterisation of the thermal susceptibility (many temperatures were varying at the same time) so we have finally discarded this test from the analysis.

Furthermore after THF_0011 and THF_0012 were completed we discovered that many channels were not biased correctly because of a procedure error. Therefore we report results only for the channels with the correct bias conditions that are listed in Table 35.

Table 35: List of channels that were biased correctly during susceptibility tests

RCA ID	**ACA**	Outputs
#27	M1, M2	R0D0, R0D1
#21	S1, S2	R1D0, R1D1
#22	All channels	All outputs
#23	S1, S2	R1D0, R1D1
#19	S1, S2	R1D0, R1D1

8.1.2 Results

NOTE: this section has been mostly modified. Please refer to [AD5] for the older version.

Temperature susceptibility tests conducted on individual receivers have defined the main susceptibility parameters, $\partial T_{\rm noise}/\partial T_{\rm phys}$ and $\partial G/\partial T_{\rm phys}$ that allow to estimate the impact of a certain temperature instability on the receiver output (see [RD5, RD1]).

The aim of the tests conducted at RAA level was to verify these parameters by measuring a variation in the receiver output caused by a temperature variation in the front-end unit and compare it with the prediction of the receiver model.

In Fig. 45 we report measured and theoretical transfer functions for the channels which were biased correctly. Some mismatches between theory and measurements are still visible, especialli for LFI22 that shows a theoretical behaviour with opposite sign with respect to measurements and LFI27, LFI21 for which the sign is correct but the measured susceptibility is larger than predicted.

8.2 Susceptibility to back-end temperature fluctuations

8.2.1 Test experimental conditions

The susceptibility to back-end temperature variations has been analysed using the dataset ST1_0002. This test is characterised by a long acquisition at stable conditions with a temperature variation of the back-end unit. We use three time windows with BEM temperatures equal to 36.29, 36.41 and 36.66 ∘C. Detailed results can be found in Annex 24. In the following figures, we show the other temperature behaviours in the dataset. We could not obtain the RCA21 result because We could not read the dataset.

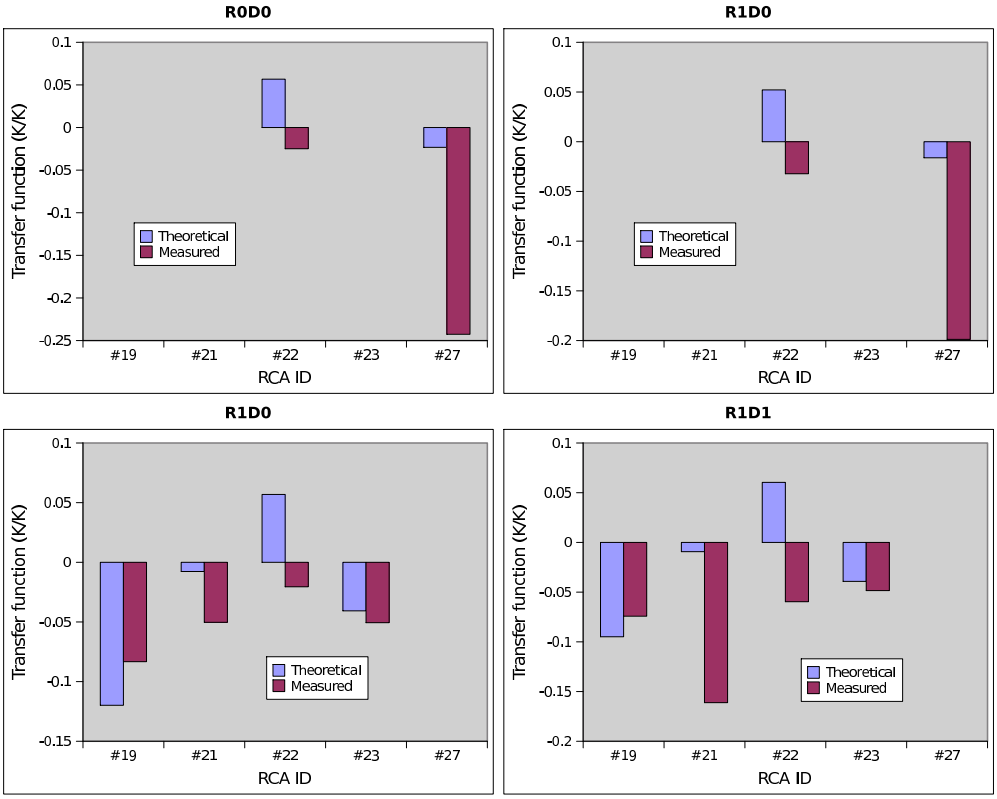

Figure 45: Measured and predicted radiometric thermal transfer functions.

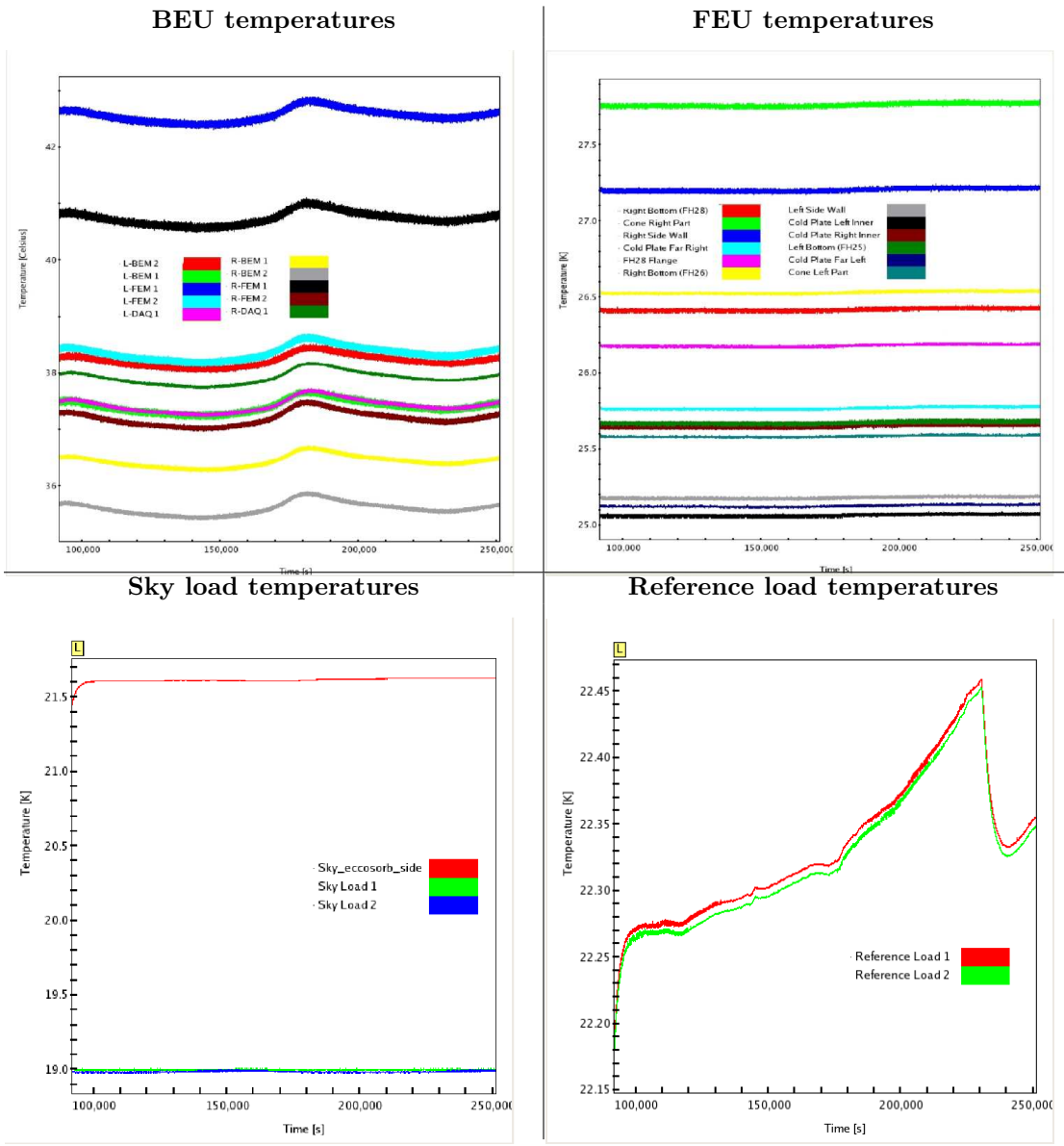

Figure 46: Temperature behaviour during ST1_0002 test

8.2.2 30 GHz

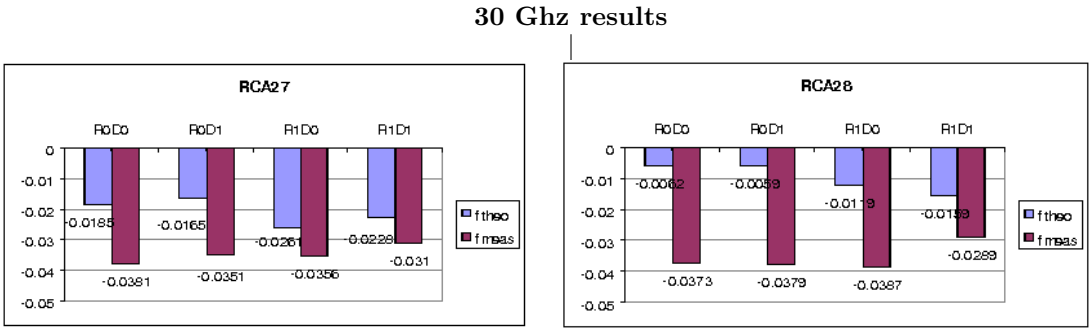

8.2.3 44 GHz

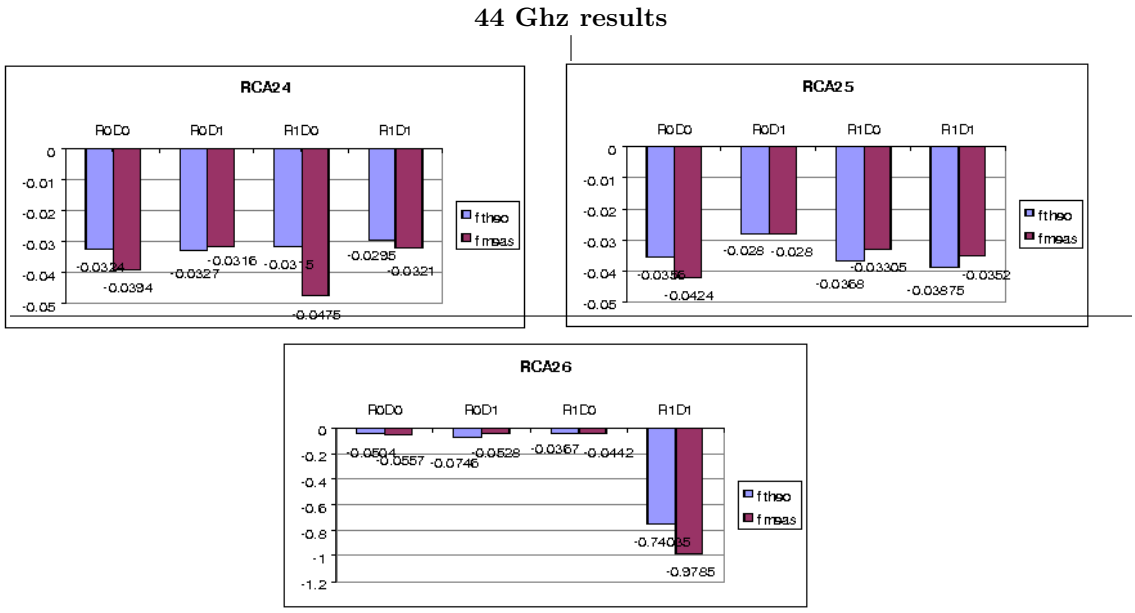

8.2.4 70 GHz

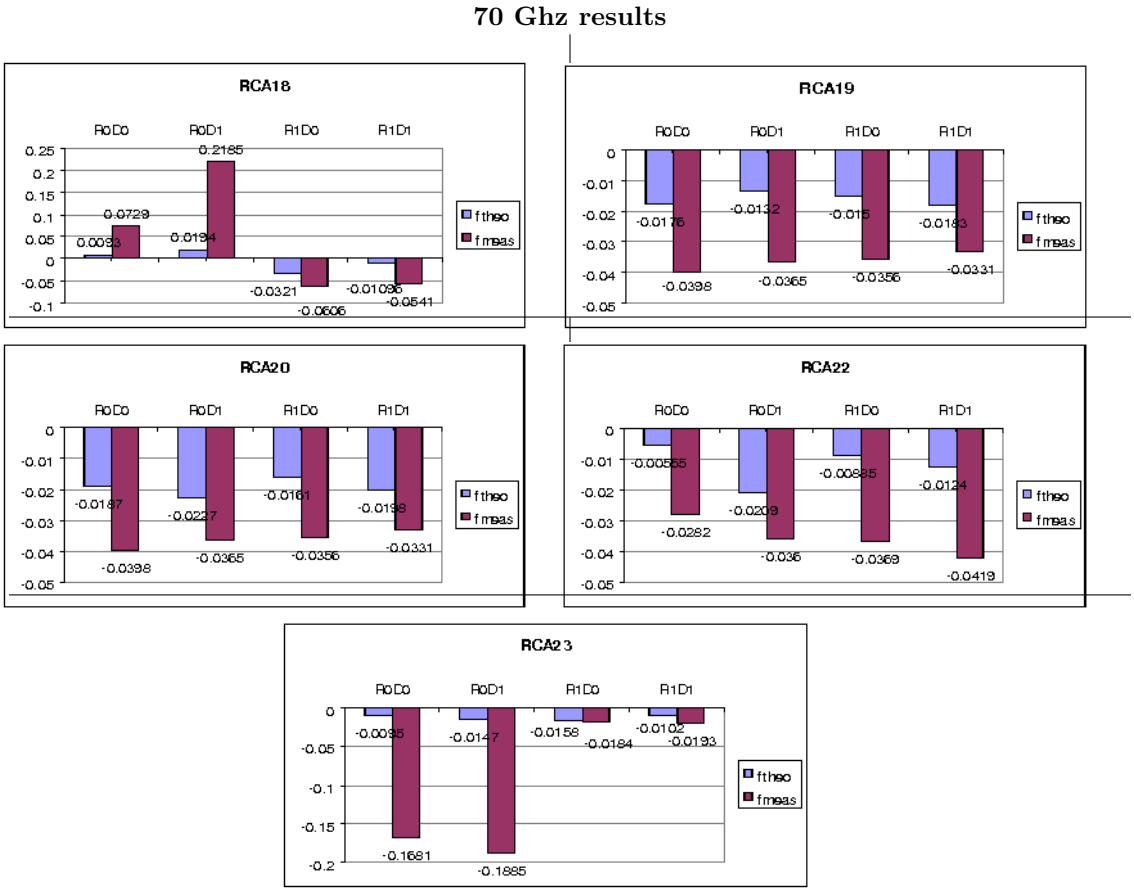

8.3 Susceptibility to bias voltage fluctuations

The ELE test is intended to measure the effect on all radiometers of the variation of the bias on one receiver while all the others are on.

8.4 Experimental

For any nominal value of Vgate 1 and Vgate 2, bias steps are set on ±2 LSB, ±4 LSB, ±8 LSB. Each step is acquired for 60 seconds in AVR1 mode. N_average is set to nominal value (126 samples) for the 70 and 44 GHz channels, while is set to 88 for the 30 GHz channels. Data are acquired for one power group at each time, due to limitations on the test acquisition process. A further 30 min acquisition, with all radiometers at nominal bias, has been taken at the end of the test, with N_average set as above indicated. This is used as a reference for data analysis.

The output files contains a sequence of Vgate1 bias steps on all radiometers (each RCA, each omt arm, each radiometer). The same is repeated for Vgate2 bias steps. Each sequence of steps is identified by a trigger signal.

8.5 Results

The analysis is focused on evaluating the effect of a single bias step perturbation on one of the gate voltages on all radiometers.
30GHz RCAs. The effect on the output is an increase of V_{out} when Vgate is increased. The effect on V_{out} is significant only on the radiometer arm where the bias perturbation is applied. The effect is roughly one order of magnitude larger when the perturbation is applied on Vgate2.

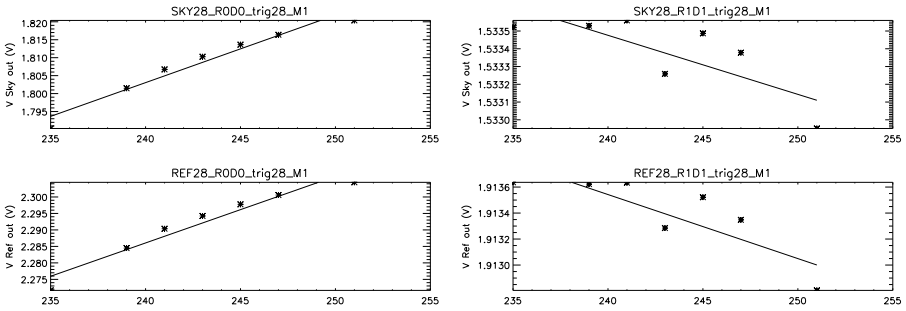

Figure 47: Steps on Vgate1, Feed Horn 28 M1. At left the output on M1 is plotted; note the significant increase in output. In the right panel the output for S1 is reported. No major effect is found: the points are scattered and the linear fit is not significant.

44GHz RCAs. As for the 30GHz channels, the effect on the output is an increase of V_{out} where Vgate is increased. The effect on V_{out} is significant only on the radiometer arm where the bias perturbation is applied.

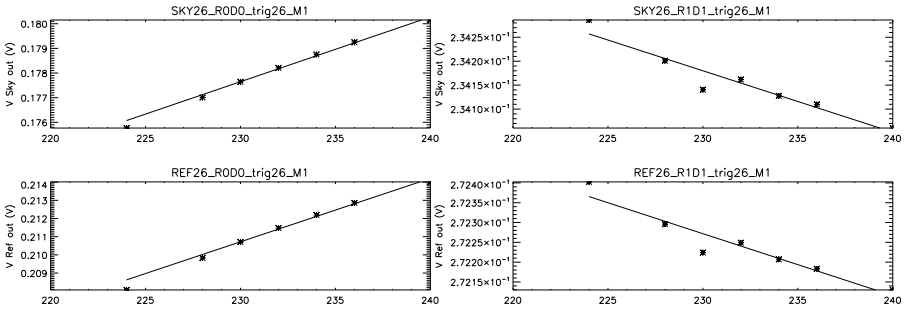

Figure 48: Steps on Vgate1, Feed Horn 26 M1. At left the output on M1 is plotted; note the significant increase in output. In the right panel the output for S1 is reported. No major effect is found: the points are scattered and the linear fit is not significant.

70GHz RCAs. Here the effect on V_{out} is not monotonic with Vgate. It is possible to observe, as for example for the RCA 20, a maximum on the output around the optimal bias value or a decrease in V_{out} when Vgate is increased, as for RCA18. Also in this case the effect is significant only on the same omt arm where the perturbation is applied.

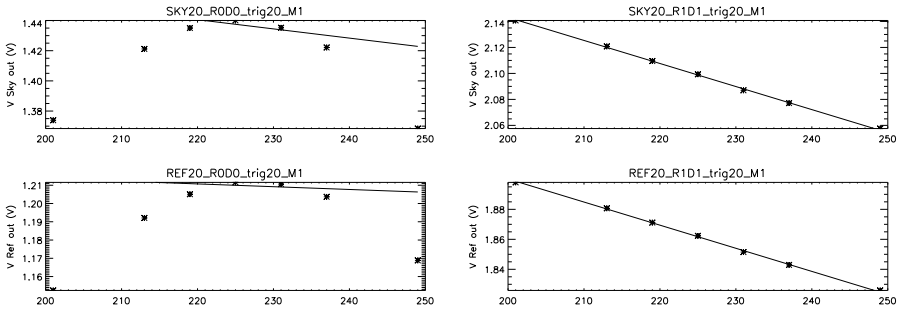

Figure 49: Steps on Vgate1, Feed Horn 20 M1. At left the output on M1 is plotted; note the significant increase in output. In the right panel the output for S1 is reported. Here Vout is decreasing.

Is it also possible to evaluate the effect of bias steps on RCA connected to the same power group. An example is reported in Figure 50. Here the Vgate bias steps are applied on Gate 1, RCA 18, M1. The output is reported for RCA18-M1 and RCA26-M1, belonging to the same power group. Solid line refer to RCA18 output, while dashed line is the RCA26 output. As expected, the effect on RCA26 is significantely lower.

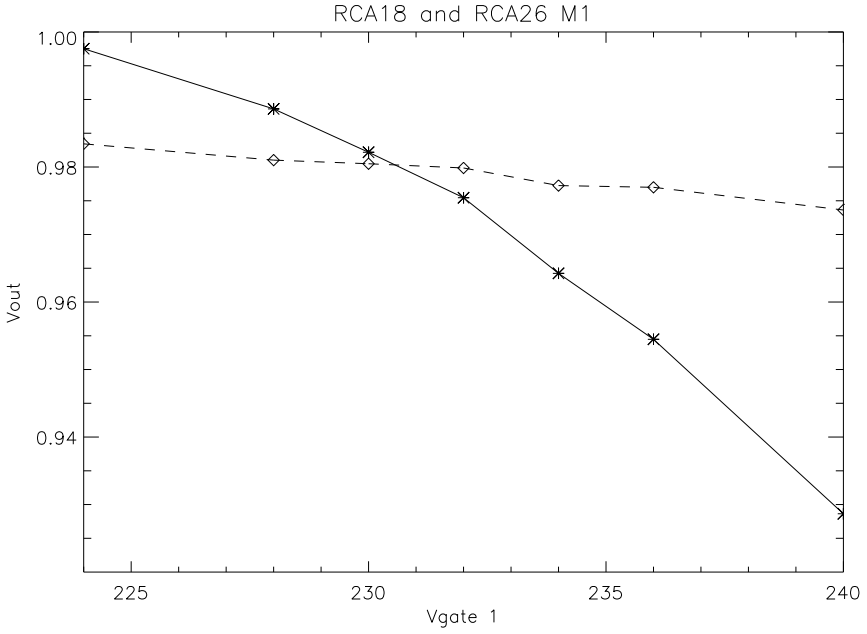

Figure 50: The effect of bias step on RCA of the same power group. Steps on Vgate1, RCA18, M1. Solid line: Vout(RCA18-M1). Dashed line: Vout(RCA26-M1)

Additional data are reported in the annex. Further analysis is in progress to evaluate the effect on white noise level, different effect on Sky and Ref output and on the correlation between output of the same power group.

9 REBA quantisation and compression tests

9.1 Introduction

The REBA tuning tests aim to find the optimal set of values uses by the REBA to quantize and compress the scientific data coming from the 44 LFI detectors. Data quantization and compression is implemented in the nominal acquisition mode (`COM5`). Its purpose is to reduce the packet size in order to match the requirements on the data rate sent by Planck to the Earth. The best strategy is to have a good compression ratio of the signal (≈ 2.4) while keeping the quantization error well below the intrinsic RMS of the radiometric output ($\sim 10\%$). For this purpose, a number of tuning tests have been made on the REBA in order to find an optimal set of quantization/compression parameters for each detector.

9.2 REBA operations

The REBA accepts a stream of data coming from the DAE, transforms them via a lossy transformation (i.e. it throws away some information) and then compresses them. The purpose of the transformation is to achieve a greater compression efficiency. In this section we provide some details about these operations.

When digitized data flow from the DAE into the REBA, the following sequence of operations happens while in nominal mode (`COM5`):

1. A number of N consecutive sky samples are summed together, and the same for the reference. This is equivalent to take the average of the data. N is chosen in order to have about three averaged samples per beam size.

2. For each pair of averaged samples $(\bar{x}_\mathrm{s}, \bar{x}_\mathrm{r})$ the following transformation $(\bar{x}_\mathrm{s}, \bar{x}_\mathrm{r}) \rightarrow (q_1, q_2)$ is made:

$$q_1 = \Big[\big(\bar{x}_\mathrm{s} - r_1 \bar{x}_\mathrm{r} + \Delta\big) \times s\Big], \tag{13}$$

$$q_1 = \Big[\big(\bar{x}_\mathrm{s} - r_2 \bar{x}_\mathrm{r} + \Delta\big) \times s\Big], \tag{14}$$

   where the square brackets denote a rounding operation (this is the origin of the quantization, whose effect is greater for low values of s).

   The quantities Δ (the *offset*), s (the *second quantization*), r_1 and r_2 (the *gain modulation factors*) are free parameters. Finding their optimal value is the objective of the REBA tuning.

3. The pair (q_1, q_2) is compressed using an arithmetic coding algorithm, put into a packet and sent to the Earth.

When the packets are acquired by the TQL/TMH, they are uncompressed, and equations (13) and (14) are inverted in order to get x'_s and x'_r. Of course, $x_\mathrm{s} \neq x'_\mathrm{r}$ and $x_\mathrm{r} \neq x'_\mathrm{r}$: their difference is called the *quantization error*, and must be as small as possible.

The REBA is able to operate in other modes, called *diagnostic modes*. To tune the compressor we use mode `AVR1`, where only the first passage is done (e.g. the REBA skips the lossy transformation and the compression phases).

9.3 Details about the REBA tests

In principle, each time the sky/reference load change their temperature, a new tuning of the REBA should be made. This was not necessary during the tests, as we have acquired data in mode `AVR1` for the most part of the FM tests.

Tuning the REBA is a two-phases process:

Tuning phase: We acquired data for all the radiometers in mode `AVR1`, while the sky and reference loads were kept at stable conditions. Using mode `AVR1` ensures that the REBA induces no data loss.

The radiometer output is used by OCA, one of the modules of the LIFE software suite, to find the best values for Δ, s, r_1 and r_2 (see equations 13 and 14). The OCA algorithm uses a software-only implementation of the REBA compressor to compress the `AVR1` data trying to achieve the target compression rate (2.4) while minimizing the quantization error.

Verification phase: The optimal parameters for the 44 channels are fed to the REBA and a new acquisition with stable conditions is made. Data are collected both in mode `AVR1` and `COM5`. Using REVERIE, another LIFE tool, the quantization error is estimated from the difference between the two streams, and it is compared with the intrinsic RMS error in order to quantify the impact of the quantization on the scientific output.

Here is a list of the tests made to tune the REBA:

Test	Description
TUN_0060	`AVR1` acquisition for feed horns #18-#23.
TUN_0061	`AVR1` acquisition for feed horns #24-#28.
TUN_0062	`AVR1`/`COM5` verification for feed horns #18-#22.
TUN_0063	`AVR1`/`COM5` verification for feed horns #23-#28.

We acquired two tests for the tuning and two for the verification, as telemetry constraints while in the uncompressed mode `AVR1` prevented us from acquiring all the 44 channels at the same time.

9.4 Results

The following table provides the list of optimal parameters found by OCA. In order to optimize the time, the algorithm made the following assumptions:

$$r_1 = \langle x_\mathrm{s} \rangle \,/\, \langle x_\mathrm{r} \rangle \,, \tag{15}$$

$$\Delta = -\langle x_\mathrm{s} \rangle + \frac{r_1 + r_2}{2} \langle x_\mathrm{r} \rangle \,. \tag{16}$$

Using these two equations, the code explores a two-parameters space, therefore simplifying the optimization process.

In the table below also report the parameters σ/q (noise over quantisation step) and C_r (co-pression ratio) that summarise the scientific and telemetry performances that need to be compliant with the following requirements: $\sigma/q \geqslant 2$ and $C_r \geqslant 2.4$. Values from the table below indicate that both requirements have been met (σ/q is always greater than 2 and the average C_r is ~ 2.4.

Table 36: List of optimal REBA parameters

Feed	Chan ID	r_1	r_2	Δ	s	$N_{\rm av}$	σ/q	C_r
18	R0D0	1.00	-0.22	-5359.41	1.46	52	3.72	2.40
	R0D1	1.02	-0.21	-5568.31	1.07	52	3.41	2.45
	R1D0	0.95	-0.26	-7327.35	1.34	52	2.07	2.40
	R1D1	0.98	-0.24	-7125.57	1.82	52	2.22	2.34
19	R0D0	0.94	-0.26	-6261.11	1.27	52	2.57	2.41
	R0D1	0.91	-0.28	-5998.7	0.72	52	2.50	2.41
	R1D0	0.96	-0.25	-6368.42	1.48	52	2.77	2.46
	R1D1	0.94	-0.26	-6514.42	1.09	52	2.58	2.40
20	R0D0	0.94	-0.26	-6882.89	1.19	52	2.58	2.44
	R0D1	0.95	-0.26	-6657.11	1.71	52	3.10	2.41
	R1D0	0.91	-0.28	-5656.35	0.71	52	2.39	2.38
	R1D1	0.93	-0.27	-5680.95	1.12	52	2.52	2.44
21	R0D0	0.96	-0.25	-6635.29	1.18	52	2.76	2.42
	R0D1	0.96	-0.25	-6489.73	1.2	52	2.41	2.37
	R1D0	0.93	-0.27	-5764.98	1.5	52	2.45	2.42
	R1D1	0.94	-0.26	-6205.53	1.52	52	2.12	2.41
22	R0D0	0.97	-0.24	-6451.81	1.33	52	2.44	2.39
	R0D1	0.97	-0.24	-6206.1	1.14	52	2.63	2.37
	R1D0	0.94	-0.26	-6676.86	1.19	52	2.54	2.40
	R1D1	0.97	-0.24	-6610.82	1.28	52	2.85	2.41
23	R0D0	0.98	-0.24	-6433.48	2.07	52	3.00	2.45
	R0D1	0.95	-0.26	-5857.59	1.15	52	2.01	2.35
	R1D0	0.97	-0.24	-8137.46	1.52	52	2.17	2.40
	R1D1	0.98	-0.24	-7695.93	1.63	52	3.36	2.41
24	R0D0	0.96	-0.25	-7455.57	0.8	88	2.75	2.39
	R0D1	0.95	-0.26	-6328.58	0.8	88	2.01	2.38
	R1D0	0.95	-0.26	-6622.91	2.69	88	2.23	2.52
	R1D1	0.96	-0.25	-7000.99	2.11	88	2.82	2.56
25	R0D0	0.94	-0.26	-6920.67	1.96	88	2.82	2.45
	R0D1	0.95	-0.25	-6393	1.73	88	3.07	2.57
	R1D0	0.93	-0.26	-6267.06	1.92	88	2.70	2.53
	R1D1	0.94	-0.26	-6535.74	2.04	88	2.53	2.51
26	R0D0	0.97	-0.28	-6804.56	5.33	88	2.12	2.37
	R0D1	0.97	-0.25	-7096.86	3.74	88	3.27	2.50
	R1D0	0.94	-0.27	-6010.62	3.81	88	2.36	2.34
	R1D1	0.96	-0.25	-7862.1	3.35	88	2.47	2.46
27	R0D0	0.85	-0.32	-6515.75	1.34	126	3.09	2.42
	R0D1	0.91	-0.28	-6522.67	2.52	126	3.43	2.44
	R1D0	0.87	-0.31	-6355.57	1.45	126	3.03	2.43
	R1D1	0.87	-0.31	-6380.6	1.53	126	3.18	2.44
28	R0D0	0.92	-0.28	-6506.1	2.35	126	3.03	2.39
	R0D1	0.89	-0.3	-6089.71	1.56	126	2.97	2.42
	R1D0	0.93	-0.27	-5954.07	2.25	126	3.58	2.45
	R1D1	0.94	-0.26	-5797.02	1.81	126	3.53	2.48

9.5 Discussion

Results in Table 36 indicate that it was possible to obtain optimal REBA parameters which satisfy both the scientific requirement of $\sigma/q \geq 2$ and the telemetry requirements of $c_r \geq 2.4$.

The only exception was detector R1D1 of LFI26 which showed an anomalous behaviour which has been subsequently understood. To understand this anomaly we must spend few words about some of the details of OCA, the REBA analysis software.

The compression algorithm is designed to find a configuration where the compression ratio (C_r) is 2.4 in every channel. If OCA is able to achieve a greater compression ratio (for low-noise channels), it will reduce the quantization error in the signal (thus incrementing the entropy of the data) until C_r becomes equal to 2.4.

The low RMS in channel #2611 caused the compressor to achieve a C_r far greater than 2.4. By reducing the quantization, the number of distinct symbols in the data stream increased till the samples were larger than the 14 bits used by the REBA to store them. This caused an overflow and a subsequent offset in the compressed data.

Now that the problem has been discovered, the solution is fairly simple: OCA will be modified in order to take into account the 14-bit boundary when exploring the parameter space of the quantization parameters. This will not have an impact on the performances, as the problem only arises when a channel can be compressed far better than 2.4.

10 Dynamic thermal response of the focal plane unit to temperature fluctuations

10.1 Overview

There are two thermal models for the Planck/LFI instrument:

1. A complete model of the instrument
2. A more detailed model of the focal plane

The THF tests aim to validate the model of the focal plane by inducing a sinusoidal oscillation in the temperature of the cold end and measuring how the fluctuation propagates through the focal plane. The results are then compared with the estimates provided by the thermal model.

10.2 Validation of the thermal model

The thermal model of an object like LFI is a set of N nodes connected by M thermal conductors. Each node i must satisfy the following equation:

$$C_i \frac{\mathrm{d}T_i}{\mathrm{d}t} = \dot{Q}_i + \sum_k L_{ki}(T_k - T_i) + \sum_k R_{ki}(T_k^4 - T_i^4), \tag{17}$$

where T_i is the temperature of the node, C_i is the heat capacity, Q_i the amount of heat produced by the node, L_{ki} is the linear conductance between node i and k and R_{ki} the radiative conductance.

Calibrating a thermal model means to verify the value of the constants C_i, Q_i, L_{ki} and R_{ki} by measuring temperatures on the object itself and then comparing them with the predictions of the model. One usually wants to perform this calibration in two steps:

1. A first calibration keeps the temperatures fixed. Thus $\mathrm{d}T_i/\mathrm{d}t$ is zero and the value of C_i is not considered.
2. A dynamical calibration induces a fluctuation on some points of the object and compares the fluctuation on other points of the model. This calibration validates the values of C_i.

10.3 How the validation tests were made

The THF tests done during the LFI FM test campaign were done using a pure sinusoidal wave. The inductor was a power generator connected to the cold end of the focal plane. The amplitude and the frequency of the fluctuation were kept fixed during the test.

Five tests were made. However, only three are usable for our analysis, since in the other two ones the amplitude induced by the power generator was not enough to induce a measurable temperature fluctuation in the focal plane.

The details of the three tests, with the fluctuation period used, are provided here:

Test	Period [min]
THF_0004	30
THF_0008	12
THF_0009	90

10.4 Algorithms used during the analysis

When analyzing the dynamical performances of a thermal model, one usually wants to get a transfer function, i.e. a pair of functions γ_{ij}, ψ_{ij} which relate the temperature T_i and T_j at two points through the following function:

$$T_j = \gamma_{ij}(\nu)\, T_i^0 \sin\big(2\pi\nu t + \psi_{ij}(\nu)\big),$$

where T_i^0 is the mean temperature at point i.

In order to analyze the data, we developed three different methods. Each of them is able to determine the value of $\gamma(\nu)$ from the data acquired during some test.

1. The transfer function can be considered the ratio of the absolute value of the Fourier transform of the temperatures at i and j. This method can not be used to analyze `THF_0008` due to gaps in the data.

2. The amplitude of the fluctuations at i and j can be estimated simply by finding the maximum and minimum temperature measured during the tests.

3. The values for γ_{ij} and ψ_{ij} can be determined by computing a least square fit of the temperatures with a sinusoid.

10.5 Analysis results

In this section we show the results of our analysis. The transfer function was estimated for the following pair of temperature sensors:

1. Focal plane cold end → "Left Bottom (FH25)" (LM204332)

2. Focal plane cold end → "Right Bottom (FH26)" (LM306332)

3. Focal plane cold end → "Right Bottom (FH28)" (LM301332)

The results are here:

FH	Frequency [mHz]	γ [pure number]
25	0.209	0.495
	0.595	0.293
26	0.209	0.504
	0.595	0.246
28	0.209	0.557
	0.595	0.299

Table 37: Estimations of the FFT method (1.)

Table 38: Estimations of the direct method (2.)

FH	Frequency [mHz]	γ [pure number]
	0.2032 ± 0.0008	0.483 ± 0.005
25	0.600 ± 0.005	0.299 ± 0.004
	1.400 ± 0.008	0.194 ± 0.003
	0.2031 ± 0.0008	0.493 ± 0.003
26	0.600 ± 0.005	0.248 ± 0.003
	1.400 ± 0.009	0.118 ± 0.002
	0.2032 ± 0.0008	0.545 ± 0.005
28	0.600 ± 0.005	0.301 ± 0.004
	1.400 ± 0.009	0.169 ± 0.003

Table 39: Estimations of the fitting method (3.)

FH	Frequency [mHz]	γ [pure number]
	0.1999 ± 0.0016	0.4792 ± 0.0021
25	0.6010 ± 0.0025	0.295 ± 0.009
	1.403 ± 0.012	0.191 ± 0.014
	0.1999 ± 0.0016	0.4824 ± 0.0002
26	0.6003 ± 0.0032	0.2488 ± 0.0009
	1.403 ± 0.020	0.122 ± 0.002
	0.1999 ± 0.0016	0.5361 ± 0.0020
28	0.6005 ± 0.0025	0.302 ± 0.009
	1.403 ± 0.015	0.165 ± 0.017

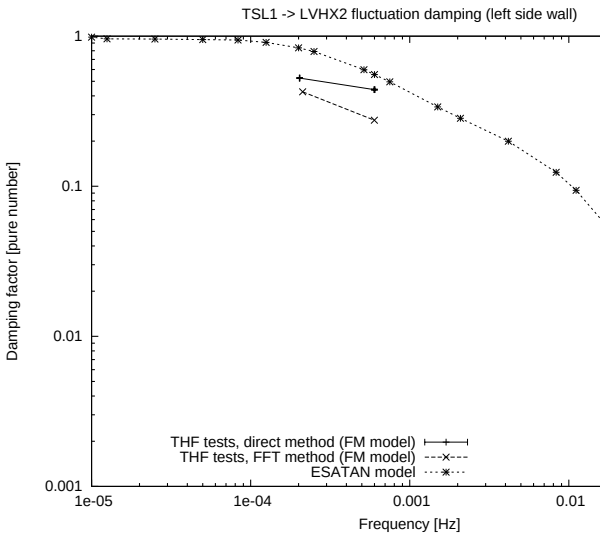

Figure 51: Comparison between the THF tests and the ESATAN thermal model for sensor TSL1 (left side wall).

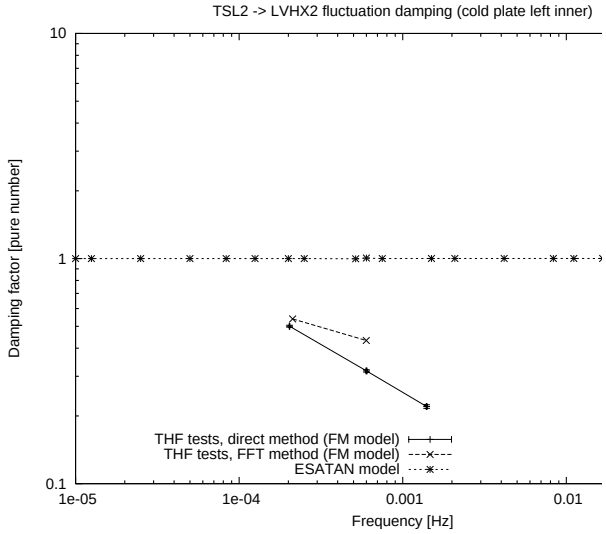

Figure 52: Comparison between the THF tests and the ESATAN thermal model for sensor TSL2 (cold plate left inner).

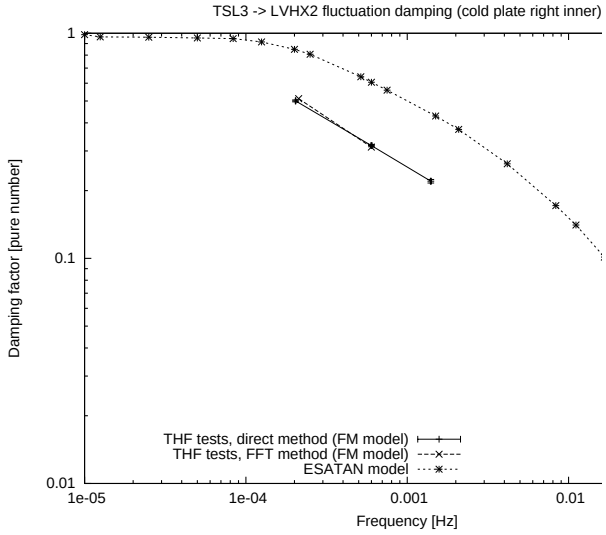

Figure 53: Comparison between the THF tests and the ESATAN thermal model for sensor TSL3 (cold plate right inner).

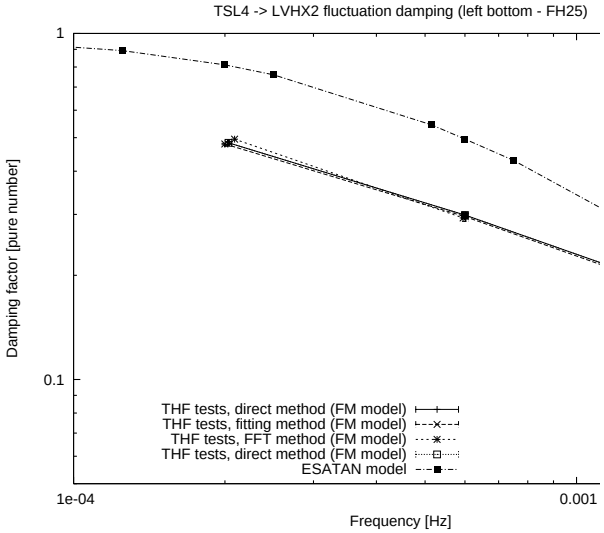

Figure 54: Comparison between the THF tests and the ESATAN thermal model for sensor TSL4 (left bottom - FH25).

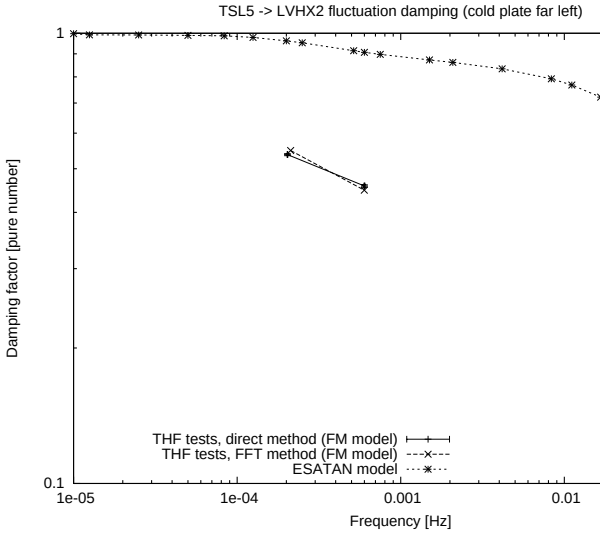

Figure 55: Comparison between the THF tests and the ESATAN thermal model for sensor TSL5 (cold plate far left).

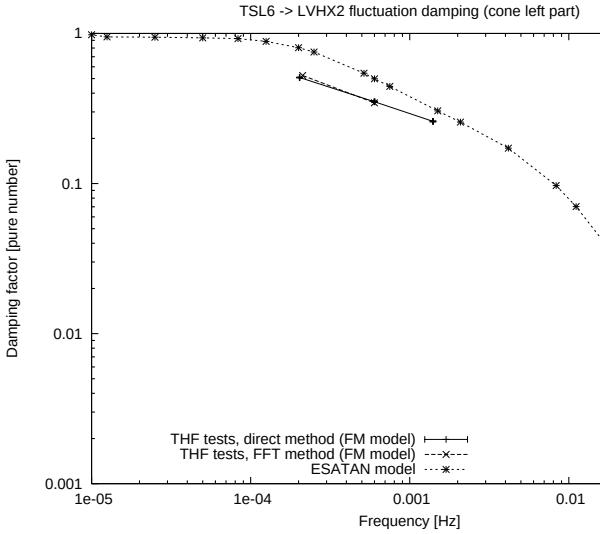

Figure 56: Comparison between the THF tests and the ESATAN thermal model for sensor TSL6 (cone left part).

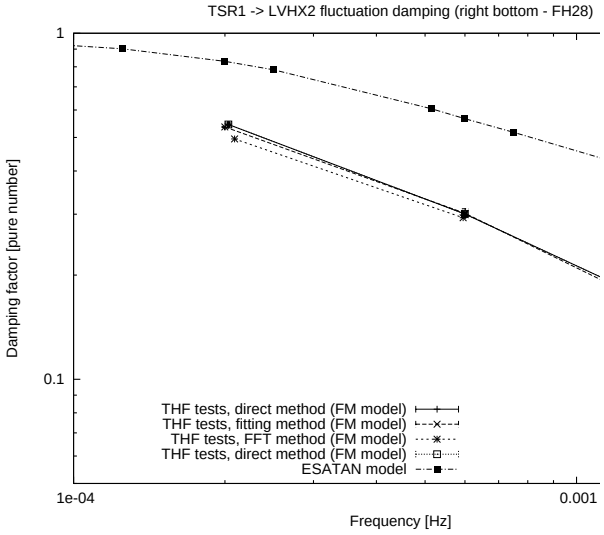

Figure 57: Comparison between the THF tests and the ESATAN thermal model for sensor TSR1 (right bottom - FH28).

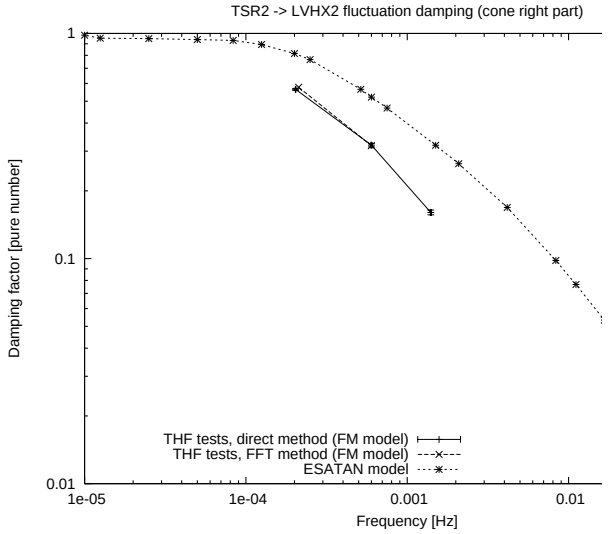

Figure 58: Comparison between the THF tests and the ESATAN thermal model for sensor TSR2 (cone right part).

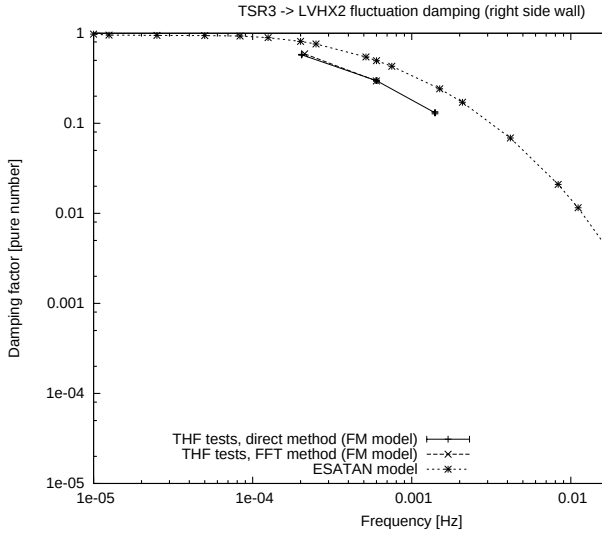

Figure 59: Comparison between the THF tests and the ESATAN thermal model for sensor TSR3 (right side wall).

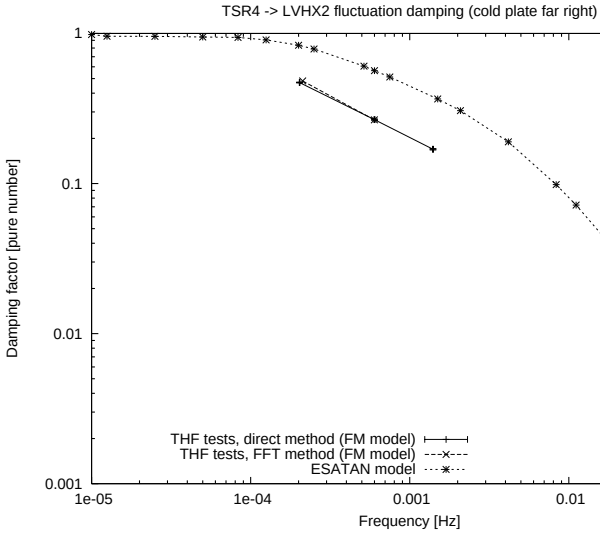

Figure 60: Comparison between the THF tests and the ESATAN thermal model for sensor TSR4 (cold plate far right).

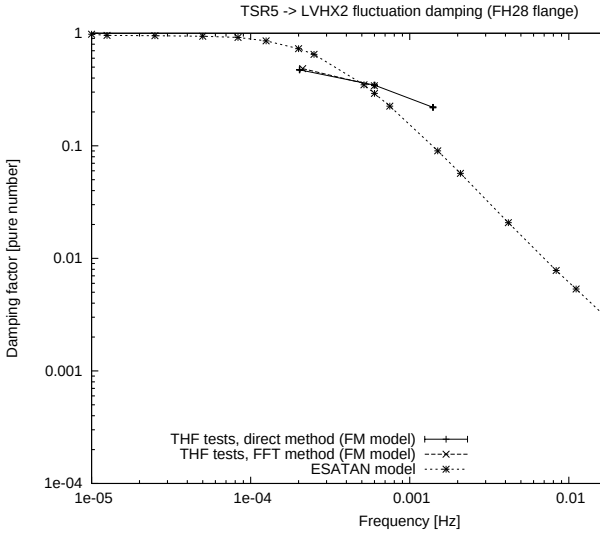

Figure 61: Comparison between the THF tests and the ESATAN thermal model for sensor TSR5 (FH28 flange).

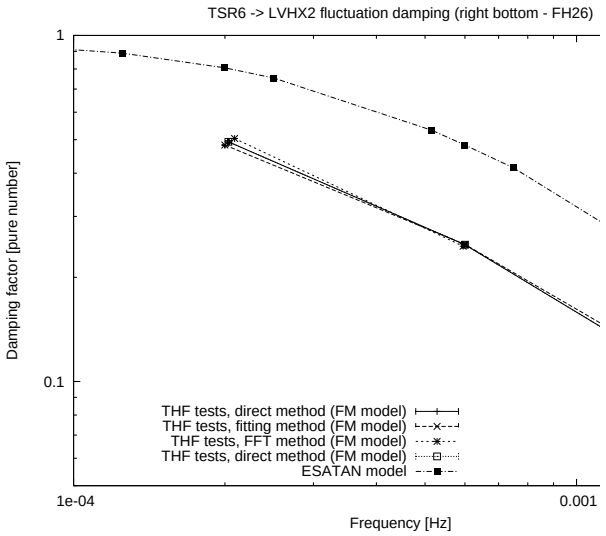

Figure 62: Comparison between the THF tests and the ESATAN thermal model for sensor TSR6 (right bottom - FH26).

10.6 Discussion

In general, the agreement between measurements and modelling is good, although the experimental data show a higher damping compared to the numerical model. Most likely reasons are:

1. A wrong choice in the thermal node considered in the comparison. This is certainly true at least for sensor TSL2, which shows that the node in the model was too near to the boundary condition to show any damping. It might be true for TSL5 as well (see below).

2. Contact resistances in the instrument that were not considered in the ESATAN model. Contact resistance can, in fact, improve the thermal damping by worsening the ability of heat to flow through discontinuities (i.e. the point where an horn connects to the FEM).

In two cases we could not produce reliable results for periods corresponding to 12 seconds. These cases were relative to sensors TSL1 and TSL5 which showed an high quantization of the signal.

The only case in which experimental data show lower damping than the model (at least for frequencies greater than 0.6 mHz) is TSR5: it is likely that this is connected to the choice of the temperature sensor. In fact the model considers each feed horn as made by 5 nodes. Node #2 has been compared with TSR5, while node #5 has been compared with TSR1. If we plot the thermal damping for nodes #3 and #4 we see (see Fig 63) that we obtain a damping curve that becomes more comparable (also in shape) with the experimental data.

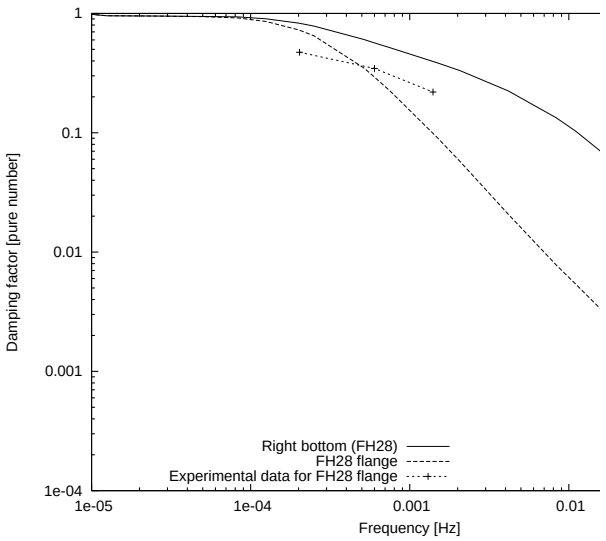

Figure 63: Comparison of experimental data acquired on sensor TSR5 with thermal model results assuming two different nodes on FEM # 28.

11 List of annex documents

1. Measurement of temperature distribution in an FM sky-load representative sample of ECCOSORB
2. Frequency spikes at cryogenic temperature for various DAE blanking times
3. Effect of blanking time on frequency spikes: BT = 7.5 μs
4. Effect of blanking time on frequency spikes: BT = 15 μs
5. Effect of blanking time on frequency spikes: BT = 21 μs
6. Effect of blanking time on frequency spikes: BT = 30 μs
7. Frequency spikes at cryogenic temperature for various DAE offset states
8. Effect of DAE offset on frequency spikes: analysis of LIS_0009 (part I)
9. Effect of DAE offset on frequency spikes: analysis of LIS_0009 (part II)
10. Effect of DAE offset on frequency spikes: analysis of LIS_0011
11. Effect of DAE offset on frequency spikes: analysis of LIS_0012
12. Frequency spikes at warm conditions
13. Frequency spikes at room temperature: test after cryogenic campaign
14. Frequency spikes at room temperature: test before cryogenic campaign
15. Frequency spikes using DAE with shorted inputs.
16. RCA RAA Phase Switch Tuning Comparison
17. Analysis of phase switch current tuning
18. Analysis of gate 1 voltage tuning
19. Analysis of gate 2 voltage tuning (first run)
20. Analysis of gate 2 voltage tuning (second run)
21. RAA radiometric basic properties
22. RAA noise properties
23. Susceptibility to FEU temperature variations
24. Susceptibility to BEU temperature variations
25. ELE report
26. Planck-LFI – fine tuning of REBA parameters: methods and software

A Appendix: Receiver basic properties – detailed figures

In this appendix we report detailed numerical results of receiver noise temperature, calibration constant and linearity, calculated as discussed in Sect. 6